Machine generated vertical vibration in elevators

Xabier Arrasate

Mechanical Engineering and Industrial Manufacturing Department

Mondragon Unibertsitatea

A thesis submitted for the degree of

PhilosophiæDoctor (PhD)

2013 June

Abstract

Vertical vibration deteriorates passenger comfort during an elevator travel. The drive system is a source of vertical vibration as well as the source of energy of the system. This report presents the results of a study of car vertical vibrations generated at the drive system in elevator installations.
The elevator system can be considered as a translating assembly of inertia elements coupled and constrained by one-dimensional slender continua. The inertia elements are the car assembly, the counterweight, the traction sheave and other rotating components of the system.
According to the roping arrangement and to the ratio of the tangential velocity of the traction sheave to the velocity of the car, the traction elevators can be classified as roped 1:1 or multiple reeving systems: the types examined in the present work are 1:1 and 2:1 traction elevators.
Distributed- and lumped-parameter models (DPM and LPM respectively) are developed to calculate the natural frequencies and mode shapes of stationary elevator systems and their results compared.
A non-stationary model of a 1:1 roping configuration elevator is developed as well to simulate the elevator acceleration response. The model accommodates the drive system dynamics: it includes the electric motor and the torque and velocity controllers, which ensure that the car follows a prescribed kinematic profile, so that good ride quality of the elevator is achieved. The machine parameters are computed by means of the Finite Element Method simulation software FLUX. With respect to the car-counterweight-sheave-ropes assembly, a LPM and a novel DPM are developed. The elevator dynamics represented by the DPM is described by a partial differential equation set that is discretised by expanding the vertical displacements in terms of the linear stationary mode shapes of a system

composed of three masses constrained by the suspension rope. The models are implemented in the MATLAB/Simulink computational environment and the system response is determined through numerical simulation. It is shown that the LPM forms a good approximation of the DPM.

Experimental tests are carried out on laboratory models. The elasticity modulus of the rope and the friction coefficients at the guide rail contact and at the machine are estimated. The acceleration response at the suspended masses and at the drive machine, the machine shaft velocity and the three phase current intensities supplied to the machine are measured during several travels. The machine torque is estimated from the current intensities.

The computed and measured accelerations are compared either in time or frequency domain and it is demonstrated that the elevator car vibrates at frequencies generated at the machine, especially when they are close to the system natural frequencies.

The proposed simulation models can be used as design and analysis tools in the development of high-performance elevator systems.

“ Nola sagar arbola,
hala gizona:
zenbat eta beteagoa,
orduan eta apalagoa ”

Gure aita zena gogoan

Acknowledgements

I would like to acknowledge MONDRAGON Corporation, Orona, the Basque Government and my workfellows from Ikerlan, but especially, Eskola, my colleagues from the Acoustics and Vibrations Group and Stefan Kaczmarczyck, for all their help.

Contents

List of Figures

LIST OF FIGURES

LIST OF FIGURES

List of Tables

LIST OF TABLES

Nomenclature

Abbreviations

cfg.	configuration
Eqn.	Equation
Eqns.	Equations
Exp.	Expression
Exps.	Expressions
Fig.	Figure
Figs.	Figures

Acronyms

AC	Alternating current
DC	Direct current
DOF	Degree of freedom
DPM	Distributed-parameter model
dqo	direct quadrature zero (transformation)
FEA	Finite element analysis
FEM	Finite element method
FRF	Frequency response function
LPM	Lumped-parameter model
ODE	Ordinary differential equation
OMA	Operational modal analysis
PDE	Partial differential equation
PI	Proportional integral
PMSM	Permanent magnet synchronous motor
PSD	Power spectral density
PWM	Pulse width modulated

Symbols

c	Viscous friction [kg/s]
g	Gravity [m/s^2]
i	Current intensity [A]
k	Stiffness [kg·s^{-2}]
l	Length [m]
m	Mass [kg]
n	Number of slots
r	Radius [m]
s	Undeformed rope section position [m]
v	Voltage [V]
p	Number of the machine stator pole pairs
t	Time [s]
u	Longitudinal displacement [m]
x	Rope section position at equilibrium [m]
A	Rope cross-sectional area [m^2]
B	Magnetic field [T]
E	Elasticity modulus [Pa]
I	Moment of inertia [kg·m^2]
L	Inductance [H]
P	Pressure [Pa]
R	Resistance [Ω]

Greek symbols

ζ	Damping coefficient
θ	Rotational angle [rad]
μ	Mass linear density [kg/m]
τ	Machine torque [N·m]
ω	Circular frequency [rad/s]
Φ	Mode shape
Ψ	Magnetic flux linkage [Wb]

Subscripts

$()_{\text{avg}}$	Average
$()_{\text{c}}$	Car
$()_{\text{cg}}$	Cogging

$()_{\mathrm{d}}$	d axis
$()_j$	jth order
$()_{\mathrm{m}}$	Mechanical shaft
$()_{\mathrm{n}}$	Normal
$()_{\mathrm{pm}}$	Magnet
$()_{\mathrm{q}}$	q axis
$()_{\mathrm{r}}$	Ripple
$()_{\mathrm{rd}}$	Radial
$()_{\mathrm{s}}$	Machine stator
$()_{\mathrm{sh}}$	Traction sheave
$()_{\mathrm{t}}$	Total
$()_{\mathrm{tg}}$	Tangential
$()_{\mathrm{w}}$	Counterweight

Superscripts

$()^{\mathrm{d}}$	Dynamic
$()^{\mathrm{e}}$	Equilibrium
$()^*$	Reference signal

Short Notation

$\dot{()}$	$\frac{\mathrm{d}}{\mathrm{d}t}$
$\ddot{()}$	$\frac{\mathrm{d}^2}{\mathrm{d}t^2}$
$()_t$	$\frac{\partial}{\partial t}$
$()_{tt}$	$\frac{\partial^2}{\partial t^2}$
$()'$	$\frac{\partial}{\partial s}$
$()''$	$\frac{\partial^2}{\partial s^2}$

1

Introduction

Elevators have become an integral part of any building facility over the past few decades. In our everyday life, we depend on them for vertical transportation in offices, schools, public buildings, airports, sub-stations...

Orona is a European company whose activity centres on the design, manufacturing, installation, maintenance and modernisation of mobility solutions, such as elevators, escalators and moving walkways. The business group is formed by 30 companies in Spain, France, Portugal, United Kingdom, Ireland, Belgium, The Netherlands and Luxembourg.

The work presented in this report is a fruit of the research strategy designed by Orona, whose shared objective is the research and development of intelligent and safe transport systems, more energy and socially efficient and better integrated into buildings. Orona Elevator Innovation Centre (EIC) is the advanced research centre where innovative solutions for the elevator industry are developed. It is geared towards technological research and the development of products for the Elevation sector and incorporates Ikerlan-IK4 and Mondragon Unibertsitatea as collaborative partners. These partners have been working since 2005 in a series of projects with the objective to increase the knowledge needed to design and manufacture comfortable elevators.

One of the challenges of elevator installations is to achieve and maintain good ride quality standards. This research work focuses on vertical vibration in an elevator; vertical vibration generated at the drive system and perceived by car passengers due to the elasticity of the suspension ropes.

1.1 History of elevators

Since the dawn of time, humans sought the way for more efficient vertical transportation of freight and passengers to different levels. These devices for transport goods up and down represent first elevators.

Elevator history begins several hundred years before Christ. The earliest elevators were called hoists. They were powered by human and animal power, or sometimes water-driven mechanisms. They were in use as early as the 3rd century BC.

Modern elevators were developed during the 1800s. These crude elevators slowly evolved from steam driven to hydraulic power. The first hydraulic elevators were designed using water pressure as the source of power. They were used for conveying materials in factories, warehouses and mines. Hydraulic elevators were often used in European factories.

In 1852, Elisha Graves Otis introduced the first safety contrivance for elevators. Otis established a company for manufacturing elevators.

Revolution in elevator technology began with the invention of hydraulic and electricity. Motor technology and control methods evolved rapidly and electricity quickly became the accepted source of power. The safety and speed of these elevators were significantly enhanced. The first electric elevator was built by the German inventor Wener Von Siemens in 1880. In 1887, an electric elevator with automatic doors that would close off the elevator shaft was patented. This invention made elevators safer. In 1889, the first commercially successful electric elevator was installed. Another milestone in the new business was the Eiffel Tower in 1889 which at 321 meters is still recognised as the symbol of Paris. Many changes in elevator design and installation were made by the great advances in electronic systems during World War II.

Today, modern commercial buildings commonly have multiple elevators with a unified control system. In addition, all modern elevators have special override controls (to make elevators go directly to a specific floor without intermediate stops).

1.2 Description of an elevator

A traction drive elevator is a complex system containing both mechanical and electrical components. The electrical part of the system involves an electric motor operating in a closed loop velocity control system. The mechanical part of the system is composed

of suspended masses (a car and a counterweight), a suspension system (hoist ropes or belts), a traction sheave and pulleys (see Fig. 1.1).

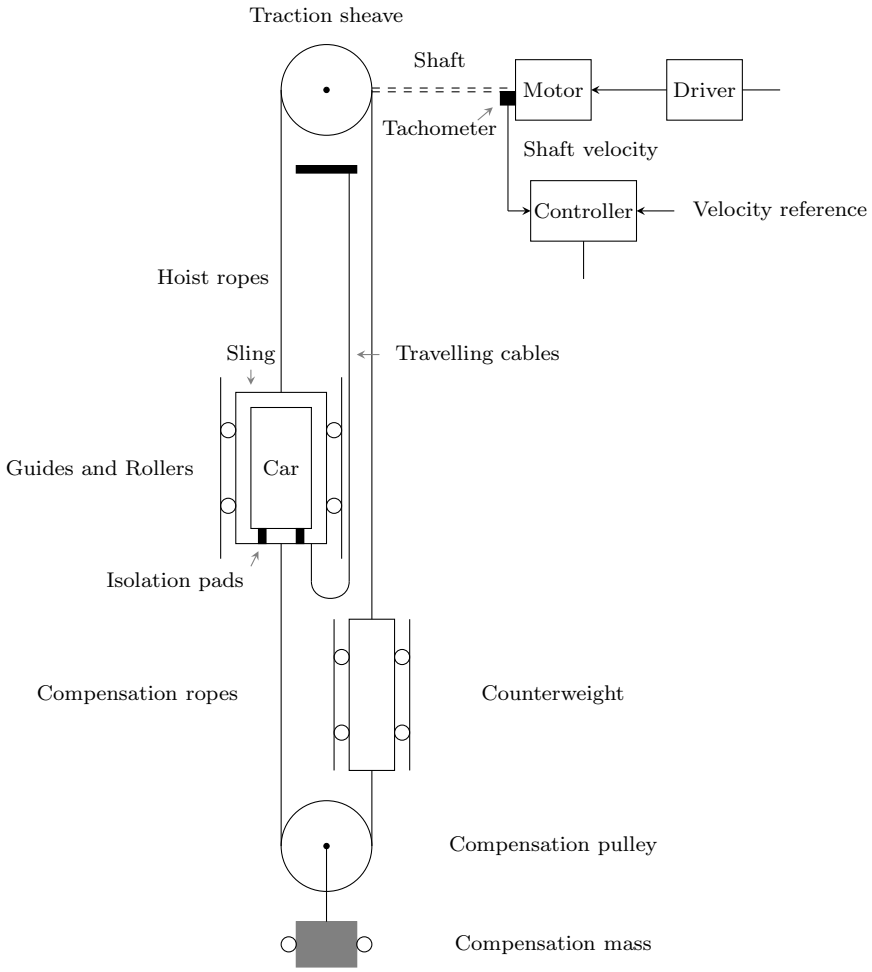

Figure 1.1: Elevator system

The motor drives the traction sheave which in turn is coupled with the hoist ropes attached to the sling and to the counterweight through a pulley system.
The elevator car is mounted in the sling fitted with rubber isolation pads, in order to reduce its vibration.
The purpose of the counterweight is to balance a part of the weight of the elevator car assembly and, consequently, to reduce the machine torque requirements.
Some elevator systems are equipped with compensation ropes to reduce or eliminate

the effect of the varying mass of the hoist ropes as the elevator moves in the shaft, thereby reducing variations in the motor current.
The car assembly moves vertically constrained by two guide rails, sliding or rolling along them.
According to the roping arrangement and to the ratio of the tangential velocity of the traction sheave to the velocity of the car, the traction elevators can be classified as roped 1:1 or multiple reeving systems. The type of elevator system examined in the present work is a 1:1 traction elevator as shown in Fig. 1.1.

1.3 Ride quality

One of the main problems in elevator systems is to achieve and maintain adequate ride quality standards. In the 19nth century, passenger comfort was not thought of as an important item for elevators; if it is considered the motor car industry of that time, the cars were open, with no heating, and very noisy, very different from today. The elevator industry, and building owners remained stagnated in this position for over 100 years after Elisha Otis gave his revolutionary demonstration, in that elevator ride quality was not a major concern as it did not have an affect on sales or maintenance revenues.
It was not until the last quarter of the 20th Century did the concept of Elevator ride quality start appearing in specification documents. The Japanese Elevator industry had basic ride quality requirements in place during the early 1980's due to the cultural demands of the Japanese population. These Japanese concepts started to be incorporated into international building owners and elevator consultants' specifications with varying degrees of success.
Some elevator consultants' specifications attempted to incorporate very detailed testing procedures using highly complex testing and recording instruments which also required highly skilled technicians to operate, keep the instrumentation in calibration and understand the data and results obtained.
To enable a Worldwide method of standardized elevator testing of ride comfort an ISO Standard for elevators (Measurement of lift ride quality ISO 18738) (1) was published in 2003. This standard provides an International standardised method of testing and recording elevator ride quality, as well as standardised terms and definitions, measuring instrumentation, evaluation of ride quality, procedures for measuring ride quality and

reporting of results. It does not specify acceptable or unacceptable ride quality. More information on measurement of elevator ride quality can be found in (2, 35, 36).

Ride quality is the term that stands for the following set of aspects: jerk, car acceleration, vertical car vibration, lateral car vibration and sound inside the car.

The jerk (m/s^3) is the time-derivative of acceleration. If the elevator moves with high jerk, acceleration changes are very abrupt and can be felt as bumps.

The car acceleration (m/s^2) determines how long it takes before the car reaches its maximum speed. A high acceleration is generally considered uncomfortable, however, it gives the impression that the car moves very fast.

The vertical car vibration is also measured as acceleration and can be felt by the feet of a person, but is also discerned by the stomach and the internal ear. It is mostly caused by vibrations of the drive and frequency converter. These are transferred to the car by the traction media.

The lateral car vibration is caused by non-straightness of the guide rails, play between car and guide rails and non-smooth guide rail transitions. Generally, it causes low-frequent lateral movements of the car.

Finally, the sound level in the car should be low enough not to interfere with speech, but hearing the elevator in motion is desirable from a psychological point of view.

More information about the sources of vibration in elevator systems can be found in (9). Typical values of unacceptable acceleration and jerk are given in (21).

Concerning vibration, the standard ISO 18738 defines the ISO-weighted Maximum Peak-to-Peak vibration value (ISO MPtP) and the ISO-weighted A95 vibration value (ISO A95) (95% of all peaks of the ISO-weighted signal are below it) to evaluate the ride performance of an elevator, based on the acceleration time signal measured inside the car during a travel. The spectrum of the acceleration signal provides additional information to asses ride performance.

High-rise buildings in modern cities require high-speed elevator systems to provide quick access within them. Speeds up to 16 m/s have been achieved and if the velocity is to be increased the technology of elevators will require a revolution to accomplish the goal. Acceptable levels of vertical and lateral vibrations in high-speed elevators are very small (53). Therefore, vibration suppression schemes are required.

1.4 Dynamics of elevators

An elevator is a complex structure, described in Section 1.2. Next, the particularities of its dynamics are briefly described.

1.4.1 Ropes

Hoist ropes, due to their flexibility, loading conditions, and relatively low internal damping characteristics, mainly determine the resonances within the system and, therefore, the level of longitudinal and lateral vibration in the elevator system. There are additional resonance frequencies associated with particular components of the elevator such as the car frame.

Excessive vibration of suspension and compensating ropes affect substantially elevator system performance, as it induces high level dynamic stresses which cause excessive friction wear and, consequently, shortening of the safe service life of the rope (25). Besides, particularly in high-rise systems, vibration amplitude may reach large values, that lead to mechanical breakdowns of the equipment and a disruption of the elevator operation.

Ropes are axially moving continua with time-varying lengths. Therefore, their dynamic characteristics vary during travel, rendering the system non-stationary. Moving slender continua are inherently non-linear and they undergo non-linear resonance and modal interaction phenomena, as modal interactions between the lateral and longitudinal oscillations and the car motions (55).

When any excitation frequency coincides with one of the natural frequencies of the rope transient resonance phenomena occur (28).

1.4.2 Drive system

The drive system comprises the traction sheave and the corresponding motor powered via an inverter. The motor shaft speed is controlled in order for the car to follow a prescribed velocity profile to achieve good ride quality. The traction sheave sets in motion the car-rope and the counterweight-rope subsystems.

The drive system is as well a source of vibration; oscillations in the torque exerted by the motor or irregularities in the traction sheave, as imbalance, are cause of comfort deterioration. Smooth performance of the drive system is fundamental to comfort in

an elevator car.

Measurements in rotary machines have been carried out in order to detect imbalance or defects in bearings or gears (6) and a number of control algorithms have been proposed (20) to improve the comfort in elevators.

1.4.3 Guide rails

A key component of the elevator hoistway are the guide rails that constrain the lateral motion of the elevator car. Guide rails flexibility or inaccuracy in their installation mainly cause lateral vibration. Therefore, steps at the guide joints, uneven or curved rails, bending (the lowest excitation frequency due to bending corresponds to the velocity of the elevator divided by the length of the rail), and worn or flattened rollers, if it is the case, excite lateral vibration. Measuring devices have been developed to asses inaccuracies in the guide rails (18, 47).

1.4.4 Car

The car is a complex structure (see Fig. 1.2) that undergoes lateral and vertical vibration. The response of the cab and frame to excitation forces from the rails-rollers (or -shoes) interaction can be represented using multibody dynamics. The behaviour of the transmission path from the guide rail to the car depends mainly on the mass, flexibility and damping characteristics of the guide rollers or shoes and the car frame.

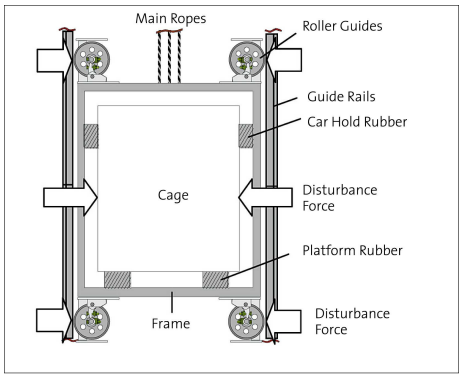

Figure 1.2: Elevator car (Reprinted from (14))

Simple multibody models of the car have been developed to study and reduce lateral (56) and longitudinal (19) vibration. Vibration test equipment system using full-size

cars have been developed in order to test the good performance of the proposed vibration control systems (39, 66).

1.5 Aim of the thesis

At this stage of the thesis report, it will be roughly stated what the aim of the research is, although more precise primary and secondary objectives will be set once a comprehensive literature review is done.
The research work will focus on one of the aspects of ride quality mentioned in Section 1.3: vertical vibration, particularly, that one associated with the suspension ropes.
As mentioned in Section 1.3, the origin of vertical vibrations can be usually found at the drive system. The electrical motor interconnects and sets in motion the car- and the counterweight-side subsystems, but it is as well a source of vibration; particularly, the torque generated by the machine is not smooth but includes a ripple that causes the elevator car to vibrate.
In this research, car vibration at torque ripple frequencies will be investigated. Thus, the primary objective of the thesis can be stated as:

"**The analysis of machine generated elevator car vertical vibrations**"

1.6 Outline of the thesis

Chapter 1 presents a brief introduction to the elevator industry, the company Orona and its research activity, a short history of elevators, ride quality as one of the elevator industry concerns and the characteristics of the dynamics of elevator systems. It states roughly the aim of the thesis research.
Chapter 2 discusses and assesses the literature related to the aim stated. The review focuses particularly on the dynamics of the suspension ropes and the drive system, on elevator system modelling and testing. It is critically appraised the literature about vertical, lateral or coupled vertical-lateral vibrations, about stationary or non-stationary either distributed- or lumped-parameter models.
In Chapter 3, the primary and secondary objectives to be achieved in the research work are set and the methodology that will be applied to accomplish them described.

In Chapter 4 distributed- and lumped-parameter models of an elevator with a 1:1 roping configuration are developed to calculate the natural frequencies and corresponding mode shapes. The values of the parameters of a particular laboratory model are used to calculate the values of natural frequencies and mode shapes by all the developed models. The results are compared and some conclusions obtained.

In Chapter 6, a number of tests are carried out on a 1:1 roping configuration laboratory model. The rope elasticity modulus is estimated from some of them. Other tests consist of measuring the acceleration response at the suspended masses and at the drive machine, the machine shaft velocity and the three phase current intensities supplied to the machine during several travels. The machine torque is estimated from the current intensities. Viscous friction at the guide-rail contact and at the machine are estimated. The measured and simulated acceleration responses, either in time or frequency domain, are compared and it is shown that the elevator car vibrates at frequencies generated at the machine, especially when they are close to the system natural frequencies.

Chapter 7 focuses on the vertical vibration of a 2:1 roping configuration elevator. A mathematical model is developed to calculate the natural frequencies of the system. A laboratory setup is used to carry out some experimental tests. The simultaneous accelerations of its main components are recorded during a travel. The frequency content and the corresponding amplitudes of the torque ripple generated by the setup traction machine are calculated by a FEM software. The experimental results are interpreted according to the expected natural frequencies of the system and the electromagnetic simulation results.

Finally, Chapter 8 summarises all the work done and the conclusions obtained.

2

Literature review

2.1 Outline

According to the aim stated in 1.5, this review will focus particularly on the literature that reports the dynamics of elevators where the suspension and drive systems play a significant role.

Ropes will be the only suspension system to be studied. Other suspension systems, as belts (49), will not be examined.

Particular attention will be paid to the mathematical models developed and the experimental tests performed to check their availability.

The car and the guide rails dynamics was described briefly in Sections 1.4.4 and 1.4.3 and will not be the focus of this review.

After a comprehensive review of the literature, it has been observed that, under some assumptions, depending on the issue to analyse, the coupling between lateral and longitudinal vibrations of the suspension ropes is neglected. The topics where the elevator longitudinal and lateral vibrations are modelled independently are described in 2.3. First, vertical vibration cases are described. Either distributed-parameter or lumped-parameter models are presented, either stationary or non-stationary. Next, lateral vibration is the topic examined. In some cases, the models developed are non-stationary and the axial transport velocity is prescribed; in some others, the drive system dynamics is included.

Lateral vibration in compensation ropes is as well a cause for concern in the elevator industry and is superficially described in section 2.3.

Coupling between the lateral and longitudinal vibration will be the issue studied in 2.4.

2.2 Elevator systems

Elevators are axially translating media with time-varying length. Wickert and Mote (64) shown that there is a critical transport velocity, that depends on the rope tension, at which divergent instability occurs. Kaczmarczyck and Andrew (28) defined the following dimensionless parameter to asses the variability rate of the rope lengths

$$\varepsilon = \frac{V}{\omega_0 l_0} \tag{2.1}$$

where V is the elevator rated speed, ω_0 denotes the lowest natural frequency and l_0 the corresponding length of the rope. In the case of hoist ropes in elevator systems, $\varepsilon << 1$ and it can be stated that the system natural frequencies vary slowly with time, but it is not so small for the case of compensation ropes due to their low tension (28).
Depending on the scope of the dynamic phenomena chosen to study, various simplifications are made when modelling an elevator system.
One approach considers it as a translating assembly of one-dimensional distributed subsystems carrying lumped inertia elements at the ends, and acting together as a single system due to constraints imposed between adjacent subsystems. The inertia elements are the car assembly, the counterweight, the traction sheave and other rotating components of the system. The one-dimensional slender continua are the suspension ropes that vibrate laterally and vertically and have time-dependent length.
Therefore, the entire system is non-stationary and its response can be described by a system of PDEs, derived from Hamilton's principle (38) of the form (58)

$$\begin{aligned} &\mu_i(x)\mathbf{u}^i_{tt} + \mathbf{C}^i\left[\mathbf{u}^i_t\right] + \mathbf{L}^i\left[\mathbf{u}^i\right] = \mathbf{N}^i\left[\mathbf{u}^i\right] + \mathbf{f}^i{}_{(x,t,\theta_i)} \\ &x \in D_i(t),\ 0 \leq t < \infty \end{aligned} \tag{2.2}$$

where $i = 1, 2, \ldots$ indicates the component number, $\mu_i(x)$ a local mass distribution function, $\mathbf{u}^i{}_{(x,t)}$ is a local (component) displacement vector representing the motion of the component i, and $\mathbf{C}^i$ and $\mathbf{L}^i$ are local linear operators. $\mathbf{N}^i$ is an operator acting upon the global displacement vector that represents non-linear couplings and inter-component constraints in the system. $\mathbf{f}^i$ is a forcing function with harmonic terms of

frequency $\dot{\theta}_i = \Omega_i$. D_i represents a local time-variant spatial domain defined as $D_{i(t)} = \{x : 0 < x < l_{i(t)}\}$, where $l_{i(t)}$ represents the time-varying length of the component i.
The set of PDEs 2.2 can be discretised by series methods (Rayleigh-Ritz, Galerkin...) (38), where the solutions are expanded in terms of the modes of the corresponding linear stationary system. This procedure results in a system of ordinary differential equations (ODE).
Alternatively one can seek the approximate solution to the PDE set using asymptotic (perturbation) methods (23, 30, 58, 59).

2.3 Vertical-lateral vibration coupling neglected

It is often assumed that if the amplitude of the lateral vibration is small, the coupling between the vertical and the lateral vibration can be neglected; thus, vertical and lateral vibration are studied independently (28). The higher the rope tension is (it depends on the suspended mass), the smaller it is the amplitude of the lateral vibration, and the more adequate this approach.

2.3.1 Vertical vibration

Next, several possibilities to model the vertical dynamics of an elevator are reported as well as experimental tests carried out to validate them. A summary of the models to develop depending on the axial velocity of the elevator was proposed by Vladic et al. (63).

2.3.1.1 Car-ropes subsystem distributed parameter models

Another simplification is to consider the car- and counterweight-side subsystems separately in the analysis. It is a consequence of assuming that the drive control system allows an accurately prescribed motion of the traction sheave to be realized (31).
As previously stated (see Section 2.2), the parameters of the elevator system vary slowly with time (28) but in the analysis they can be considered to be constant with the car frozen at a certain position. In this case, the system can be modelled by a differential equation that has got an analytical solution and the natural frequencies and modes of either the vertical or the lateral vibration can be determined as a closed-form solution solving Eqn. 2.2.

Chi and Shu (10) calculated the longitudinal natural frequencies of a hoist rope of constant length and three lumped masses (car frame, cabin and hitch device coupling the car frame to the rope) connected by springs for various boundary conditions at the top end (see Fig. 2.1). Kaczmarczyk and Andrew calculated the longitudinal and lateral natural frequencies of the car-side subsystem modelling it as a fixed-free rod of constant length carrying a concentrated mass at its free end (28).

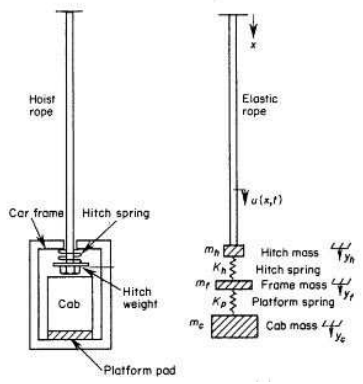

Figure 2.1: Hoist rope of constant length and three lumped masses (Reprinted from (10))

2.3.1.2 Lumped parameter models

When the whole assembly of distributed subsystems is considered, the suspension rope can be represented by a lumped-mass model with point masses joined by springs and dampers with the corresponding stiffness and damping values. Such models are described by a set of ODEs. The number of discrete mass points corresponds to the number of degrees of freedom (DOF) of the system and to the number of natural frequencies and mode shapes that are considered. Eqn. 2.2 is reduced to a set of ordinary differential equations (ODE) of the form

$$\mathbf{M}\ddot{\mathbf{q}}(t) + \mathbf{C}\dot{\mathbf{q}}(t) + \mathbf{K}\mathbf{q}(t) = \mathbf{f}(t) \tag{2.3}$$

where $\mathbf{M}, \mathbf{C}$ and $\mathbf{K}$ are the mass, damping and stiffness matrices respectively. $\mathbf{q}(t)$ is the vector of translational displacements with respect to the equilibrium position (angular displacements for lumped pulleys or sheaves) and $\mathbf{f}(t)$ the vector of forces (torques for pulleys). The values of these matrices are a function of the position of the car.
A number of models of this kind have been considered in the literature, from just 3

DOF, in order to control longitudinal vibration (57), up to 11 DOF (40) or 27 DOF for high speed elevators (53) (see Fig. 2.2). Zhou compared a lumped longitudinal model of 8 DOF with a Finite Element Analysis (FEA) model (where the ropes are taken as distributed parameter media) and concluded that the FEA model should be used to study the elevator hoistway vertical dynamics in high buildings (70).

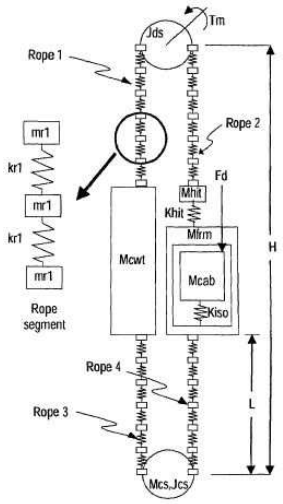

Figure 2.2: Lumped-parameter model (Reprinted from (53))

Mei et al. (37) developed a 9 DOF model of a 2:1 roping configuration elevator (see Fig. 2.3) and proposed a parameter optimisation method to minimise car acceleration. A lumped-parameter model enables to simulate the vertical vibration during a travel by updating its parameters at every time step. A number of papers account for the time-variability. For instance, in order to control vertical vibration, Venkatesh et al. (61) represented the elevator hoistway dynamics as a parameter-varying linear state space model, whose parameters were identified according a certain methodology (62); Arakawa and Miyata (5) proposed a new algorithm to suppress the first mode longitudinal vibration of a high speed elevator; Fukui et al. (13) developed a detection system to avoid emergency stop procedures due to car forced vibration caused by passenger mischief; Aldaia et al. (3) included a time-varying lumped-parameter model of the ropes in a more complex one composed of interconnected parts (machine room, ropes, cabin and counterweight) that interchanged energy through their connections; Herrera (19)

shown that acceleration response was highly influenced by even the mass and damping and stiffness characteristics of passengers by a 6-DOF eleveator model.

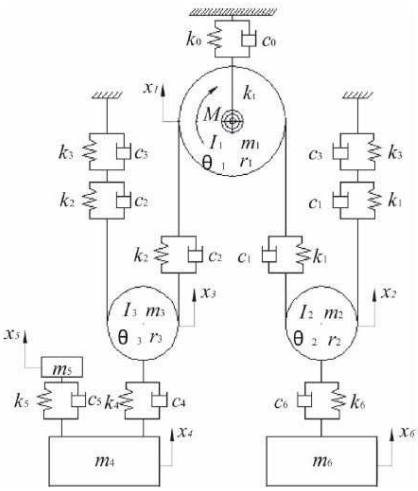

Figure 2.3: Lumped-parameter model of a 2:1 roping cfg. elevator (Reprinted from (37))

2.3.1.3 Experimental tests

There have been some attempts to identify the dynamic behaviour of the elevator by experimental tests.

Roberts (53) tried to validate its 27 DOF model calculating the transfer function between the recorded velocities of the car and the traction sheave for different lengths of the ropes.

Nai et al. (41) obtained experimental Frequency Response Functions (FRF) between the sling and the sheave and between the car floor and the sling and identified resonance frequencies of the ropes and the isolation pads.

Emory et al. (11) calculated the longitudinal and lateral natural frequencies of a simplified aramid suspension rope-elevator car system and analysed how rope terminations or the wrapping around the sheave affected their values; they concluded as well that longitudinal vibration of two rope sections jointed by a sheave are coupled while lateral vibration was almost uncoupled.

2.3.1.4 Non-stationary models of an assembly of distributed subsystems

Kaczmarczyk and Ostachowicz (23, 30) investigated transient resonance phenomena in mine hoisting ropes. The overall response of a hoisting rope system to inertial load due to transport motion acceleration/deceleration and to harmonic excitation was studied by means of distributed-parameter models (see Fig. 2.4). It was assumed that the drive control system allowed an accurately prescribed motion of the traction sheave to be realized. The PDE set was solved by a combined perturbation and numerical technique.

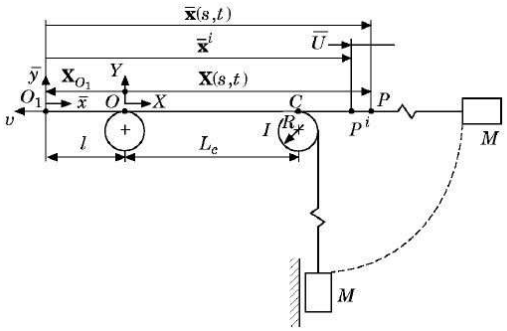

Figure 2.4: Catenary-vertical rope system (Reprinted from (23))

Zhang et al. (69) proposed a controller to dissipate the vibratory energy of an elevator modelled as a mass driven by two flexible ropes with motors fixed at both ends.

2.3.2 Lateral vibration

Particularly in high rise buildings, lateral vibration of ropes can achieve large amplitudes, hit the hoist walls and cause damage in the elevator installation. This is why a lot of research works on lateral vibration of ropes have been reported.

2.3.2.1 Lumped-parameter models

Nakagiri (42, 43) calculated lateral natural frequencies by means of a lumped-parameter model (see Fig. 2.5) where the rope was decomposed in a series of rigid links interconnected by torsion springs.

Otsuki eta al. (44, 45, 46) proposed several control methods to suppress lateral vibrations of elevators represented by lumped-parameter models.

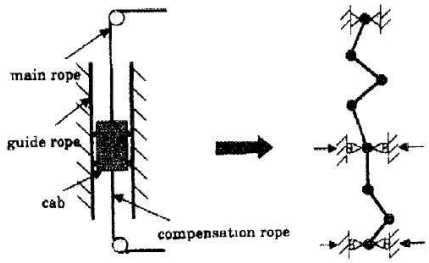

Figure 2.5: Lumped-parameter model for lateral vibration (Reprinted from (42))

2.3.2.2 Axial velocity prescribed non-stationary lateral vibration models of the car-ropes subsystem

Kotera (33) analysed the free lateral vibrations of the hoist rope of a mining elevator represented as a concentrated mass at the free end and axially moving with a constant velocity (see Fig. 2.6); the displacement of both ends was zero for any time t.

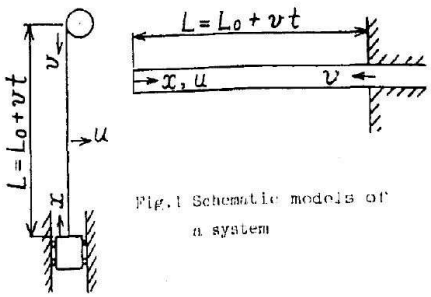

Figure 2.6: Distributed-parameter model for lateral vibration (Reprinted from (33))

Yamamoto et al. (65) investigated the free and forced vibrations of a string of slowly time-varying length. Passages through resonance were studied and it was observed and experimentally checked (see Fig. 2.7) that the vibration maximum amplitude occurred at a slightly lagged position from the resonance point and that the lag depended on the string transport velocity.

Zhu and Ni (75) investigated the dynamic stability of the lateral vibration of vertically moving beams and strings with time-varying length and various boundary conditions from the energy standpoint. They concluded that the energy of vibration of an undamped, uniformly accelerating or decelerating medium decreases and increases

monotonically during extension and retraction, respectively (the "unstable shortening rope behaviour" observed in the elevator industry) and that special jerk functions could stabilise the translating medium.

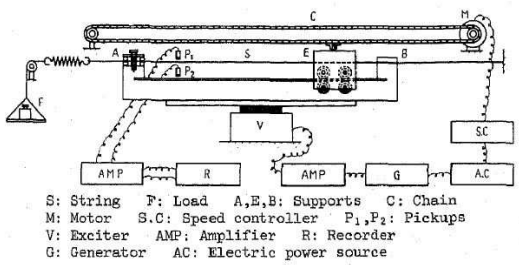

Figure 2.7: Experimental setup to investigate lateral vibration resonance phenomena (Reprinted from (65))

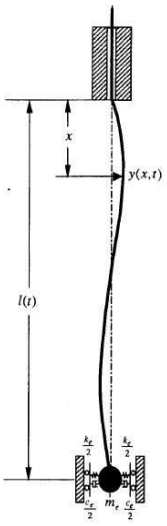

Figure 2.8: Vertically moving string lateral vibration (Reprinted from (75))

An active control methodology using a pointwise control force and/or moment was developed by Zhu eta al. (73) to dissipate vibratory energy of translating media with variable length.

Zhu and Xu (77) investigated the effects of bending stiffness and boundary conditions on the dynamic characteristics of hoist ropes and identified the optimal stiffness and damping coefficient of the suspension of the car against its guide rails for the moving

rope.

Zhu and Chen (8, 71) determined the lateral response of rope-car systems in high-speed elevators for general initial conditions and external excitation that arises from building sway, pulley eccentricity, and guide-rail eccentricity. They showed that the vibratory energy of the rope is usually much higher than that of the spring-suspended mass subsystem.

Zhu and Chen (72) presented a control method to dissipate the vibratory energy associated with the lateral vibration of the rope and validated it by experimental tests performed on a novel small-scale within limiting factors laboratory model (76) (see Fig. 2.9).

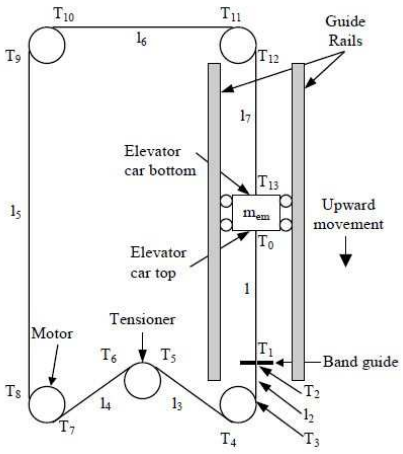

Figure 2.9: Schematic of the setup (Reprinted from (76))

Kaczmarczyk investigated the guide rail excitation mechanism and its influence on car ride quality (24). He also solved the equations describing the lateral response due to a boundary periodic excitation (25) and proposed the integration of shape memory alloy elements within the suspension rope design to suppress lateral vibration.

Kaczmarczyk and Ostachowicz analysed the response of an elevator to stochastic guide rail excitation (29).

Gang et al. (16) showed that the horizontal vibration behaviour is closely interconnected with the location, velocity and acceleration of the elevator cab by means of a model based on the wave theory of one-dimensional string vibration.

Kimura et al. (32) investigated the response of an elevator to building sway and found

the exact solution to the forced vibration of a rope where both ends (the car and the traction sheave) are moving, based on the assumption that rope tension and movement velocity were constant and that the damping coefficient of the rope was zero.

2.3.2.3 Drive system dynamics included

Fung et al. (15) reported a control strategy to suppress the transient amplitudes of lateral vibration of a moving elevator string with time-varying length that was coiled around a rotor driven by a permanent magnet synchronous servo motor (see Fig. 2.10). The axial velocity of the elevator was not prescribed. The mass and inertia of the rotor were time-dependant due to the winding of the string either on or off it.

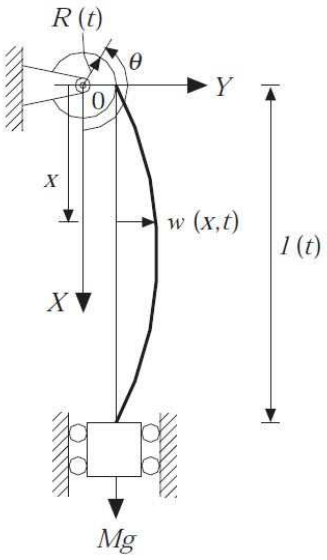

Figure 2.10: Machine included elevator system (Reprinted from (15))

2.3.2.4 Compensation ropes

A number of papers focus on the lateral vibration of compensation ropes. Compensation ropes are subjected to low tensions and suffer from large amplitude low-frequency vibrations. Blodgett and Majumdar (7) analysed lateral vibrations of compensation ropes caused by heavy wind in tall buildings by means of a model that consisted of a hanging rope excited by an oscillation at the upper end and having a weight suspended at the lower end. The effect of introducing a damper at the upper end in order to limit

the vibration was also examined.

Kaczmarczyk developed a model that accounted for the influence of centrifugal forces as well as the Coriolis and lift profile acceleration terms to investigate the fundamental features of the dynamic response of compensating ropes in a building subjected to excitation caused by adverse environmental phenomena (26). He proposed how to avoid the resonance phenomena that occur when excitation frequencies due to building sway coincide with the natural frequencies of the ropes.

Zhu (74) developed a non-linear planar model of a slack cable (see Fig. 2.11) with bending stiffness and arbitrarily moving ends for either compensation ropes or travelling cables and validated it by experimental tests carried out in a laboratory setup (76) (see Fig. 2.9).

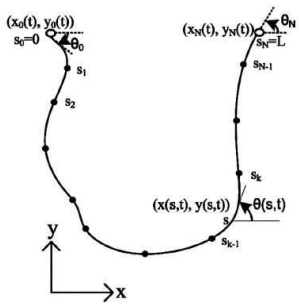

Figure 2.11: Slack cable (Reprinted from (74))

2.4 Coupled vertical-lateral vibration

All the models that have been developed up to this point in this literature review have dealt with either the vertical or the lateral vibration, and they have resulted accurate enough to simulate certain characteristics of the elevator dynamics. Nevertheless, there arise situations where longitudinal and lateral vibration coupling occurs.

Zhang et al. (68) investigated the lateral vibration of a mass-loaded string (see Fig. 2.12) due to the parametric excitation caused by an external harmonic disturbance applied to the mass in the vertical direction. They validated the simulation results experimentally (see Fig. 2.13) and shown that one of the cases of parametric resonance may occur under a small vertical disturbance when the vertical natural frequency is close to twice the lateral natural frequency. Zhang et al. proposed and validated a

strategy to suppress this parametric resonance based on tuned-mass dampers (67). Terumichi et al. (59) studied the non-stationary vibration of a string with time-varying length and a mass-spring system attached at the lower end (see Fig. 2.14). The string top end was excited sinusoidally by a horizontal displacement and the suspended mass had two degrees of freedom, vertical and horizontal. It was shown analytically and experimentally (see Fig. 2.15) that the axial velocity of the string influenced the vibration amplitude of the string and the mass at the passage through resonances.

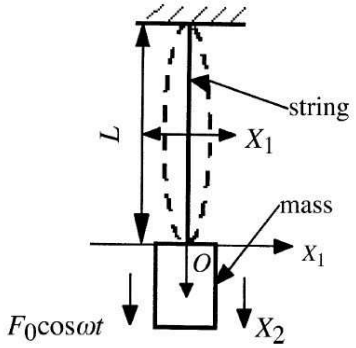

Figure 2.12: Mass-loaded string system (Reprinted from (68))

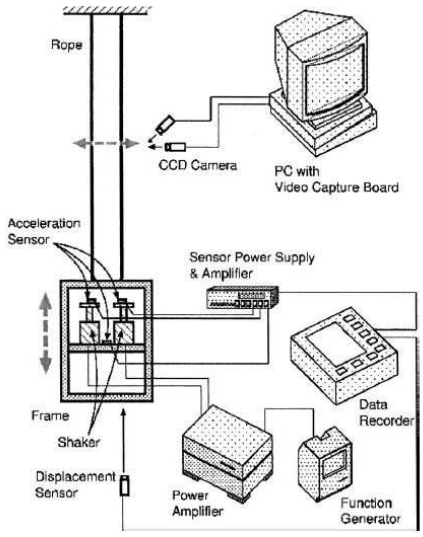

Figure 2.13: Schematic diagram of the experiment system (Reprinted from (68))

Kaczmarczyk et al. (27) investigated the influence of building lateral vibrations on the

dynamic response of hoists ropes by means of a model that consisted of a hoist rope moving axially with a prescribed velocity and with a mass attached to the free end. It was shown that the building sway results in a distributed inertial load acting upon the hoist ropes which in turn may lead to resonance and modal interactions between the lateral modes and the fundamental longitudinal mode.

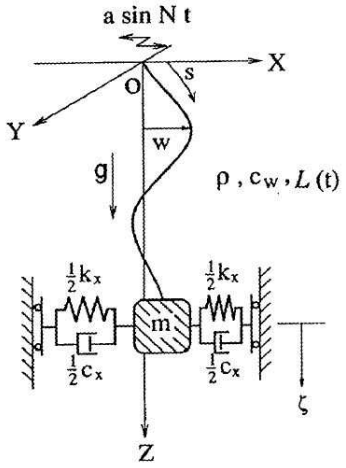

Figure 2.14: Elevator model (Reprinted from (59))

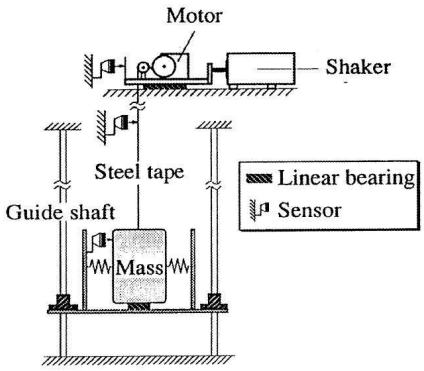

Figure 2.15: Experimental setup (Reprinted from (59))

Salamaliki-Simpson et al. (54) developed a stationary model of an elevator car-hoist rope assembly to investigate the response to three dimensional kinematic excitation applied to the drive sheave end; the numerical simulation results demonstrated that autoparametric 2:1 resonance between the longitudinal and lateral modes occurs due

to nonlinear quadratic coupling between the modes.
Ren and Zhu developed a spatial discretisation and substructure method (51) to study the longitudinal, lateral and coupled vibrations of moving elevator car-rope systems (52).

2.5 Conclusions

As it was stated in Section 1.5, the focus of the thesis is the analysis of elevator car vertical vibrations generated at the machine.
The literature review shows that the coupling between the vertical and the lateral vibration has often been neglected, particularly when the amplitude of the lateral vibration is small, and that consequently the elevator vertical vibration has been modelled independently. It is an approach that does not account for any of the dynamic issues described in Section 2.4. This thesis will deal with elevator vertical vibration caused by vertical excitation forces due to the torque ripple generated at the machine; thus, it will be developed a mathematical model of an elevator to study only vertical vibration.
Another approach reported in the Literature consists of lumping the inertia elements (the car assembly, the counterweight and the traction sheave) at its corresponding points and considering the elevator system as a translating assembly of these inertia elements coupled and constrained by one-dimensional slender continua. This approach involves not considering dynamic issues such as those described in Section 1.4.4 and will also be assumed in this thesis.
Another simplification reported considers the car- and counterweight-side subsystems separately in the analysis, as a consequence of assuming that the drive control system allows an accurately prescribed motion of the traction sheave to be realized. However, as this thesis will deal with excitation forces generated at the machine, that couples the car- and counterweight-side ropes through the traction sheave, it has been decided to develop a model of the whole assembly, including the car, the counterweight, the ropes and the drive system. A common drive system model, reported in the related literature, will be developed.
To summarise, it will be developed a mathematical model to describe the vertical vibration of the car-counterweight-sheave-ropes assembly with all inertia components lumped at their locations. A model of the drive system will be included as well. The

input to it will be a desired reference velocity profile to be followed by the car.
The ropes are distributed-parameter media. Vertical vibration either distributed- or lumped-parameter models of elevators have been reported. In the case of LPMs, the suspension rope is approximated by a lumped-mass model with point masses joined by springs and dampers with the corresponding stiffness and damping values. From a mathematical point of view, the LPM is described by a set of ODEs (Eqn. 2.3) that has got a closed-form solution (the eigenvalue problem) whereas the DPM is described by a set of PDEs, that is usually solved by spatial discretisation methods such as Galerkin. The Galerkin method has been extensively applied to solve the PDE sets that describe the dynamics of DPMs of not only vertical but also lateral and coupled lateral-vertical vibrations. Both approaches will be worked out in this thesis.
With respect to experimental tests, acceleration inside the cabin or certain frequency response functions have been obtained in elevator installations, as described in Section 2.3.1.3, but it is more frequent to find specifically designed setups, such as those described in Section 2.4, in order to test a certain characteristic of the elevator dynamics. A real elevator installation is complex enough to difficult obtaining conclusions on certain features of its dynamics.
The influence of the machine generated torque ripple in elevator car vertical vibration has not been specifically studied and reported in the literature. Regarding this issue, some questions can be formulated: how large is the amplitude of the torque ripple? what is the frequency content of it? which of these excitation frequencies are apparent on the cabin floor? These are the question that this thesis will try to answer.

3

Objectives and methodology

The main objective was stated in Section 1.5 as

"**The analysis of machine generated elevator car vertical vibrations**"

The main objective has been divided in some secondary objectives. Next, these secondary objectives are established and the methodology planned to achieve them described.

1. To calculate the natural frequencies and mode shapes of an elevator with a 1:1 roping configuration.
   It will be assumed that all inertia elements are lumped at their corresponding points, that the rope material is uniform, that the sheave is perfectly rigid and that there is no rope slip across the sheave, and only longitudinal motion will be admitted in the car-rope and counterweight-rope subsystems.

   (a) To elaborate a distributed-parameter model of a system that consists of three masses constrained by a rope of fixed length.
   Hamilton's principle will be applied to derive the PDE set describing the dynamics. A closed-form solution will be searched for.

   (b) To elaborate a lumped-parameter model of a system that consists of three masses constrained by a rope of fixed length.
   The suspension rope will be represented by a lumped-mass model with point masses joined by springs and dampers with the corresponding stiffness and damping values. The resulting eigenvalue problem will be solved.

(c) The natural frequencies and mode shapes obtained by both models will be compared and the pertinent conclusions will be drawn.

2. To develop a model to simulate the acceleration response of an elevator with a 1:1 roping configuration to excitation generated at the machine.
   The model will be implemented in the MATLAB/Simulink computational environment.

   (a) To develop a model of the drive system that comprises a permanent magnet synchronous motor powered via an inverter that supplies a pulse width modulated (PWM) voltage.
   The well known direct quadrature zero (dqo) mathematical transformation will be applied to simplify the analysis of the three-phase synchronous machine.
   A common vector control strategy oriented to the magnets flux will be implemented to control the motor shaft speed in order for the car to follow a prescribed velocity profile to achieve good ride quality.

   (b) To compute the machine parameters by means of the Finite Element Method simulation software FLUX and to estimate the amplitudes of the main frequency components of the torque ripple.

   (c) To develop a non-stationary DPM of the car-counterweight-sheave-rope assembly.
   The application of Hamilton's principle will provide the PDE set describing the dynamics. Galerkin method will be applied to discretise it by expanding the vertical displacements in terms of the linear stationary mode shapes of the system composed of three masses constrained by the suspension rope.

   (d) To develop a non-stationary LPM of the car-counterweight-sheave-rope assembly.

   (e) To simulate and compare the car acceleration response during a travel by both the DPM and the LPM models and to draw the pertinent conclusions.

3. To validate the simulation model by experimental measurements performed in a laboratory model of an elevator.

(a) To perform measurements on a 1:1 roping configuration laboratory setup.
During several travels, the acceleration response at the suspended masses and at the drive machine, its shaft velocity and the three phase current intensities supplied to it will be measured. The machine torque will be estimated from the current intensities.

(b) To simulate the acceleration response of the system during a travel by means of both models, the DPM and the LPM.
The torque ripple estimated from the current intensities will be added to the controller generated torque as a perturbation. Simulation and experimental results will be compared and the pertinent conclusions drawn.

4. To calculate the natural frequencies and mode shapes of an elevator with a 2:1 roping configuration.
It will be assumed that all inertia elements are lumped at their corresponding points, that the rope material is uniform, that the sheave is perfectly rigid and that there is no rope slip across the sheave, and only longitudinal motion will be admitted in the car-rope and counterweight-rope subsystems.
A distributed-parameter model of the system will be developed. Hamilton's principle will be applied to derive the PDE set describing the dynamics. A closed-form solution will be searched for.

5. To perform experimental measurements in a laboratory model of an elevator with a 2:1 roping configuration.

(a) To compute the setup machine parameters by means of the Finite Element Method simulation software FLUX and to estimate the amplitudes of the main frequency components of the torque ripple.

(b) To observe the acceleration response of the car, the counterweight and the machine during several travels and to interpret it with relation to the developed model results.

6. To draw the conclusions of the thesis work.

4

Elevator 1:1 roping configuration

The natural frequencies and mode shapes of a stationary elevator with a 1:1 roping configuration are calculated in this chapter. The elevator is represented by a system that consists of three masses constrained by a rope of fixed length.
It is assumed that:

- The car, the counterweight and the traction sheave are lumped at their corresponding points.
- The rope material is uniform.
- The sheave is perfectly rigid and there is no rope slip across it.
- Only longitudinal motion is admitted in the car-rope and counterweight-rope subsystems.

Hamilton's principle is applied to derive the equations describing its dynamics. A closed-form solution is obtained and the natural frequencies and mode shapes calculated.
A lumped-parameter model of the system is developed as well. The suspension rope is represented by a lumped-mass model with point masses joined by springs with the corresponding stiffness values. The resulting eigenvalue problem is solved, the natural frequencies and mode shapes calculated and then compared to those obtained from the distributed-parameter model.
It is concluded that:

- The first three natural frequencies calculated using the DPM model and the LPM model compare very well (the first natural frequency is 0 Hz and corresponds to an overall transport motion of the system).

- At higher frequencies there are some differences between the results that are obtained from these models.
  It is demonstrated that if the rope is represented by a larger number of lumped masses so that the number of degrees of freedom in the LPM is increased, this model yields more accurate results with the differences between the frequencies calculated from the DPM and LPM being decreased.

- The car, the counterweight and the sheave are located at the nodes for all higher mode shapes from the 4th onwards.

4.1 Distributed-Parameter Model

A schematic representation of a traction elevator with a 1:1 roping configuration is shown in Fig. 4.1. A stationary inertial system Ox has been fixed at the centre of the traction sheave.
The hoist rope of mass density μ, elasticity modulus E and effective cross-sectional area A passes over the traction sheave. The mass of the car is m_{c}; the mass of the counterweight, m_{w}; the radius of the traction sheave is r; the length from the counterweight and car to the sheave l_{w} and l_{c} respectively; the total length of the rope is $l_{\mathrm{t}} = l_{\mathrm{w}} + l_{\mathrm{w}}$; and I the moment of inertia of the sheave and $m_{\mathrm{sh}} = I/r^2$ denotes the effective mass of the sheave.
The schematic shown by Fig. 4.2 is a system that consists of three masses constrained by a rope of fixed length (see Fig. 4.2). The position measured from the counterweight of any section of the undeformed rope is described by the variable s; t is the time. The counterweight- and the car-side rope subsystems are described by the intervals $0 \leq s \leq l_{\mathrm{w}}$ and $l_{\mathrm{w}} \leq s \leq l_{\mathrm{t}}$ respectively, where $s = 0$, $s = l_{\mathrm{w}}$ and $s = l_{\mathrm{t}}$ are the positions of the counterweight, traction sheave and car respectively. The displacement of any rope section in the counterweight- and car-side ropes are given by the functions $u_{\mathrm{w}}(s,t)$ and $u_{\mathrm{c}}(s,t)$ respectively.
Hamilton's principle is applied to obtain the following set of PDEs.

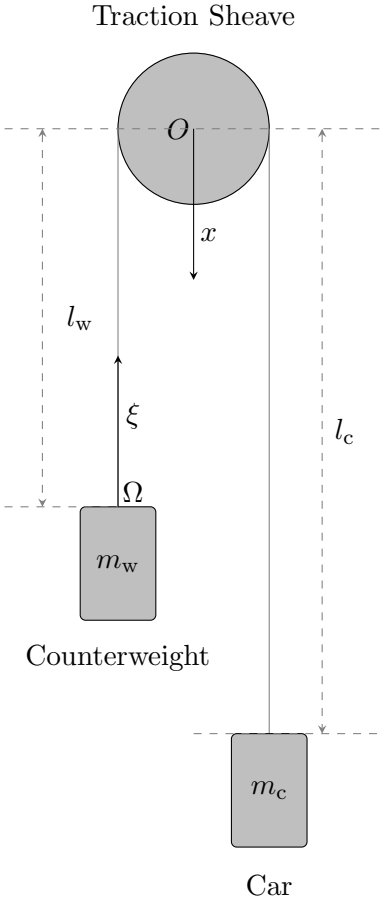

Figure 4.1: Schematic representation of a Lift System

$$\mu u_{w,tt} - EAu_{w,ss} = 0,\ 0 \leq s \leq l_w \tag{4.1}$$

$$\mu u_{c,tt} - EAu_{c,ss} = 0,\ l_w \leq s \leq l_t \tag{4.2}$$

$$m_w u_{w,tt}(0,t) - EAu_{w,s}(0,t) = 0 \tag{4.3}$$

$$m_c u_{c,tt}(l_t,t) + EAu_{c,s}(l_t,t) = 0 \tag{4.4}$$

$$m_{sh} u_{w,tt}(l_w,t) - EA\left[u_{c,s}(l_w,t) - u_{w,s}(l_w,t)\right] = 0 \tag{4.5}$$

The continuity of displacements requires that

$$u_{w,tt}(l_w,t) = u_{c,tt}(l_w,t) \tag{4.6}$$

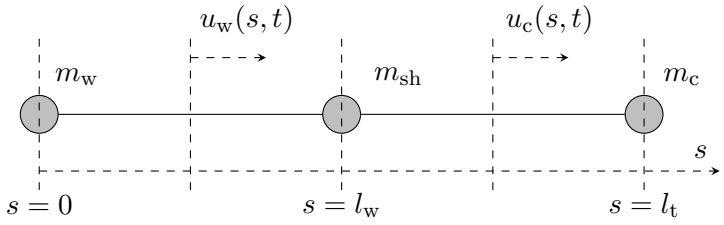

Figure 4.2: Three masses constrained by a rope of fixed length

It is searched a solution of the form

$$u(s,t) = q(t)\Phi(s, l_w(t)) \tag{4.7}$$

where $\Phi(s, l_w(t))$ are the mode shapes represented as

$$\Phi(s, l_w(t)) = \begin{cases} \Phi_w(s, l_w(t)), \ 0 \leq s \leq l_w \\ \Phi_c(s, l_w(t)), \ l_w \leq s \leq l_t \end{cases} \tag{4.8}$$

and the modal coordinate $q(t)$

$$q(t) = C\sin(\omega_i t + \varphi) \tag{4.9}$$

is a harmonic function of time and C an arbitrary constant.

4.1.1 Solving the equations

If the Eqn. 4.7 and its required derivatives are introduced into Eqns. 4.1 and 4.2, it results

$$\ddot{q}(t) + \omega^2 q(t) = 0 \tag{4.10}$$

$$\Phi_w'' + \gamma^2 \Phi_w = 0 \tag{4.11}$$

$$\Phi_c'' + \gamma^2 \Phi_c = 0 \tag{4.12}$$

$$\gamma^2 = \frac{\mu}{EA}\omega^2 \tag{4.13}$$

The mode shapes that satisfy Eqn. 4.11 have got the form

$$\Phi_{\mathrm{w}}(s) = C_1 \sin(\gamma s) + C_2 \cos(\gamma s) \tag{4.14}$$

$$\Phi_{\mathrm{c}}(s) = C_3 \sin(\gamma s) + C_4 \cos(\gamma s) \tag{4.15}$$

The continuity condition requires that

$$\Phi_{\mathrm{w}}(l_{\mathrm{w}}) = \Phi_{\mathrm{c}}(l_{\mathrm{w}}) \tag{4.16}$$

Introducing Eqn. 4.14 and its required derivatives, evaluated at $s = 0$, in Eqn. 4.3, it is obtained

$$C_2 = -\frac{\mu}{m_{\mathrm{w}}\gamma} C_1 \tag{4.17}$$

$$\Phi_{\mathrm{w}}(s) = C_1 g_1(\gamma, s) \tag{4.18}$$

$$g_1(\gamma, s) = \frac{\mu}{m_{\mathrm{w}}\gamma} \cos(\gamma s) - \sin(\gamma s) \tag{4.19}$$

We proceed in a similar manner with the Eqn. 4.15 and Eqn. 4.4 and it results

$$C_3 \left(\frac{\mu}{m_{\mathrm{c}}\gamma} \cos(\gamma l_{\mathrm{t}}) - \sin(\gamma l_{\mathrm{t}}) \right) = C_4 \left(\frac{\mu}{m_{\mathrm{c}}\gamma} \sin(\gamma l_{\mathrm{t}}) + \cos(\gamma l_{\mathrm{t}}) \right) \tag{4.20}$$

$$\Phi_{\mathrm{c}}(s) = C_4 g_2(\gamma, s) \tag{4.21}$$

$$g_2(\gamma, s) = \frac{\mu}{\gamma m_{\mathrm{c}}} \cos(\gamma(l_{\mathrm{t}} - s)) - \sin(\gamma(l_{\mathrm{t}} - s)) \tag{4.22}$$

Evaluating Eqns. 4.18 and 4.21 at $s = l_{\mathrm{w}}$ and introducing them into Eqn. 4.16, we get

$$C_1 g_1(\gamma, l_{\mathrm{w}}) = C_4 g_2(\gamma, l_{\mathrm{w}}) \tag{4.23}$$

The mode shapes must have the following form in order to satisfy the constraint 4.23,

$$\Phi_{\mathrm{w}}(\gamma, s) = C g_2(\gamma, l_{\mathrm{w}}) g_1(\gamma, s) \tag{4.24}$$

$$\Phi_{\mathrm{c}}(\gamma, s) = C g_1(\gamma, l_{\mathrm{w}}) g_2(\gamma, s) \tag{4.25}$$

where C is an undetermined constant value. If the derivatives of the mode shapes 4.24 and 4.25 are evaluated at $s = l_{\mathrm{w}}$, introduced into Eqn. 4.5, and the Eqns. 4.10 and 4.13 are used, the following expression is obtained

$$-g_1(l_\mathrm{w},\gamma)g_2'(l_\mathrm{w},\gamma)+g_2(l_\mathrm{w},\gamma)g_1'(l_\mathrm{w},\gamma)-\frac{m_\mathrm{sh}}{\mu}\gamma^2 g_1(l_\mathrm{w},\gamma)g_2(l_\mathrm{w},\gamma)=0 \tag{4.26}$$

where g_1', g_2' denote the derivative of g_1, g_2 respectively with respect to s.
The Eqn. 4.26, which is called the characteristic equation, is the constraint that the parameters γ must satisfy in order the Eqn. 4.7 to be a solution of the set of PDEs 4.1-4.5. That is to say, the roots of Eqn 4.26 determine the natural frequencies of the system described by the set of PDEs 4.1-4.5.
The mode shapes given by equations 4.24 and 4.25 are valid as long as $g_1(\gamma, l_\mathrm{w})$ or $g_2(\gamma, l_\mathrm{w})$ are not zero. At that case, the traction sheave is at a node, both rope sides are decoupled and their natural frequencies and mode shapes correspond to a rope with a suspended mass at one end and fixed at the other end.

4.1.2 Orthogonality conditions of the mode shapes

The mode shapes obtained satisfy some orthogonality properties. These properties are useful when applying spatial discretisation methods of PDE sets such as Galerkin, where these mode shapes are the basis for a series expansion that expresses the displacement of any rope section as a sum of terms of the form a time dependent coefficient multiplying a mode shape.
Let us consider the Eqn. 4.11 applied to the mode $\Phi_{\mathrm{w},j}(s)$ and use the Eqn. 4.13.

$$EA\Phi''_{\mathrm{w},j}+\omega_j^2\Phi_{\mathrm{w},j}=0 \tag{4.27}$$

If the Eqn. 4.27 is multiplied by the mode $\Phi_{\mathrm{w},i}(s)$ and then integrated from 0 to l_w (the counterweight-side rope length), it results

$$EA\Phi_{\mathrm{w},i}(l_\mathrm{w})\Phi'_{\mathrm{w},j}(l_\mathrm{w})-EA\Phi_{\mathrm{w},i}(0)\Phi'_{\mathrm{w},j}(0)-EA\int_0^{l_\mathrm{w}}\Phi'_{\mathrm{w},i}(s)\Phi'_{\mathrm{w},j}(s)\mathrm{d}s=$$
$$-\mu\omega_j^2\int_0^{l_\mathrm{w}}\Phi_{\mathrm{w},i}(s)\Phi_{\mathrm{w},j}(s)\mathrm{d}s \tag{4.28}$$

In a similar manner, let us consider Eqn. 4.12 applied to the mode $\Phi_{\mathrm{c},j}(s)$. If it is multiplied by the mode $\Phi_{\mathrm{c},i}(s)$ and integrated from l_w to l_t, it results

$$EA\Phi_{\mathrm{c},i}(l_\mathrm{t})\Phi'_{\mathrm{c},j}(l_\mathrm{t}) - EA\Phi_{\mathrm{c},i}(l_\mathrm{w})\Phi'_{\mathrm{c},j}(l_\mathrm{w}) - EA\int_{l_\mathrm{w}}^{l_\mathrm{t}} \Phi'_{\mathrm{c},i}(s)\Phi'_{\mathrm{c},j}(s)\mathrm{d}s = -\mu\omega_j^2 \int_{l_\mathrm{w}}^{l_\mathrm{t}} \Phi_{\mathrm{c},i}(s)\Phi_{\mathrm{c},j}(s)\mathrm{d}s \tag{4.29}$$

If the Eqn. 4.5 is applied to the mode $\Phi_i(l_\mathrm{w})$, it results

$$-EA\Phi'_{\mathrm{w},i}(l_\mathrm{w}) + EA\Phi'_{\mathrm{c},i}(l_\mathrm{w}) + m_\mathrm{sh}\omega_i^2 EA\Phi_{\mathrm{w},i}(l_\mathrm{w}) = 0 \tag{4.30}$$

If Eqn. 4.3 is applied to the mode $\Phi_i(0)$, it results

$$EA\Phi'_{\mathrm{w},i}(0) + m_\mathrm{w}\omega_i^2\Phi_{\mathrm{w},i}(0) = 0 \tag{4.31}$$

If Eqn. 4.4 is applied to the mode $\Phi_i(l_\mathrm{t})$, it is obtained

$$-EA\Phi'_{\mathrm{c},i}(l_\mathrm{t}) + m_\mathrm{c}\omega_i^2\Phi_{\mathrm{c},i}(l_\mathrm{t}) = 0 \tag{4.32}$$

If Eqn. 4.32 is introduced into Eqn. 4.29, Eqn. 4.31 into Eqn. 4.28, and the resulting expressions are added up, it is obtained

$$\begin{aligned} &EA\Phi_{\mathrm{w},i}(l_\mathrm{w})\left(\Phi'_{\mathrm{w},j}(l_\mathrm{w}) - \Phi'_{\mathrm{c},j}(l_\mathrm{w})\right) - \\ &EA\left(\int_0^{l_\mathrm{w}} \Phi'_{\mathrm{w},i}(s)\Phi'_{\mathrm{w},j}(s)\mathrm{d}s + \int_{l_\mathrm{w}}^{l_\mathrm{t}} \Phi'_{\mathrm{c},i}(s)\Phi'_{\mathrm{c},j}(s)\mathrm{d}s\right) = \\ &-\omega_j^2\left[\mu\int_0^{l_\mathrm{w}} \Phi_{\mathrm{w},i}(s)\Phi_{\mathrm{w},j}(s)\mathrm{d}s + \mu\int_{l_\mathrm{w}}^{l_\mathrm{t}} \Phi_{\mathrm{c},i}(s)\Phi_{\mathrm{c},j}(s)\mathrm{d}s + \right. \\ &\left. + m_\mathrm{w}\Phi_{\mathrm{w},i}(0)\Phi_{\mathrm{w},j}(0) + m_\mathrm{c}\Phi_{\mathrm{c},i}(l_\mathrm{t})\Phi_{\mathrm{c},j}(l_\mathrm{t})\right] \end{aligned} \tag{4.33}$$

If Eqn. 4.30 is introduced into Eqn. 4.33 and the symmetry of the resulting expression with respect to the indexes i and j is considered, we obtain the following orthogonality condition,

$$\begin{aligned} &\mu\int_0^{l_\mathrm{t}} \Phi_i(s)\Phi_j(s)\mathrm{d}s + m_\mathrm{w}\Phi_i(0)\Phi_j(0) + \\ &m_\mathrm{c}\Phi_i(l_\mathrm{t})\Phi_j(l_\mathrm{t}) + m_\mathrm{sh}\Phi_i(l_\mathrm{w})\Phi_j(l_\mathrm{w}) = \\ &\delta_{ij}\left[\mu\int_0^{l_\mathrm{t}} \Phi_i^2(s)\mathrm{d}s + m_\mathrm{w}\Phi_i^2(0) + m_\mathrm{c}\Phi_i^2(l_\mathrm{t}) + m_\mathrm{sh}\Phi_i^2(l_\mathrm{w})\right] \end{aligned} \tag{4.34}$$

where

$$\delta_{ij} = \begin{cases} 1, & i = j \\ 0 & i \neq j \end{cases} \tag{4.35}$$

4.2 Lumped-Parameter Model

Another approach to calculate the natural frequencies and mode shapes of the system is a lumped-parameter model, where not only the car, the counterweight and the sheave inertia are lumped at their corresponding positions but also the counterweight- and car-side rope masses are lumped at discrete points and then jointed to the sheave and counterweight, the sheave and the car, by mass-less springs of stiffness constant given by Eqn. 4.36 and Eqn. 4.37 respectively, for the case of a 5 DOF LPM (see Fig. 4.3).

$$k_{\mathrm{w}} = \frac{2EA}{l_{\mathrm{w}}} \tag{4.36}$$

$$k_{\mathrm{c}} = \frac{2EA}{l_{\mathrm{c}}} \tag{4.37}$$

The configuration of the system is described by five generalized coordinates representing the counterweight, car and counterweight-side and car-side rope mass displacements with respect to the equilibrium position and the sheave rotation angle: u_{w}, u_{c}, u_1, u_2 and $u_{\mathrm{sh}} = \theta r$ respectively.
The natural frequencies and mode shapes result from

$$\mathbf{M\ddot{u}} + \mathbf{Ku} = \mathbf{0} \tag{4.38}$$

i.e., from the eigenvalue problem defined by

$$-\mathbf{Ku} = \mathbf{M}\omega^2\mathbf{u} \tag{4.39}$$

where the inertia $\mathbf{M}$ and stiffness $\mathbf{K}$ matrices and the vector $\mathbf{u}$ are given by Eqns. 4.40, 4.41 and 4.42 respectively.

$$\mathbf{M} = \begin{bmatrix} m_{\mathrm{w}} & 0 & 0 & 0 & 0 \\ 0 & m_1 & 0 & 0 & 0 \\ 0 & 0 & I/r^2 & 0 & 0 \\ 0 & 0 & 0 & m_2 & 0 \\ 0 & 0 & 0 & 0 & m_{\mathrm{c}} \end{bmatrix} \tag{4.40}$$

$$\mathbf{K} = \begin{bmatrix} k_{\mathrm{w}} & -k_{\mathrm{w}} & 0 & 0 & 0 \\ -k_{\mathrm{w}} & 2k_{\mathrm{w}} & k_{\mathrm{w}} & 0 & 0 \\ 0 & k_{\mathrm{w}} & (k_{\mathrm{w}} + k_{\mathrm{c}}) & -k_{\mathrm{c}} & 0 \\ 0 & 0 & -k_{\mathrm{c}} & 2k_{\mathrm{c}} & -k_{\mathrm{c}} \\ 0 & 0 & 0 & -k_{\mathrm{c}} & k_{\mathrm{c}} \end{bmatrix} \tag{4.41}$$

$$\mathbf{u} = [u_{\mathrm{w}} \; u_1 \; u_{\mathrm{sh}} \; u_2 \; u_{\mathrm{c}}]^{\mathrm{T}} \tag{4.42}$$

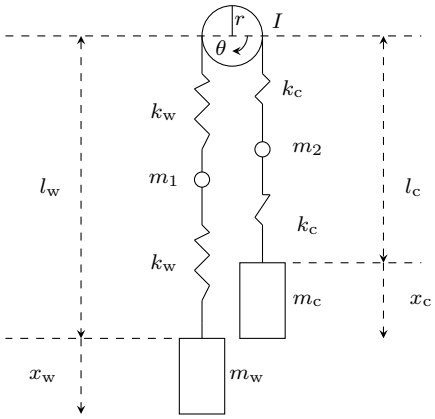

Figure 4.3: 5 DOF model of a 1:1 roping cfg. elevator

4.3 Natural frequencies and mode shapes

The natural frequencies and mode shapes for a particular case will be calculated by the two models developed. The parameter values correspond to a laboratory model that will be described in Chapter 6.

The masses are m_{w} =33 kg and m_{c} =70.5 kg, the whole length and mass density of the rope are 8.6 m and μ = 0.095 kg/m respectively and the moment of inertia and the radius of the traction sheave I = 0.3385 kg·m^2, r = 0.065 m respectively. The product between the elasticity modulus and the cross-section area of the rope EA has been assigned a value of 10^6 N.

In the case of the LPM, the eigenvalue problem defined by Eqn. 4.39 determines the natural frequencies and mode shapes of the system.

In the case of the DPM, the roots of Eqn. 4.26 determine the natural frequencies of the system and the corresponding modes are given by Eqns. 4.24 and 4.25.

Fig. 4.4 shows the five natural frequencies calculated by the five DOF LPM and Fig. 4.5 shows the first six natural frequencies calculated by the DPM. The first natural frequency is 0 Hz and corresponds to an overall transport motion of the system. Figs. 4.6 and 4.7 compare the natural frequencies calculated by both methods. Fig. 4.8 shows the natural frequencies calculated by the DPM and those calculated by an 11 DOF LPM for the same frequency band.

4.4 Conclusions

The first three natural frequencies calculated using the DPM model and the LPM model compare very well (see Fig. 4.7). However, at higher frequencies there are some differences between the results that are obtained from these models. It is demonstrated that if the rope is represented by a larger number of lumped masses so that the number of degrees of freedom in the LPM is increased, this model yields more accurate results with the differences between the frequencies calculated from the DPM and LPM being decreased (see Figs. 4.6 and 4.8).

Regarding the mode shapes, Fig. 4.9 shows the modes corresponding to the 2nd, 3rd, 4th and 5th natural frequencies calculated by both models when the counterweight-side rope length is 2 m. The horizontal axis is the position given by the variable s with respect to the reference frame shown in Fig. 4.2. The car, the counterweight and the sheave are located at the nodes for all higher mode shapes from the 4th onwards.

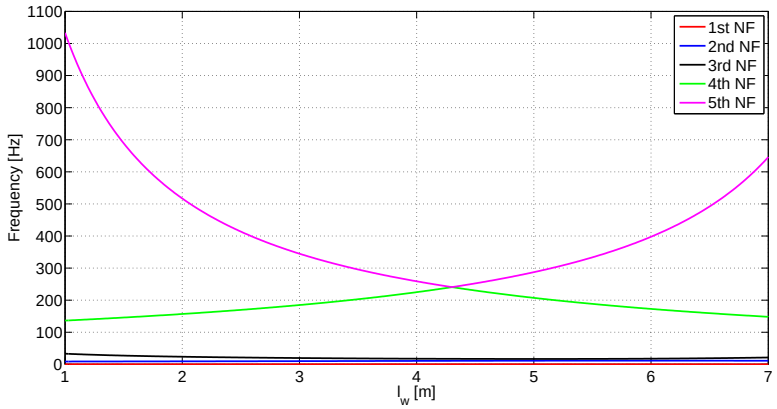

Figure 4.4: The five natural frequencies as a function of the counterweight-side rope length calculated by the LPM

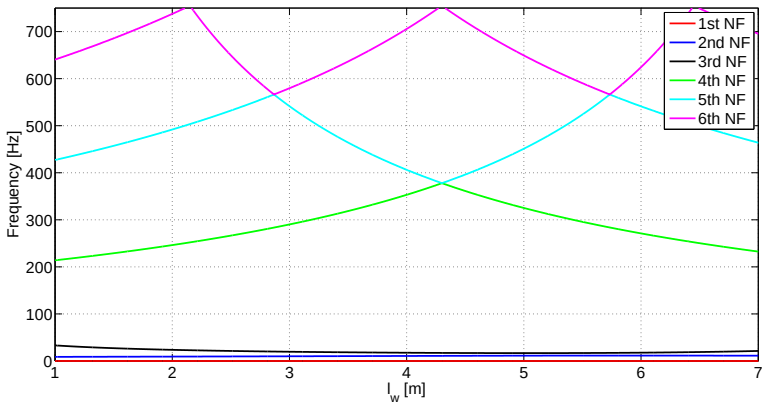

Figure 4.5: The first six natural frequencies as a function of the counterweight-side rope length calculated by the DPM

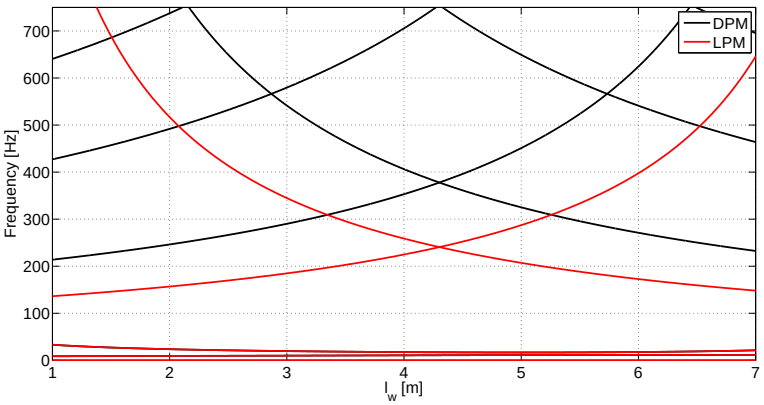

Figure 4.6: Comparison of natural frequencies calculated by both models for those below 750 Hz

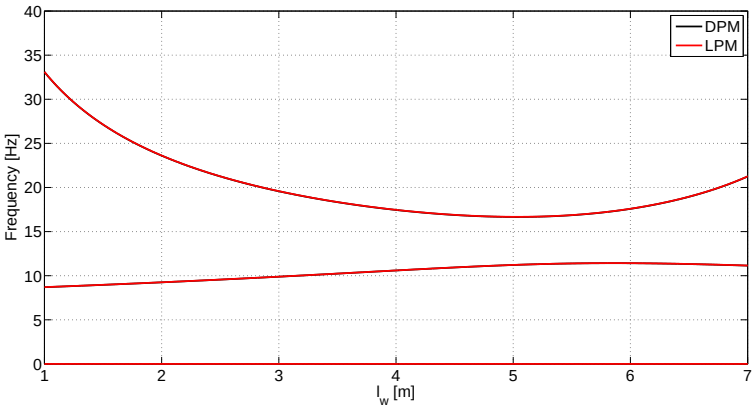

Figure 4.7: Comparison of natural frequencies calculated by both models for those below 40 Hz

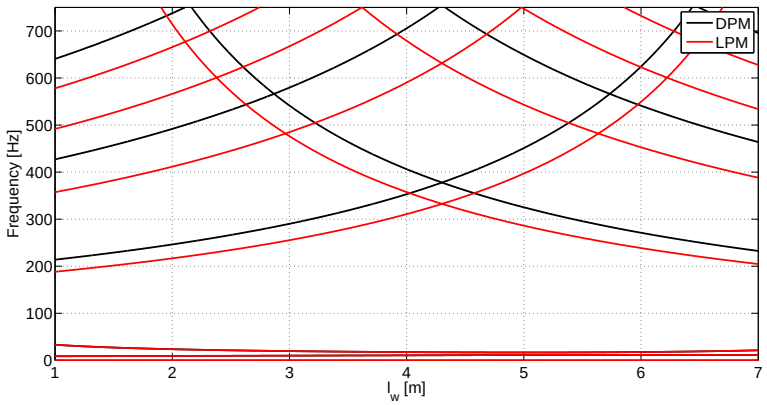

Figure 4.8: Comparison of natural frequencies calculated by both models for those below 750 Hz when the LPM has 11 DOFs

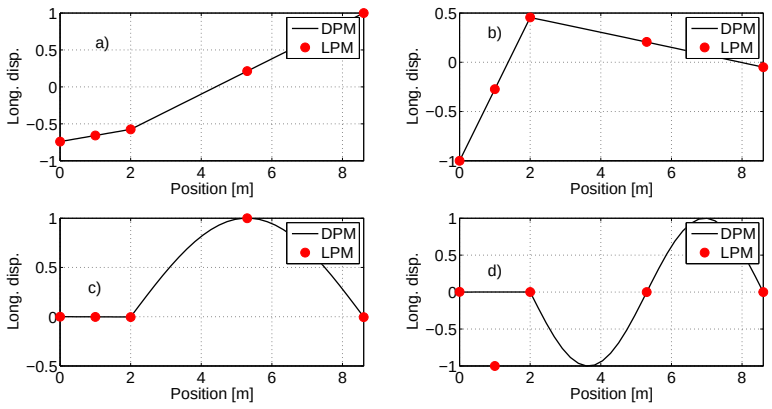

Figure 4.9: Mode shapes corresponding to the a) 2nd, b) 3rd, c) 4th and d) 5th natural frequencies calculated by both models

5

Non-stationary model

It is developed a non-stationary model of the elevator to simulate its acceleration response to excitation generated at the machine.
The model includes the drive system; it comprises a permanent magnet synchronous motor powered via an inverter that supplies a pulse width modulated (PWM) voltage. The well known direct quadrature zero (dqo) mathematical transformation is applied to simplify the analysis of the three-phase synchronous machine. A common vector control strategy oriented to the magnets flux is implemented to control the motor shaft speed in order for the car to follow a prescribed velocity profile to achieve good ride quality. The machine parameters are computed by means of the Finite Element Method simulation software FLUX and the amplitudes of the main frequency components of the torque ripple are estimated.
The car-counterweight-sheave-rope assembly is represented by a non-stationary either distributed- or lumped-parameter model. In the case of the DPM, the PDE equation set is discretised by the Galerkin method; the vertical displacements are expanded in terms of the linear stationary mode shapes of the system composed of three masses constrained by the suspension rope.
It is shown that only two modes contribute to the car and counterweight vibration responses and, as far as the prediction of the response of the car and the counterweight, it can be concluded that a five degree-of-freedom lumped-parameter model is as accurate as the distributed-parameter model.
It is observed that the excitation frequencies originated at the machine close to the elevator system natural frequencies are particularly manifest in the car- and counterweight-

frame acceleration signals and that their amplitude varies according to the proximity between them (resonance phenomena).

5.1 Drive System Model

A model of the drive system is shown in Fig. 5.1. The input to the drive system is a desired velocity profile and the output is the machine torque, that is the input to the mechanical system. The drive system comprises a permanent magnet synchronous motor (PMSM) powered via an inverter that supplies a pulse width modulated (PWM) voltage.

In order to simplify the analysis of the three-phase synchronous machine, a mathematical transformation known as the direct quadrature zero (dqo) transformation (48) is used. In the case of balanced three-phase circuits, application of the dqo transform reduces the three AC quantities to two DC quantities. Simplified calculations can then be carried out on these imaginary DC quantities before performing the inverse transform to recover the actual three-phase AC results. According to the reference frame transformation theory, the three phase variables, currents and voltages, are transformed to the dq reference frame, which consists of the direct (d) axis and the quadrature (q) axis and is rotating at the stator current frequency ω_{s}, representing the fundamental frequency. The fundamental frequency ω_{s} satisfies the following equation,

$$\omega_{\mathrm{s}} = p\omega_{\mathrm{m}} \tag{5.1}$$

where p is the number of pole pairs of the machine stator and ω_{m} the rotation speed of the rotor. In this setup, the dq components of the currents and the voltages are constant.

The motor shaft speed is controlled in order for the car to follow a prescribed velocity profile ω_{m}^{*} to achieve good ride quality. A well known vector control strategy oriented to the magnets flux has been implemented in the computer simulation (60). Such control scheme consists of two control loops: outer and inner loops. In the outer control loop the speed of the motor is regulated by a conventional Proportional Integral (PI) controller, which sets the torque reference τ^{*} with the aim of minimizing the speed error $\omega_{\mathrm{m}}^{*} - \omega_{\mathrm{m}}$. In the inner control loop two PI controllers are implemented in order to regulate the dq axes currents i_{d} and i_{q}. These two controllers set the dq axes voltage references v_{d}^{*} and

v_q^* in order to minimize the current errors. The q axis current reference i_q^* is obtained directly from the torque reference τ^*, because in permanent magnet synchronous motors the relationship between the torque τ and the q axis i_q current is practically constant and known as the torque constant (see Eqn. 5.9). The field weakening strategy is not implemented so that the d axis current reference i_d^* is set to zero (34).

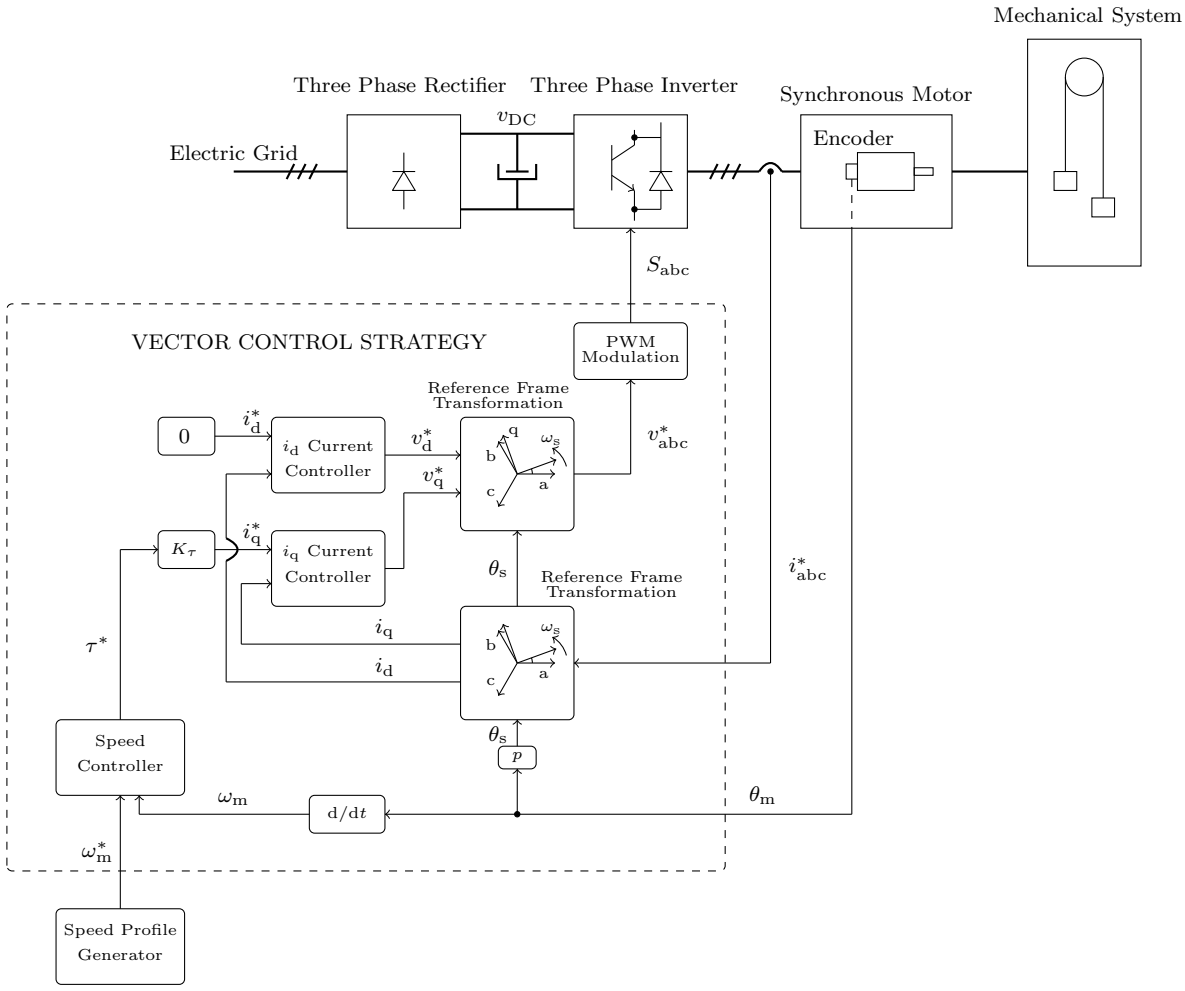

Figure 5.1: The elevator model, with the mechanical and drive systems. The latter includes the control diagram, the power converter and the electric motor

5.1.1 Electric motor model

The machine is a 12 pole permanent magnet synchronous motor comprising a stator with 72 slots. The electric model of the motor is described by the following two differential equations,

$$v_{\mathrm{d}} = R_{\mathrm{s}} i_{\mathrm{d}} + \frac{\mathrm{d}\Psi_{\mathrm{d}}}{\mathrm{d}t} - p\omega_{\mathrm{m}} L_{\mathrm{q}} i_{\mathrm{q}} \tag{5.2}$$

$$v_{\mathrm{q}} = R_{\mathrm{s}} i_{\mathrm{q}} + \frac{\mathrm{d}\Psi_{\mathrm{q}}}{\mathrm{d}t} + p\omega_{\mathrm{m}} \left(L_{\mathrm{d}} i_{\mathrm{d}} + \Psi_{\mathrm{pm}}\right) \tag{5.3}$$

where v_{d} and v_{q}, i_{d} and i_{q} and Ψ_{d} and Ψ_{q} are the dq axes voltages, currents and flux linkages respectively, Ψ_{pm} is the magnet flux linkage, R_{s} is the stator resistance, L_{d} and L_{q} are the dq axes inductances and ω_{m} is the mechanical speed. The dq axes flux linkages are defined as (60),

$$\Psi_{\mathrm{d}} = L_{\mathrm{d}} i_{\mathrm{d}} + \Psi_{\mathrm{pm}} \tag{5.4}$$

$$\Psi_{\mathrm{q}} = L_{\mathrm{q}} i_{\mathrm{q}} \tag{5.5}$$

Consequently, as Ψ_{pm} is constant,

$$v_{\mathrm{d}} = R_{\mathrm{s}} i_{\mathrm{d}} + L_{\mathrm{d}} \frac{\mathrm{d}i_{\mathrm{d}}}{\mathrm{d}t} - p w_{\mathrm{m}} L_{\mathrm{q}} i_{\mathrm{q}} \tag{5.6}$$

$$v_{\mathrm{q}} = R_{\mathrm{s}} i_{\mathrm{q}} + L_{\mathrm{q}} \frac{\mathrm{d}i_{\mathrm{q}}}{\mathrm{d}t} + p w_{\mathrm{m}} \left(L_{\mathrm{d}} i_{\mathrm{d}} + \Psi_{\mathrm{pm}}\right) \tag{5.7}$$

The torque τ generated by a motor is composed of two components: the average torque τ_{avg} and the torque ripple τ_{r}. In addition, the torque ripple is composed of another two components: the electromagnetic torque ripple and the cogging torque. The electromagnetic torque ripple is mainly due to the spatial distribution of stator windings and the magnets shape, while the cogging torque depends mainly on the number of stator slots and pole pairs (72). The average value of the torque produced by the motor can be modelled as follows

$$\tau_{\mathrm{avg}} = \frac{3}{2} p \left(\Psi_{\mathrm{d}} i_{\mathrm{q}} - \Psi_{\mathrm{q}} i_{\mathrm{d}}\right) \tag{5.8}$$

The d axis current i_{d} is set to 0,

$$\tau_{\mathrm{avg}} = \frac{3}{2} p \Psi_{\mathrm{pm}} i_{\mathrm{q}} \tag{5.9}$$

Eqn. 5.9 shows that the average torque generated by the motor τ_{avg} is proportional to the q axis current i_{q}. The magnitude of the electromagnetic torque ripple τ_{r} is also proportional to the q axis current i_{q} as it is demonstrated in (4). Nevertheless, the magnitude of the cogging torque does not depend on the current magnitude and is constant, even when the motor is not power supplied. Then, the overall torque τ is computed as follows

$$\tau = \tau_{\mathrm{avg}} + \tau_{\mathrm{r}} = \frac{3}{2} p \Psi_{\mathrm{pm}} i_{\mathrm{q}} + K_j i_{\mathrm{q}} \sin(k \omega_{\mathrm{s}} t) + K_{\mathrm{cg}} \sin(n \omega_{\mathrm{s}} t) \tag{5.10}$$

where K_j is the torque constant for the main component of the electromagnetic torque ripple, whose order is j, and K_{cg} is the magnitude of the main cogging torque component, whose order is n. In Fig. 5.2 the overall block diagram of the modelled motor is shown, where it is satisfied that $\omega_{\mathrm{m}} = \dot{\theta}_{\mathrm{m}}$ and $\omega_{\mathrm{s}} = \dot{\theta}_{\mathrm{s}}$.

5.2 Vertical vibration model

Two possibilities to model the car-counterweight-sheave-rope assembly will be implemented: a DPM and a LPM.

5.2.1 Distributed-parameter model

The non-stationary DPM to be developed is based on the DPM described in Section 4.1.

In order to describe the oscillations of the rope, the classical moving frame approach is applied (27) (see Figs. 4.1 and 5.3). Two frames of reference are defined: a coordinate system $\Omega\xi$ attached to the undeformed body at the counterweight and moving with it, and a stationary inertial system Ox. The dynamic deformed position of an arbitrary section of the rope during its motion is defined in the inertial frame by the position vector

$$\mathbf{R}(s,t) = \mathbf{R}_{\Omega}(s,t) + \mathbf{R}^{i}(s,t) + \mathbf{U}(s,t) \tag{5.11}$$

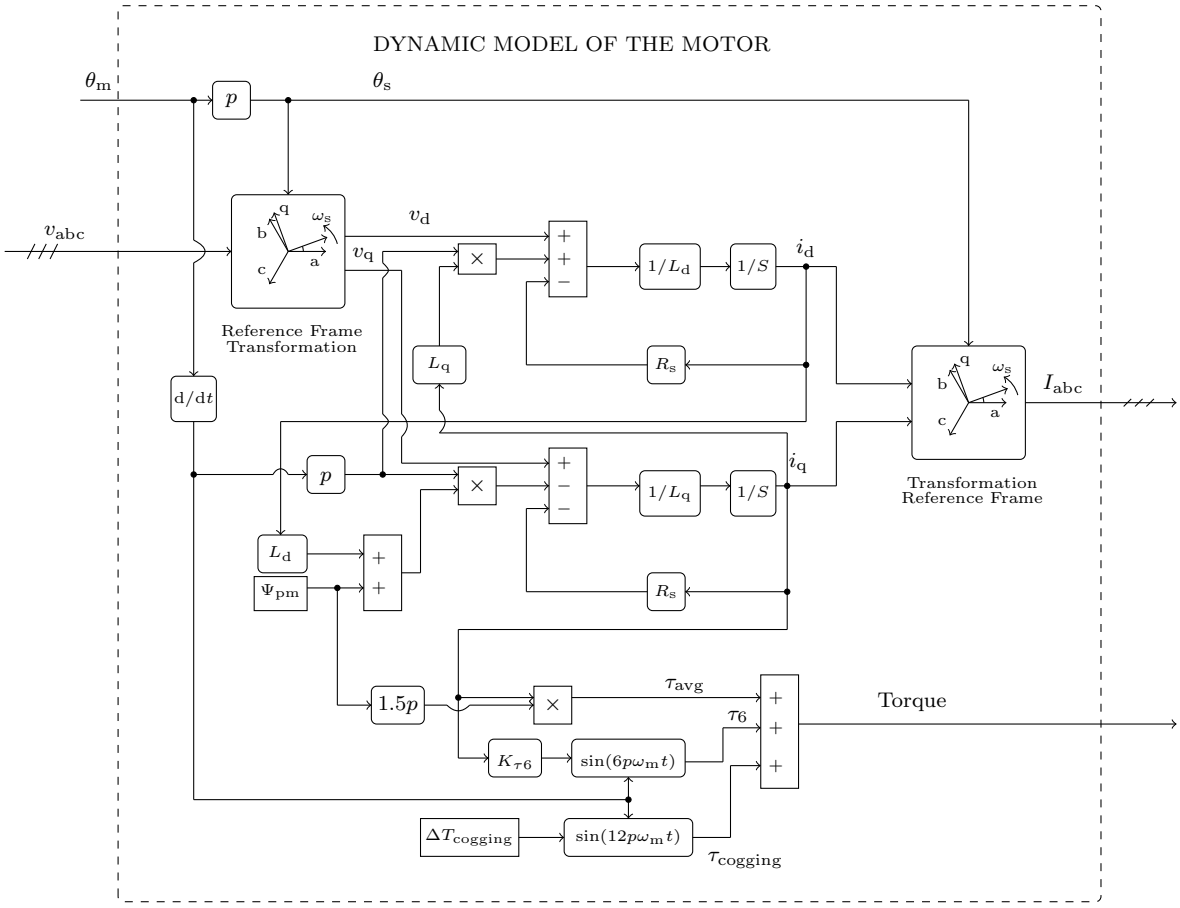

Figure 5.2: Synchronous Motor Model

where s denotes the Lagrangian (material) coordinate of P^i, representing the dynamically undeformed position of the rope section, and measured from the counterweight frame. In this representation the axial transport motion is treated as essentially an overall rigid-body translation, and the dynamic elastic deformations are referred to the moving frame associated with this motion. All dynamic characteristics of the rope are functions of the independent variables (s,t), with s being referred to the unstressed state and the moving frame. Thus, $\mathbf{R}_\Omega = -l\mathbf{i}$ represents the position of the origin Ω in the inertial frame ($\mathbf{i}$ is the unit vector in the positive x direction), $\mathbf{R}^i = s\mathbf{i}$ defines the reference position P^i in the moving frame , and $\mathbf{U} = u(s,t)\mathbf{i}$ is the dynamic deformation vector with u representing the longitudinal motion of the rope.

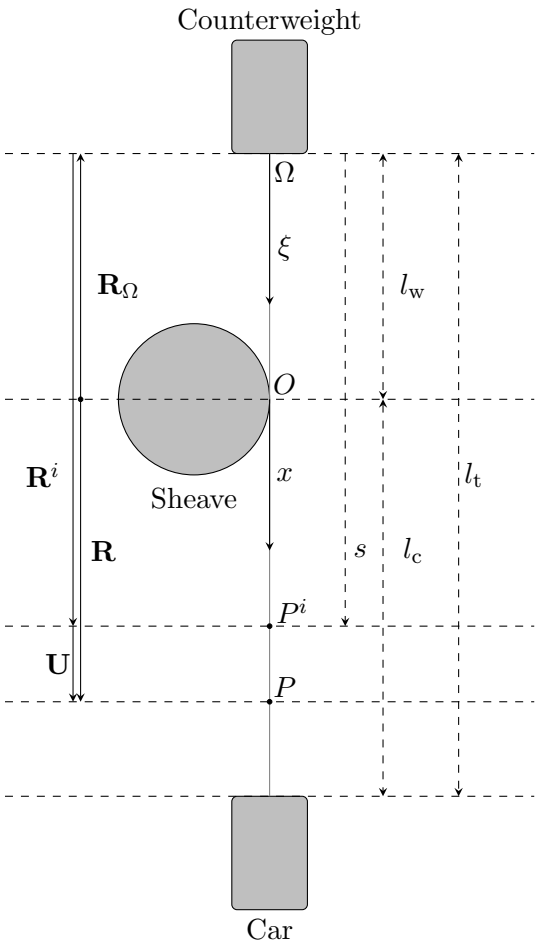

Figure 5.3: Reference frames

The longitudinal dynamic deflection in the car-side rope will be denoted as $u_\mathrm{c}(s,t)$, and the one in the counterweight-side rope as $u_\mathrm{w}(s,t)$. Thus, the deformed position vector is defined as

$$\mathbf{R} = \begin{cases} (s + u_\mathrm{w}(s,t) - l_\mathrm{w})\,\mathbf{i}, & 0 \le s \le l_\mathrm{w} \\ (s + u_\mathrm{c}(s,t) - l_\mathrm{w})\,\mathbf{i}, & l_\mathrm{w} \le s \le l_\mathrm{t} \end{cases} \tag{5.12}$$

The continuity of deflection across the sheave requires $u_\mathrm{w}(l_\mathrm{w},t) = u_\mathrm{c}(l_\mathrm{w},t)$. The velocity vector of a rope particle P is determined by

$$\dot{\mathbf{R}} = \begin{cases} \mathbf{v}_\mathrm{w} = \left(u_{\mathrm{w},t}(s,t) - \dot{l}_\mathrm{w}\right)\mathbf{i}, & 0 \le s \le l_\mathrm{w} \\ \mathbf{v}_\mathrm{c} = \left(u_{\mathrm{c},t}(s,t) - \dot{l}_\mathrm{w}\right)\mathbf{i}, & l_\mathrm{w} \le s \le l_\mathrm{t} \end{cases} \tag{5.13}$$

5.2.1.1 Equations of Motion

Hamilton's principle (38) yields the following equations and boundary conditions for the dynamic deflections (see Appendix A).

$$EAu_{\mathrm{w},ss} - \mu g = \mu \left(u_{\mathrm{w},tt} - \ddot{l}_{\mathrm{w}} \right) \tag{5.14}$$

$$EAu_{\mathrm{c},ss} + \mu g = \mu \left(u_{\mathrm{c},tt} - \ddot{l}_{\mathrm{w}} \right) \tag{5.15}$$

$$EAu_{\mathrm{w},s}(0,t) - m_{\mathrm{w}} g = m_{\mathrm{w}} \left(u_{\mathrm{w},tt}(0,t) - \ddot{l}_{\mathrm{w}} \right) \tag{5.16}$$

$$-EAu_{\mathrm{c},s}(l_{\mathrm{t}},t) + m_{\mathrm{c}} g = m_{\mathrm{c}} \left(u_{\mathrm{c},tt}(l_{\mathrm{t}},t) - \ddot{l}_{\mathrm{w}} \right) \tag{5.17}$$

$$\frac{\tau}{r} + EA\left[u_{\mathrm{c},s}\left(l_{\mathrm{w}},t\right) - u_{\mathrm{w},s}\left(l_{\mathrm{w}},t\right)\right] = m_{\mathrm{sh}} \left(u_{\mathrm{w},tt}(l_{\mathrm{w}},t) - \ddot{l}_{\mathrm{w}} \right) \tag{5.18}$$

The rope dynamic displacements of the ropes are defined as

$$u\left(s,t\right) = \begin{cases} u_{\mathrm{w}}\left(s,t\right) = u_{\mathrm{w}}^{\mathrm{e}}\left(s\right) + u_{\mathrm{w}}^{\mathrm{d}}\left(s,t\right), \ 0 \le s \le l_{\mathrm{w}} \\ u_{\mathrm{c}}\left(s,t\right) = u_{\mathrm{c}}^{\mathrm{e}}\left(s\right) + u_{\mathrm{c}}^{\mathrm{d}}\left(s,t\right), \ l_{\mathrm{w}} \le s \le l_{\mathrm{t}} \end{cases} \tag{5.19}$$

where $u_{\mathrm{w}}^{\mathrm{e}}\left(s\right)$ and $u_{\mathrm{c}}^{\mathrm{e}}\left(s\right)$ express the static deflection at equilibrium of the rope sections at the counterweight- and car-rope sides respectively and satisfy the set of PDEs qiven as

$$EAu_{\mathrm{w},ss}^{\mathrm{e}} - \mu g = 0 \tag{5.20}$$

$$EAu_{\mathrm{c},ss}^{\mathrm{e}} + \mu g = 0 \tag{5.21}$$

$$EAu_{\mathrm{w},s}^{\mathrm{e}}(0) - m_{\mathrm{w}} g = 0 \tag{5.22}$$

$$-EAu_{\mathrm{c},s}^{\mathrm{e}}(l_{\mathrm{t}}) + m_{\mathrm{c}} g = 0 \tag{5.23}$$

$$\frac{\tau^{\mathrm{e}}}{r} + EA\left[u_{\mathrm{c},s}^{\mathrm{e}}\left(l_{\mathrm{w}}\right) - u_{\mathrm{w},s}^{\mathrm{e}}\left(l_{\mathrm{w}}\right)\right] = 0 \tag{5.24}$$

where τ^{e} is the torque applied at the equilibrium position. The solution of Eqns. (5.20)-(5.24) is given as

$$u_{\mathrm{w}}^{\mathrm{e}}\left(s\right) = \frac{g}{EA}\left(\mu\frac{s^2}{2} + m_{\mathrm{w}} s\right) \tag{5.25}$$

$$u_{\mathrm{c}}^{\mathrm{e}}\left(s\right) = \\ = \frac{g}{EA}\left[\left(\mu l_{\mathrm{t}} + m_c\right) s - \frac{\mu s^2}{2} + l_{\mathrm{w}}\left(m_w - m_c - \mu l_{\mathrm{c}}\right)\right] \tag{5.26}$$

The deflections with respect to the equilibrium position $u_{\mathrm{w}}^{\mathrm{d}}(d,t)$ satisfy the following set of PDEs

$$EAu_{\mathrm{w},ss}^{\mathrm{d}} = \mu\left(u_{\mathrm{w},tt} - \ddot{l}_{\mathrm{w}}\right) \tag{5.27}$$

$$EAu_{\mathrm{c},ss}^{\mathrm{d}} = \mu\left(u_{\mathrm{c},tt} - \ddot{l}_{\mathrm{w}}\right) \tag{5.28}$$

$$EAu_{\mathrm{w},s}^{\mathrm{d}}(0,t) = m_{\mathrm{w}}\left(u_{\mathrm{w},tt}(0,t) - \ddot{l}_{\mathrm{w}}\right) \tag{5.29}$$

$$-EAu_{\mathrm{c},s}^{\mathrm{d}}(l_{\mathrm{t}},t) = m_{\mathrm{c}}\left(u_{\mathrm{c},tt}(l_{\mathrm{t}},t) - \ddot{l}_{\mathrm{w}}\right) \tag{5.30}$$

$$\frac{\tau^{\mathrm{d}}}{r} + EA\left[u_{\mathrm{c},s}^{\mathrm{d}}(l_{\mathrm{w}},t) - u_{\mathrm{w},s}^{\mathrm{d}}(l_{\mathrm{w}},t)\right] = m_{\mathrm{sh}}\left(u_{\mathrm{w},tt}(l_{\mathrm{w}},t) - \ddot{l}_{\mathrm{w}}\right) \tag{5.31}$$

The torque τ in Eqn. 5.18 satisfies that

$$\tau = \tau^{\mathrm{e}} + \tau^{\mathrm{d}} \tag{5.32}$$

Eqns. 5.27-5.31 will be discretised by expanding the longitudinal displacements with respect to the equilibrium position in terms of linear stationary mode shapes (Eqn. 5.33)

$$u^{\mathrm{d}}(s,t) = \sum_{i=1}^{n} q_i(t)\Phi_i(s,l_{\mathrm{w}}) \tag{5.33}$$

where $\Phi_i(s,l_{\mathrm{w}})$ represents the mode shapes corresponding to the system described in Section 4.1 and shown in Fig. 4.2. The first n linear stationary natural frequencies are considered in Eqn. 5.33.

5.2.1.2 Mathematical Discrete Model

The series given by Eqn. 5.33 and its derivatives are substituted in Eqns. 5.14-5.18. Next, the Galerkin method with the approximate solution given by Eqn. 5.33 is applied, where the orthogonality conditions of the modes given by Eqn. 4.8 and described in section 4.1.2 are used. As a result, the following set of ODEs with time dependant coefficients is obtained

$$\ddot{\mathbf{q}} + 2\mathbf{Z}\boldsymbol{\Omega}\dot{\mathbf{q}} + \boldsymbol{\Omega}^2\mathbf{q} = \mathbf{M}_1^{-1}$$
$$\Big[\frac{\tau^{\mathrm{d}}}{r}\boldsymbol{\Phi}(l_{\mathrm{w}}) - \mathbf{p}_1 + \ddot{l}_{\mathrm{w}}\left(\mathbf{p}_2 + m_{\mathrm{sh}}\boldsymbol{\Phi}(l_{\mathrm{w}}) - \mathbf{M}_2\mathbf{q}\right) -$$
$$2\dot{l}_{\mathrm{w}}\mathbf{M}_2\dot{\mathbf{q}} - \dot{l}_{\mathrm{w}}^2\mathbf{M}_3\mathbf{q} - c_{\mathrm{sh}}(\mathbf{M}_4\dot{\mathbf{q}} + \mathbf{M}_5\mathbf{q}\dot{l}_{\mathrm{w}} - \dot{l}_{\mathrm{w}}\boldsymbol{\Phi}(l_{\mathrm{w}}))-$$
$$\frac{g}{EA}(2\mu\dot{l}_{\mathrm{w}}^2 + \ddot{l}_{\mathrm{w}}(2\mu l_{\mathrm{w}} + m_{\mathrm{w}} - m_{\mathrm{c}} - \mu l_{\mathrm{t}}))\Big] \tag{5.34}$$

where the $n\times n$ matrices $\boldsymbol{\Omega}, \mathbf{Z}, \mathbf{M}_1, \mathbf{M}_2, \mathbf{M}_3, \mathbf{M}_4, \mathbf{M}_5$ and the $n\times 1$ vectors $\mathbf{q}(t), \mathbf{p}_1, \mathbf{p}_2, \boldsymbol{\Phi}(s)$ are given by the Eqns. 5.35-5.45.

$$(\boldsymbol{\Omega})_{ij} = \delta_{ij}\omega_i;\ \delta_{ij} = 1 \text{ if } i = j, 0 \text{ if } i \neq j \tag{5.35}$$
$$(\mathbf{Z})_{ij} = \delta_{ij}\zeta_i \tag{5.36}$$
$$(\mathbf{M}_1)_{ij} = \delta_{ij}\left(\mu\int_0^{l_{\mathrm{t}}}\Phi_i^2\,\mathrm{d}s + m_{\mathrm{w}}\Phi_i^2(0) + m_{\mathrm{sh}}\Phi_i^2(l_{\mathrm{w}}) + m_{\mathrm{c}}\Phi_i^2(l_{\mathrm{t}})\right) \tag{5.37}$$
$$(\mathbf{M}_2)_{ij} = \mu\int_0^{l_{\mathrm{t}}}\Phi_i\frac{\partial\Phi_j}{\partial l_{\mathrm{w}}}\,\mathrm{d}s +$$
$$+m_{\mathrm{w}}\Phi_i(0)\frac{\partial\Phi_j}{\partial l_{\mathrm{w}}}(0) + m_{\mathrm{sh}}\Phi_i(l_{\mathrm{w}})\frac{\partial\Phi_j}{\partial l_{\mathrm{w}}}(l_{\mathrm{w}}) + m_{\mathrm{c}}\Phi_i(l_{\mathrm{t}})\frac{\partial\Phi_j}{\partial l_{\mathrm{w}}}(l_{\mathrm{t}}) \tag{5.38}$$
$$(\mathbf{M}_3)_{ij} = \mu\int_0^{l_{\mathrm{t}}}\Phi_i\frac{\partial^2\Phi_j}{\partial l_{\mathrm{w}}^2}\,\mathrm{d}s +$$
$$+m_{\mathrm{w}}\Phi_i(0)\frac{\partial^2\Phi_j}{\partial l_{\mathrm{w}}^2}(0) + m_{\mathrm{sh}}\Phi_i(l)\frac{\partial^2\Phi_j}{\partial l_{\mathrm{w}}^2}(l_{\mathrm{w}}) + m_{\mathrm{c}}\Phi_i(l_{\mathrm{t}})\frac{\partial^2\Phi_j}{\partial l_{\mathrm{w}}^2}(l_{\mathrm{t}}) \tag{5.39}$$
$$(\mathbf{M}_4)_{ij} = \Phi_i(l_{\mathrm{w}})\Phi_j(l_{\mathrm{w}}) \tag{5.40}$$
$$(\mathbf{M}_5)_{ij} = \Phi_i(l_{\mathrm{w}})\frac{\partial\Phi_j}{\partial l_{\mathrm{w}}} \tag{5.41}$$
$$(\mathbf{q}(t))_i = q_i(t) \tag{5.42}$$
$$(\mathbf{p}_1)_i = \frac{g}{EA}\left(2\mu\dot{l}_{\mathrm{w}}^2 + \ddot{l}_{\mathrm{w}}(2\mu l_{\mathrm{w}} + m_{\mathrm{w}} - m_{\mathrm{c}} - \mu l_{\mathrm{t}})\right)$$
$$\left(\mu\int_{l_{\mathrm{w}}}^{l_{\mathrm{t}}}\Phi_i\,\mathrm{d}s + m_{\mathrm{c}}\Phi_i(l_{\mathrm{t}})\right) \tag{5.43}$$
$$(\mathbf{p}_2)_i = \mu\int_0^{l_{\mathrm{t}}}\Phi_i\,\mathrm{d}s + m_{\mathrm{w}}\Phi_i(0) + m_{\mathrm{c}}\Phi_i(l_{\mathrm{t}}) \tag{5.44}$$
$$(\boldsymbol{\Phi}(s))_i = \Phi_i(s) \tag{5.45}$$

Eqn. 5.34 is a nonlinear time-varying ODE set. There are couplings among the coordinates due to the products $\ddot{l}_{\mathrm{w}}\ \mathbf{q}, \dot{l}_{\mathrm{w}}\,\dot{\mathbf{q}}, \dot{l}_{\mathrm{w}}^2\,\mathbf{q}$ and terms representing the inertial load

due to the axial transport motion are present. The modal damping included in Eqn. 5.36 accommodates damping effects at the rail-guide contact and the coefficient c_{sh} in Eqns. 5.34 accounts for not only viscous friction but also any other energy losses in the machine.

5.2.2 Lumped-parameter model

This model is based in the 5 DOF lumped-parameter stationary model developed in Section 4.2.

The spring stiffness constants in Eqns. 4.36-4.37 are updated every time instant during the elevator travel. The sheave rotation angle is related to the length of the counterweight-side rope by

$$r\frac{\mathrm{d}\theta}{\mathrm{d}t} = -\frac{\mathrm{d}l_{\mathrm{w}}}{\mathrm{d}t} \tag{5.46}$$

The torque provided by the machine in Fig. 5.1 is composed of two terms; the first one accommodates the torque corresponding to the outbalance weight given by Eqn. 5.47

$$\tau^{\mathrm{e}} = (m_{\mathrm{w}} - m_{\mathrm{c}} + \mu(2l_{\mathrm{w}} - l_{\mathrm{t}}))gr \tag{5.47}$$

and the second one τ^{d} is included in the vector $\mathbf{\Delta F}$ given by Eqn. 5.48

$$\mathbf{\Delta F} = \begin{bmatrix} 0 & 0 & \dfrac{\tau^{\mathrm{d}}}{r} & 0 & 0 \end{bmatrix}^{\mathrm{T}} \tag{5.48}$$

that relates to the rest of variables by Eqn. 5.49

$$\mathbf{M\ddot{u} + C\dot{u} + Ku} = \mathbf{\Delta F} \tag{5.49}$$

where the inertia $\mathbf{M}$, stiffness $\mathbf{K}$ and damping $\mathbf{C}$ matrices and the vector $\mathbf{u}$ are given by Eqns. 4.40, 4.41, 5.50 and 4.42 respectively.

$$\mathbf{C} = \begin{bmatrix} c_{\mathrm{w}} & 0 & 0 & 0 & 0 \\ 0 & 0 & 0 & 0 & 0 \\ 0 & 0 & c_{\mathrm{sh}} & 0 & 0 \\ 0 & 0 & 0 & 0 & 0 \\ 0 & 0 & 0 & 0 & c_{\mathrm{c}} \end{bmatrix} \tag{5.50}$$

The damping matrix accounts for the friction at the guide-rail contact and at the sheave.

5.3 Simulation

The acceleration responses of the main components during an elevator travel will be simulated by means of the models developed in Section 5.2.
The values of all the parameters correspond to the laboratory model that will be described in Chapter 6. They correspond as well to the case described in Section 4.3. The experimental tests that have been carried out in order to estimate some of these values will be described as well in Chapter 6.
The masses are m_{w} =33 kg and m_{c} =70.5 kg. The length l_{t}, the mass density μ and the elasticity modulus cross-sectional area product EA of the rope are 8.6 m, 0.095 kg/m and 10^6 N respectively. The moment of inertia and the radius of the traction sheave are $I = 0.3385$ kg·m^2 and $r = 0.065$ m respectively.

5.3.1 Computation of the motor parameters by FEA

The electric motor model (described in Section 5.1.1) uses some characteristic parameters such as inductances, resistance, magnet flux linkage and torque constants. All those parameters of the motor have been computed by Finite Element Analysis (FEA) by means of the software FLUX. In Fig. 5.4 the simulated motor geometry along with the mesh distribution are shown.

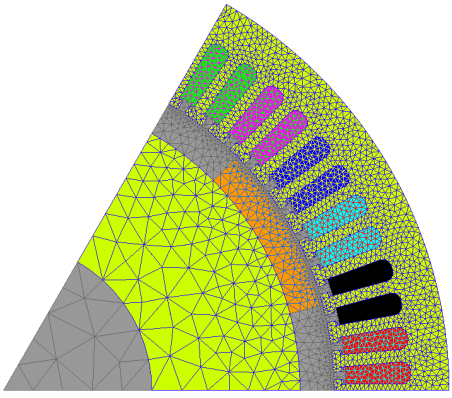

Figure 5.4: Mesh distribution

As the motor consist of p=6 pole pairs, the simulation geometry can be simplified to one pole pair domain. In Fig. 5.5 the magnetic field induced by the magnets around the geometry of the motor is shown.

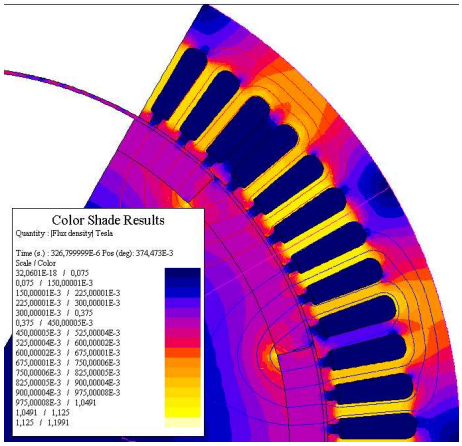

Figure 5.5: Spatial distribution of the magnetic field induced by the magnets

Table 5.1 summarises the main motor parameters computed by FEA simulations.

Coil Resistance	R_{s}	0.33 Ω
d-axis Inductance	L_{d}	8.5 mH
q-axis Inductance	L_{q}	11.7 mH
Magnet Flux Linkage	$\Psi_{\mathrm{pm}}(\mathrm{rms})$	0.83 Wb
Average Torque Constant	K_{τ}	10.44 Nm/A
Torque Ripple Constant	K_k	0.1354 Nm/A
Cogging Torque Magnitude	K_{cg}	1.25 Nm

Table 5.1: Parameters computed by FEA simulations

In addition to the components of the torque ripple described, radial forces are generated at the air gap between the stator and the rotor of the machine (17), that cause vibration of the stator core and yoke. The radial magnetic force per unit area or magnetic pressure waveform at any point of the air gap is obtained bay means of the Maxwell's stress tensor theorem given by Eqn. 5.51

$$P_{\mathrm{rd}}(\theta,t) = \frac{1}{2\mu_0}\left(B_{\mathrm{n}}^2(\theta,t) - B_{\mathrm{tg}}^2(\theta,t)\right) \tag{5.51}$$

where θ is the rotation angle with respect to the axis of symmetry of the machine, μ_0 is the magnetic permeability, t is the time, and B_{n} and B_{tg} the normal and the tangential components of magnetic field around the air-gap.

The force is decomposed in Fourier series, so that the inner surface of the stator is subjected to several sinusoidally distributed loads. The main components in the series contribute to the torque ripple too, specially when the spatial order and frequency of the excitation force are close to the stator mode shape and corresponding natural frequency respectively.

Fig. 5.6 shows the waveform of the magnetic radial pressure at a certain point of the stator core as a function of the rotor position. The spatial period of this signal is $\pi/6$ for symmetry reasons.

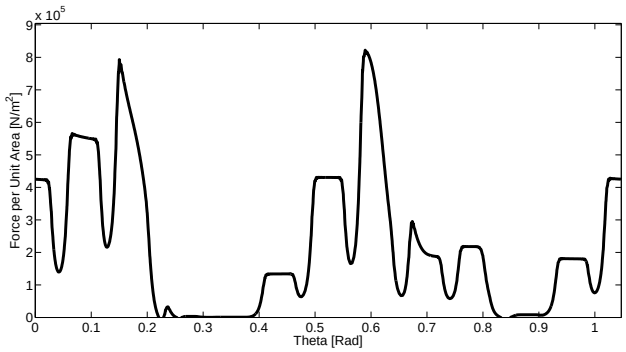

Figure 5.6: Magnetic radial force per unit area at rated load condition

Fig. 5.7 shows the components (spatial orders) in the corresponding Fourier series. The highest component corresponds to the spatial order 0 and it is a constant pressure; the spatial order 2 is a sinusoidal pressure distribution of spatial period $\pi/6$ and corresponding excitation frequency twice the fundamental one, $2\omega_s$, and it is the main harmonic of the radial force.

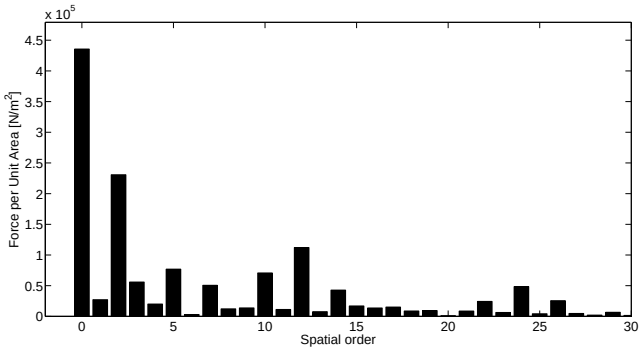

Figure 5.7: Fourier series components

5.3.2 Damping coefficients

Viscous friction and any other possible energy loss at the machine have been lumped in the parameter c_{sh} in Eqns. 5.34 and 5.50; the value assigned to it is 3 kg/s, estimated from some experimental tests that will be described in Chapter 6.

Damping at the guide-rail contact has been accommodated in the parameter ζ_i in Eqn. 5.36. The value assigned to it is 0.036 and has been estimated from experimental tests described in Chapter 6. It is calculated by (12)

$$\zeta = \frac{1}{2\pi} \ln \frac{x(t)}{x(t+T)} \tag{5.52}$$

applied to the exponential decrease in the vibration amplitude that occurs after a sharp and sudden stop of the car-frame in the laboratory setup. In Eqn. 5.52, $x(t)$ is the acceleration signal and T its period. The same value of ζ has been assumed for all modes. The values of c_{w} and c_{c} in Eqn. 5.50 are assumed to be equal and calculated by (12)

$$c_{\mathrm{w}} = c_{\mathrm{c}} = 2\zeta\omega m_{\mathrm{w}} \tag{5.53}$$

where ω is the circular frequency corresponding to the period T. The value obtained is around 148 kg/s.

5.3.3 System response

The particular reference velocity profile to be followed by the car-frame is given by Fig. 5.8.

The main electromagnetic torque ripple and the cogging torque frequency values are respectively 6 and 12 times the fundamental frequency ω_{s}, that is around 6 Hz at the setup rated speed (see Fig. 5.8). Those frequencies are 36 Hz and 72 Hz respectively. Furthermore, the 2nd order component of the radial force is around 12 Hz.

A particular torque ripple (see Chapter 6) has been added as a perturbation to the controller generated torque. Fig. 5.9 shows the average power spectral density of the torque ripple during the constant velocity stage. The frequency components corresponding to the main electromagnetic torque ripple, the cogging and the main component of the radial force, 36, 72 and 12 Hz respectively, are apparent, but there are also components at 1 Hz and 6 Hz (the electric frequency) and some of its harmonics (18 Hz, 24 Hz).

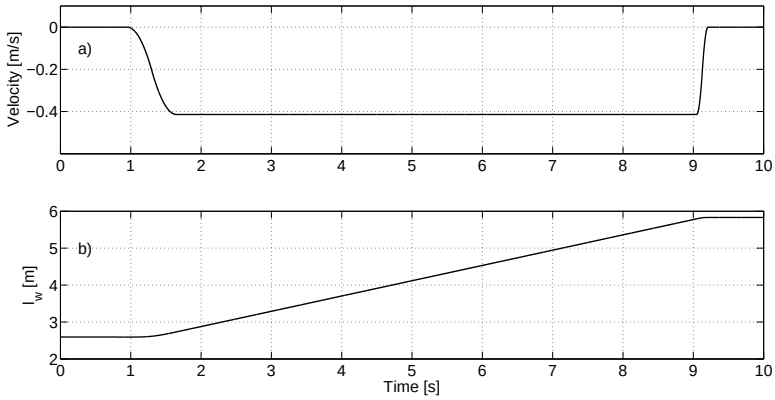

Figure 5.8: Reference a) velocity and b) counterweight-side rope length

The simulation model is implemented in the MATLAB/Simulink computational environment. The travel has been simulated by the two models developed. In the case of the DPM, the set of Eqns. 5.34 has been solved. Two cases have been considered: in the first one, the first two terms have been considered in Eqn. 5.33 during the discretisation process of the PDE set Eqns. 5.14-5.18; in the second one, the first five terms that, for this particular case, involves considering all natural frequencies below 750 Hz. Figs. 5.10 and 5.11 show the counterweight and car accelerations respectively, obtained by simulating the LPM and the DPM with two and five terms.

It can be observed that both models provide almost the same accelerations. It is because the counterweight, the car and the sheave are located at nodes in all mode shapes from the 4th onwards. Bearing in mind that for the higher modes (from the fourth mode upwards) the locations of the car, traction sheave and counterweight elements correspond to nodes, and considering that the first mode represents the overall motion of the system, it can be concluded that only the second mode and the third mode contribute to the acceleration responses of these elements. Therefore, the 5 DOF LPM model is a good approximation to predict the counterweight, car and sheave response.

The spectrogram of the simulated counterweight and car accelerations are shown in Figs. 5.12 and 5.13. The spectrograms, in dB/Hz (dB relative to the reference value of 1 m/s^2), have been calculated by the Burg algorithm (50). The frequency band shown is the interval 0-128 Hz. The natural frequencies of the system in that band have been traced as well.

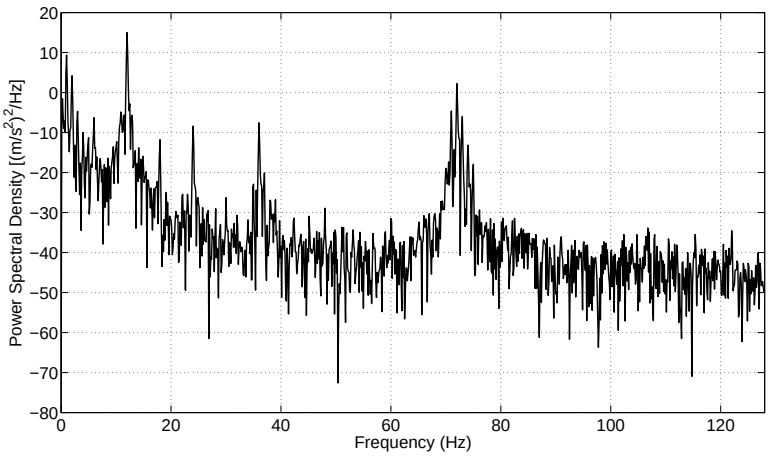

Figure 5.9: Torque ripple average power spectral density in the constant velocity stage

The excitation frequencies present in Fig. 5.9 appear in the spectrograms shown in Figs. 5.12 and 5.13. The vibration amplitude at the excitation frequency of 12 Hz is particularly high because it is the main component in the torque ripple (see Fig. 5.9) but also due to its proximity to the second natural frequency of the system.
During the constant velocity stage, Fig. 5.10 shows that the amplitude of vibration increases progressively until t =8 s. Figs. 5.12 and 5.13 show that the 2nd and 3rd natural frequencies approach are the closest to the excitation frequency of 12 Hz around that instant, which can be the reason of the progressive increase.

5.4 Conclusions

A comprehensive mathematical model has been developed in order to simulate the response of the system. It includes the drive system, with the machine and its controllers, whose parameters have been calculated by the electromagnetic FEM software FLUX. The acceleration response of the system during a travel has been simulated. A particular torque ripple has been added to the controller generated one.
Regarding the car-counterweight-sheave-ropes assembly, a novel distributed-parameter model is developed, but it is shown that only two modes contribute to the car and counterweight responses and that a five degree-of-freedom lumped-parameter model is as accurate as the distributed-parameter one.

It is observed that the excitation frequencies originated at the machine close to the elevator system natural frequencies are particularly manifest in the car- and counterweight-frame acceleration signals and that their amplitude varies according to the proximity between them (resonance phenomena).

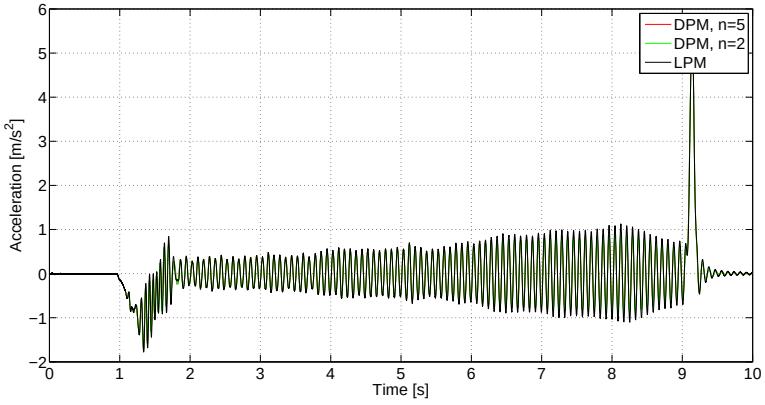

Figure 5.10: Simulated counterweight acceleration by the DPM with 2 terms (green), the DPM with 5 terms (red) and the LPM

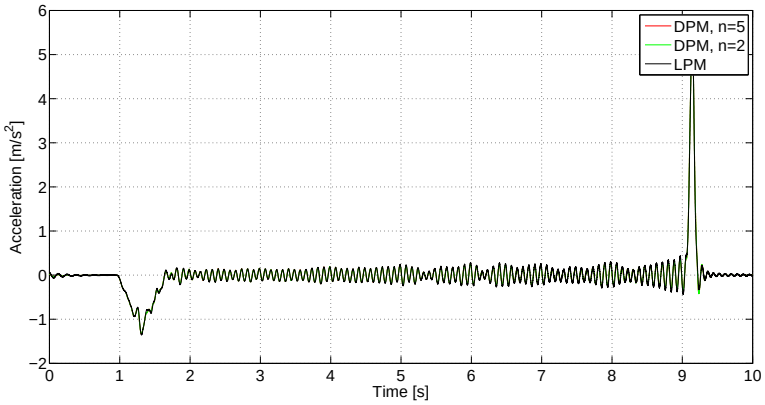

Figure 5.11: Simulated car acceleration by the DPM with 2 terms (green), the DPM with 5 terms (red) and the LPM

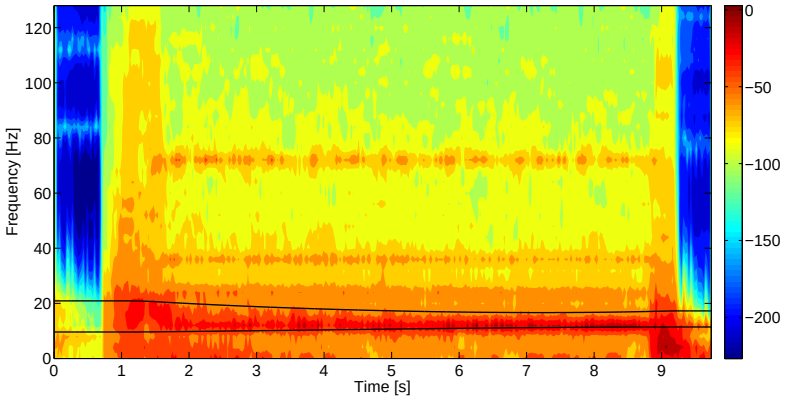

Figure 5.12: Spectrogram of the counterweight acceleration

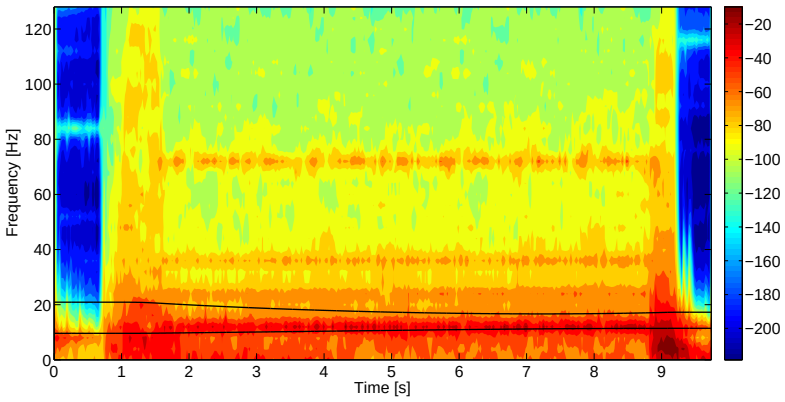

Figure 5.13: Spectrogram of the car acceleration

6

Measurements

A number of tests are performed on a 1:1 roping configuration laboratory model.
First, some tests are carried out to estimate the rope elasticity modulus.
Other tests consist of measuring the acceleration response at the suspended masses and at the drive machine, the machine shaft velocity and the three phase current intensities supplied to the machine during several travels. The machine torque is estimated from the current intensities.
Viscous friction at the guide-rail contact and at the machine are estimated from the experimental tests.
The measured and simulated acceleration responses, either in time or frequency domain, are compared and it is shown that the elevator car vibrates at frequencies generated at the machine, especially when they are close to the system natural frequencies.

6.1 Tests in elevator installations

A number of tests have been fulfilled on real elevator installations.
One of the tests consists of measuring acceleration responses during an elevator travel. Accelerometers have been placed on the car floor and on the ropes (see Fig. 6.1). It has been observed that excitation frequencies generated at the machine are present in the acceleration measured on the car floor.
Some other tests have been performed to obtain the natural frequencies of the system. For instance, for a certain car position, a force has been applied to the elevator car

by either an impact hammer or an inertial shaker[1] (see Fig. 6.2), both the applied force and the acceleration car have been measured and the frequency response functions between them calculated. The results show some natural frequencies, but it is not clear whether they correspond to the whole system, due to the rope elasticity, or, for instance, to a particular component of the car-frame.
The acceleration measured by the accelerometer placed on the rope (see Fig. 6.1) shows a similar frequency content in the three directions of the space, due to coupling.

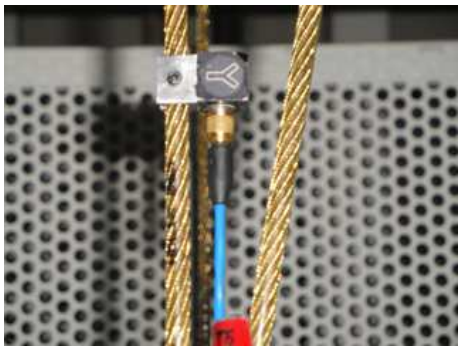

Figure 6.1: Accelerometer attached to the rope

Figure 6.2: Inertial shaker at the bottom of the car

Operational modal analysis (OMA) has been applied (22) in order to identify car natural frequencies and mode shapes during an elevator travel, and a rigid body mode corresponding to the first natural frequency of the system could have been identified.
Some tests have been carried out to identify passages through resonances. The acceleration response of the elevator car during a travel has been measured either with or

[1] Gearing & Watson V100 with Trunnion T100 and amplifier DSA1

without additional excitation force applied at a certain frequency and supplied by the previous inertial shaker placed at the bottom of the car. No clear conclusion has been obtained.

To summarise, although some rough conclusions can be obtained from measurements performed on a real elevator installation, tests fulfilled on a simpler laboratory model can be more helpful to check the simulation models.

6.2 Laboratory model

The schematic of the laboratory model and the experimental setup are shown in Fig. 6.3.

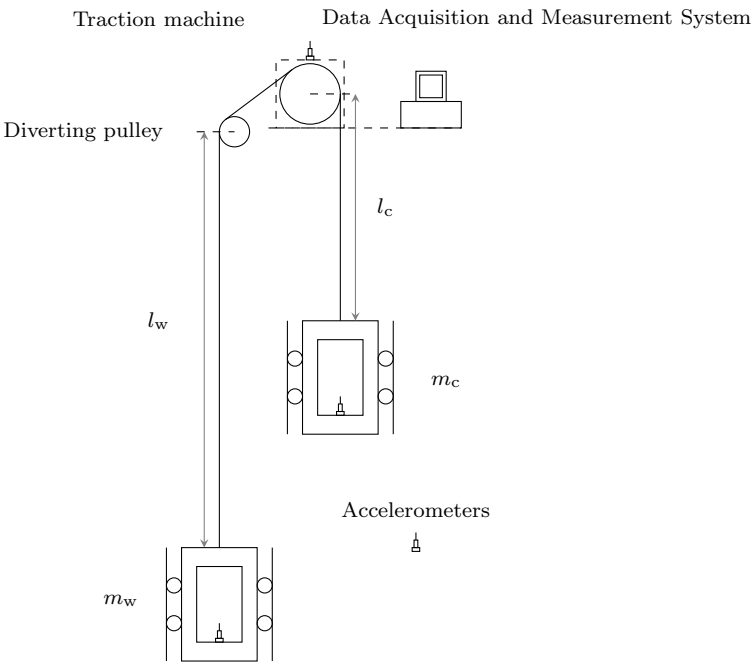

Figure 6.3: Experimental setup

Two equal rigid rigs are suspended at each side of the traction sheave by one wire rope and guided vertically as illustrated in Fig. 6.4.

A finite element model of the car or counterweight frame assemblies has been developed in order to calculate its natural frequencies with the first natural frequency determined

Figure 6.4: Setup frame

as around 235 Hz.

Fig. 6.5 shows the machine assembly with the traction sheave and the diverting pulley.

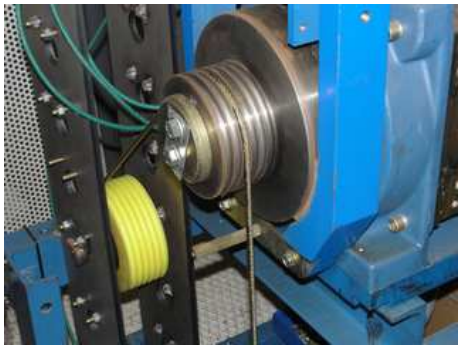

Figure 6.5: Machine, traction sheave and diverting pulley

The suspended rig at the diverting pulley side will be referred to as the counterweight, and that one suspended directly from the traction sheave as the car. Both rigs have got the same mass, 33 kg, but there is the possibility to increase it by placing some weights on them. The length from the car to the traction sheave is l_c and that one from the counterweight to the diverting pulley is $l_w = l_t - l_c$, where l_t =8.6 m. Other approximate values of the system parameters are $I = 0.3385$ kg·m^2, $r = 0.065$ m and

$\mu = 0.095$ kg/m.

6.3 Elasticity modulus of the rope

Experimental tests have been carried out in order to determine the value of the product of the rope elasticity modulus and the cross-section area EA. The determination of the value of EA is based on the characteristic equation (Eqn. 6.1) that gives the natural frequencies of a system that consists of a rope with a fixed end and a suspended mass at the other end ((28)).

$$m_c \gamma_n \sin(\gamma_n l) - m \cos(\gamma_n l) = 0 \tag{6.1}$$
$$f_n = \frac{1}{2\pi} \gamma_n \sqrt{\frac{EA}{m}}$$

where l is the length of the rope and f the natural frequency. According to the system described by Eqn. 6.1, the machine (see Fig. 6.5) is not working and the rope top end is fixed. The sensors used are given in Table 6.1.

Acquisition system	B&K Pulse
Accelerometers	B & K 4371, s.n. 1573419
Charge amplifiers	B & K 2635, s.n. 1602883

Table 6.1: Measurement system

It is measured the transitory acceleration response of the suspended mass, for different mass values and rope lengths, and the system first natural frequency and corresponding damping ratio are identified from the acceleration signal power spectrum. For instance, Fig. 6.6 shows the frame acceleration for the case of a suspended mass of 153 kg and a 4 m long rope and Fig. 6.7 the average PSD in the interval 1-1.5 s estimated by the Burg algorithm (50), given in dB/Hz relative to the reference value of 1 m/s^2.
Table 6.2 shows the average results obtained.
The values of the product EA for the different suspended masses can be seen in Fig. 6.8.

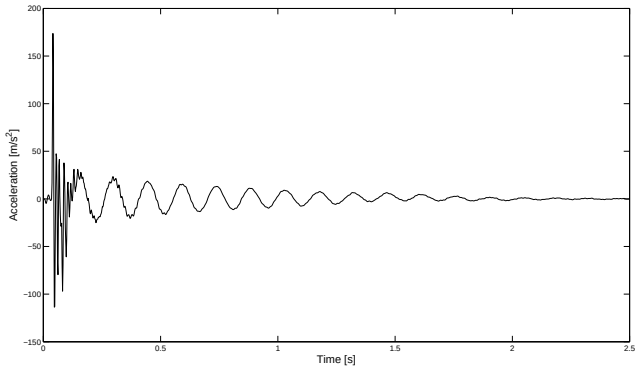

Figure 6.6: Acceleration of the frame after a hammer impact

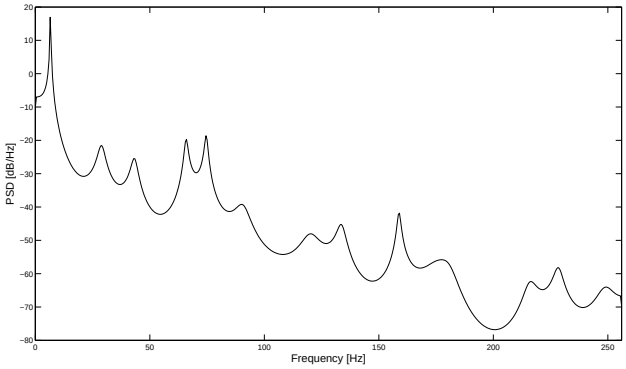

Figure 6.7: PSD of the frame acceleration in the 1-1.5 s interval

It can be concluded that as the tension of the rope increases the value of EA increases as well. The slope of the curve decreases as the value of the mass increases.
An average value of $EA = 10^6$ N has been assumed in the simulations.

6.4 Tests during elevator travels

The values of the system parameters considered in the computer simulations in section 5.3 correspond to the laboratory model described in section 6.2. Those simulation results have been compared to those obtained from experimental tests performed on the laboratory model (see Fig. 6.3).

Mass [kg]	Length [m]	Frequency [Hz]	Damping ratio [%]
33	6	9.6	4.1
	4	11.3	3.6
	2	14.1	4.0
57	6	8.4	6.2
	4	9.8	3.0
	2	12.6	4.2
105	6	6.6	9.3
	4	8.0	2.7
	2	10.4	6.0
153	6	5.7	7.0
	4	6.9	4.0
	2	9.2	10.7
201	6	5.1	6.3
	4	6.1	3.9
	2	8.5	11.9

Table 6.2: First natural frequency and damping ratio of a suspended mass system

6.4.1 Measurement procedure

Three accelerometers, each with its corresponding charge amplifier (see Table 6.1) have been placed on the frames at the car and at the counterweight side respectively, and on the machine (see Fig. 6.3).

The accelerations have been recorded during a travel together with the encoder signal, proportional to the actual velocity of the machine shaft, and the current intensities of the three phases feeding the machine, measured by current transducers. The sampling frequency has been set as 16384 Hz.

Several tests have been carried out, with the rigs travelling in both directions; the mass of the counterweight set as $m_w = 33$ kg in all the tests and the mass of the car m_c has taken four different values: 33, 45.5, 58 and 70.5 kgs.

6.4.2 Measured torque ripple

Fig. 5.8 shows the reference velocity and counterweight-side rope length time profiles corresponding to one of the test travels; in this particular case, m_w =33 kg and

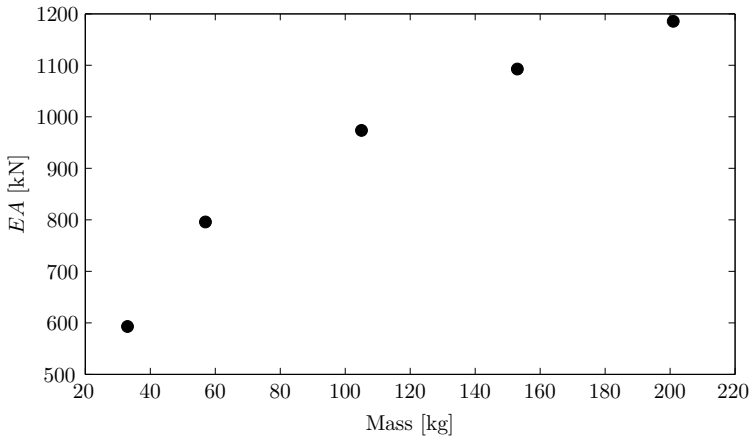

Figure 6.8: Values of the product EA as a function of the suspended mass

m_c =70.5 kg. The velocity profile is composed of acceleration and deceleration stages and a constant velocity stage where the rig velocity is around 0.4 m/s.
The machine torque has been estimated from the measured three phase current intensities by means of the quadrature zero (dqo) transformation theory (48) and Eqn. 5.9. Fig. 6.9 shows the torque time plot corresponding to the time profiles shown in Fig. 5.8.

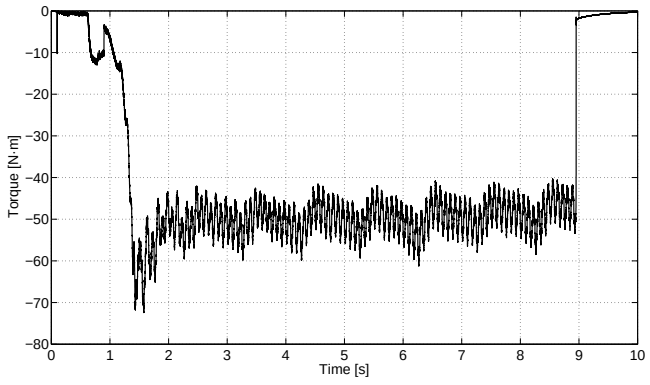

Figure 6.9: Machine torque for the case m_w =33 kg and m_c =70.5 kg

According to the reference system in Fig. 5.3, the torque assumes negative values. During the constant velocity stage, the absolute mean value of the torque decreases slightly, because the car-side rope length and mass decrease during the travel and a

smaller torque is needed.

There is a very apparent oscillation of the torque with period at around one second, which corresponds to the period of rotation of the machine shaft, possibly due to imbalance of the machine.

At the deceleration stage, it is not the machine controller that stops the travel, but the machine brake is applied. This scenario is reflected in the torque diagram at the end of the travel.

Fig. 5.9 shows the average power spectral density of the torque ripple during the constant velocity stage. The frequency components corresponding to the main electromagnetic torque ripple, the cogging and the main component of the radial force, 36, 72 and 12 Hz respectively, are apparent, but there are also components at 1 Hz, due to the machine imbalance, 6 Hz, the electric frequency (the frequency of the stator currents), and some of its harmonics (18 Hz, 24 Hz). The actual amplitudes of the electromagnetic (36 Hz) and cogging torque (72 Hz) components obtained from the measured current intensities are around 0.3 Nm and 0.5 Nm respectively and differ from the amplitudes calculated by FEA (Table 5.1). The amplitudes of the frequency components at 1 Hz, 6 Hz and 12 Hz are around 2 Nm, 0.3 Nm and 3.5 Nm respectively.

6.4.3 Experimental results

Fig. 6.10 show the counterweight and car accelerations recorded during the travel described in section 6.4.2, where the counterweight and car masses were m_{w} =33 kg and m_{c} =70.5 kg respectively and the velocity profile was given by Fig. 5.8 (a). Frequencies below 1 Hz have been filtered out.

Figs. 6.11 and 6.12 show the spectrograms of the accelerations measured by the sensors placed on the car and the counterweight respectively. The spectrograms, in dB/Hz (dB relative to the reference value of 1 $\mathrm{m/s^2}$), have been calculated by the Burg algorithm (50). The frequency band shown corresponds to the interval 0-128 Hz. The natural frequencies of the system in that band have been traced as well.

When analysing the frequency content of the accelerations recorded, it must be considered that there is a diverting pulley between the sheave and the counterweight, that could damp vibration.

The main electromagnetic torque ripple and the cogging torque frequency values are respectively 6 and 12 times the fundamental frequency ω_{s}, which is around 6 Hz at

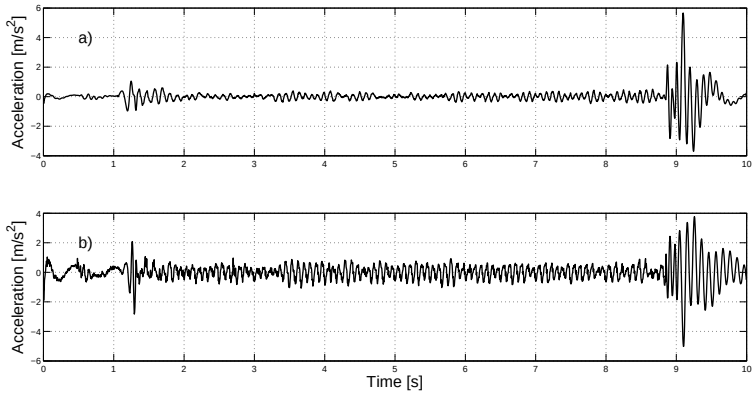

Figure 6.10: Accelerations of a) the car and b) the counterweight

the rated speed of the system. Those frequencies are 36 Hz and 72 Hz respectively. Furthermore, the 2nd order component of the radial force is around 12 Hz. All these frequencies appear in the spectrograms shown in Figs. 6.11 and 6.12. Vibration amplitude at the excitation frequency of 12 Hz is particularly high due to its proximity to the second natural frequency of the system. Fig. 6.11 shows that during the constant velocity stage the amplitude corresponding to the frequency of around 12 Hz increases progressively; it could be because the 3rd natural frequency gets progressively closer to this frequency. However, this feature is not quite clear in Fig. 6.12. Fig. 6.12 shows that there is an excitation frequency at 24 Hz; this could correspond to the component of spatial order 4 in the radial force (see Fig. 5.7). Although its amplitude is not so high in the FEM calculation, it could be due to its proximity to the 2nd natural frequency.

6.4.4 Friction and energy losses at the machine

Viscous friction and any other possible energy loss at the machine have been accommodated in the parameter c_{sh}. A rough estimate of its value has been obtained by applying the following equation that is satisfied during the constant velocity stage when $m_{\mathrm{c}} = m_{\mathrm{w}}$

$$\tau/r - c_{\mathrm{sh}}\dot{\theta}r - c_{\mathrm{w}}\dot{\theta}r - c_{\mathrm{c}}\dot{\theta}r = 0 \tag{6.2}$$

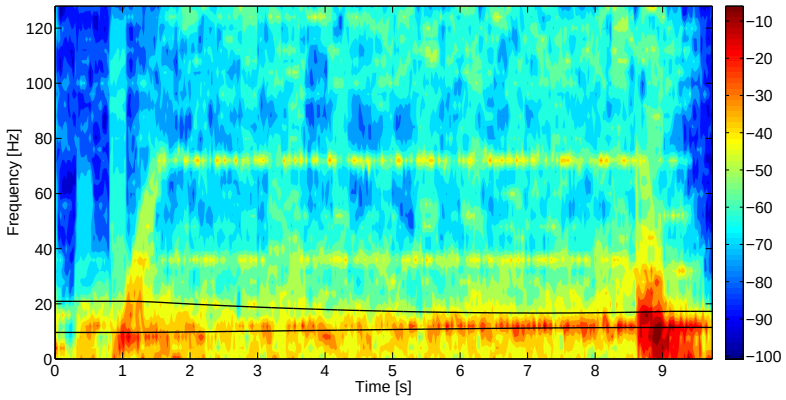

Figure 6.11: Spectrogram of the acceleration measured on the car

where τ is the torque measured at the corresponding travel and $\dot{\theta}$ the shaft velocity. The value obtained is around 3 kg/s.

6.4.5 Damping at the rail-guide contact

The value of ζ_i in Eqn. 5.36 has been calculated by Eqn. 5.52. Based on the exponential decrease in the amplitude shown in Fig. 6.10 when the rigs stopped at the end of the travel, the value obtained is around 0.036. The same value of ζ has been assumed for all modes. The values of c_{w} and c_{c} are assumed to be equal and calculated by Eqn. 5.53. The value obtained is around 148 kg/s.

6.5 Comparison of experimental ad simulation results

Figs. 6.13 and 6.14 show the comparison between the recorded and the simulated counterweight and car accelerations respectively where a highpass filter with the cut-off frequency at 1 Hz has been applied to both signals (simulated and measured).
The spectrogram of the simulated counterweight and car accelerations is shown in Figs. 5.12 and 5.13.
The excitation frequencies corresponding to the main electromagnetic torque ripple, the cogging and the second order component of the radial force, particularly manifest due to its proximity to the first natural frequency, can be observed.

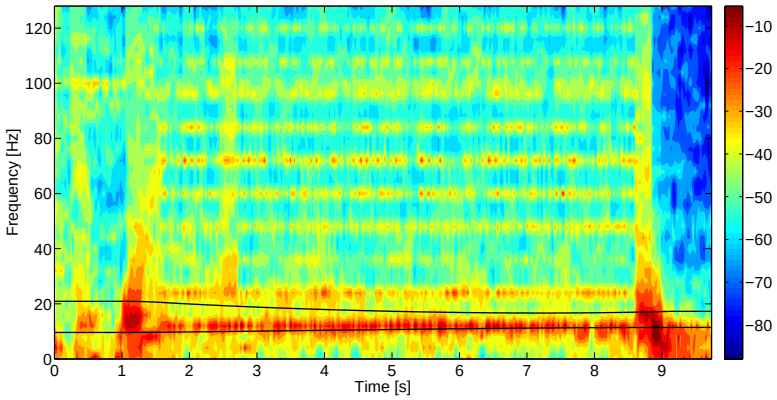

Figure 6.12: Spectrogram of the acceleration measured on the counterweight

The progressive increase in amplitude during the constant velocity stage at the excitation frequency of 12 Hz that was observed in the acceleration recorded on the car (see Fig. 6.10) is observed as well in the simulated one (see Fig. 6.14); however, it is not so evident in the counterweight acceleration (see Fig. 6.13).

Regarding the deceleration stage, in the simulation it is the machine controller that stops the travel, while it is the brake in the experimental tests, causing high vibrations, that are not observed in the simulation results.

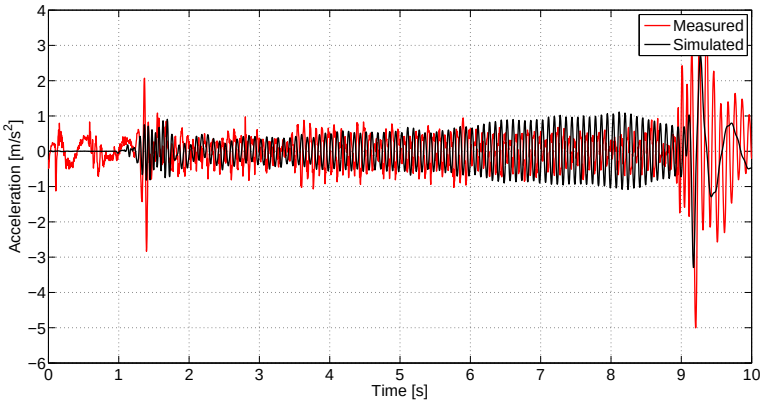

Figure 6.13: Recorded (red) and simulated (black) counterweight accelerations

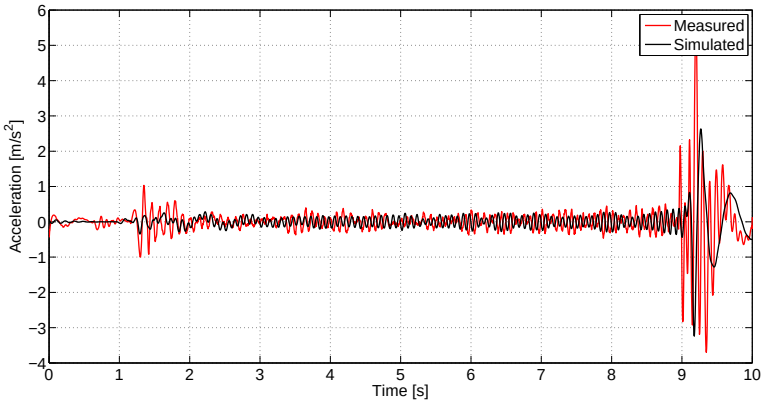

Figure 6.14: Recorded (red) and simulated (black) car accelerations

6.6 Conclusions

Experimental tests have been performed using a laboratory model to study vertical vibrations of the car and counterweight assembly due to excitations generated at the drive system in an elevator installation.

Simultaneous accelerations of the setup components, the velocity signal provided by the encoder, and the three phase motor currents have been recorded during a number of travels for a range of suspended masses. The torque supplied by the machine has been estimated from the phase current intensities.

Estimates of values of the rope elasticity modulus and the friction coefficients have been obtained from experimental tests and used in the simulations.

The accelerations obtained in the simulations are similar in amplitude and frequency content to the corresponding measured dynamic signals. It is shown that the drive-system borne excitation frequencies close to the elevator system natural frequencies appear in the car- and counterweight-frame acceleration signals.

The proposed simulation models can be used as design and analysis tools in the development of high-performance elevator systems.

7

Elevator 2:1 roping configuration

In this chapter a 2:1 roping configuration elevator system is considered and machine generated elevator vertical vibrations investigated.
The 2:1 roping configuration system is modelled as an assemblage of one-dimensional distributed subsystems, the rope segments, with lumped inertia elements (car, counterweight, traction sheave, pulleys) at their ends, and acting together as a single system due to constraints imposed between adjacent subsystems. It is assumed that:

- All inertia elements are lumped at their corresponding points.
- The rope material is uniform.
- The sheave is perfectly rigid and there is no rope slip across it.
- Only longitudinal motion is admitted in the rope subsystems.

The eigenvalue problem is solved analytically and the natural frequencies and corresponding mode shapes obtained.
The machine torque ripple and the radial forces generated at the machine air-gap between the stator and the rotor are computed using FEM simulation.
The acceleration response at the suspended masses and at the drive machine end in a laboratory model is measured during the system travel.
The experimental results confirm the FEM simulation results obtained concerning the excitation frequencies.
It is confirmed as well that the excitation frequencies close to the natural frequencies of the system are particularly magnified at the setup rig.

7.1 Natural frequencies and mode shapes

The natural frequencies and mode shapes of a 2:1 roping configuration elevator system (see Fig. 7.2) are calculated in this section.

The ropes are assumed to be continuous and homogeneous one-dimensional continua. It is assumed as well that they do not slip on the sheave.

The inertia elements are lumped at their corresponding discrete points. Both the car and counterweight are composed of two elements, the frame, represented by a rectangle, and a pulley, represented by a circle. Fig. 7.1 shows the corresponding scheme and the variables involved.

The mass of the car (the car pulley included) and the radius and moment of inertia of the corresponding pulley are m_1, r_1 and I_1 respectively. The corresponding parameters of the counterweight are m_2, r_2 and I_2. The mass density, the elasticity modulus and the cross section area of the ropes are μ, E and A respectively. The whole length of the rope is l_t.

An inertial reference frame fixed at the ceiling will give the equilibrium position of any section of the cable, x.

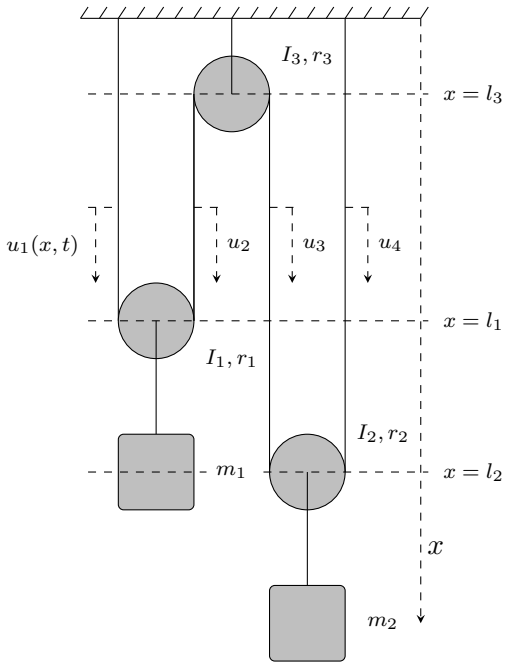

Figure 7.1: Model of a 2:1 configuration

There are two variables describing the displacement of the suspended masses: the acceleration of the centre of mass and the rotation angle of the pulley. Those describing the movement of the car are $u_{c,1}(t)$ and $\theta_1(t)$, and for the counterweight $u_{c,2}(t)$ and $\theta_2(t)$. It is assumed that the centre of masses of the traction sheave is fixed ($u_{c,3}(t) = 0$) and $\theta_3(t)$ will be the variable describing its angle of rotation.
The cable will be divided into four parts in order to describe the dynamic displacement of any of its points:

- The part from the ceiling to the car pulley, whose displacement will be given by $u_1(x,t)$ for $0 \leq l \leq l_1$.
- The part from the traction sheave to the car pulley, whose displacement will be given by $u_2(x,t)$ for $l_3 \leq l \leq l_1$.
- The part from the traction sheave to the counterweight pulley, whose displacement will be given by $u_3(x,t)$ for $l_3 \leq l \leq l_2$.
- The part from the ceiling to the counterweight pulley, whose displacement will be given by $u_4(x,t)$ for $0 \leq l \leq l_2$.

The following relations are satisfied between the displacement of the centres of masses and the rotation angles of the pulleys of the car and counterweight, and the traction sheave and those of the cable displacement functions.

$$u_{c,1}(t) = \frac{1}{2}\left[u_1(l_1,t) + u_2(l_1,t)\right] \tag{7.1}$$

$$u_{c,2}(t) = \frac{1}{2}\left[u_3(l_2,t) + u_4(l_2,t)\right] \tag{7.2}$$

$$u_{c,3}(t) = 0 \tag{7.3}$$

$$\theta_1(t) = \frac{1}{2r_1}\left[u_1(l_1,t) - u_2(l_1,t)\right] \tag{7.4}$$

$$\theta_2(t) = \frac{1}{2r_2}\left[u_3(l_2,t) - u_4(l_2,t)\right] \tag{7.5}$$

$$\theta_3(t) = \frac{1}{r_3}u_3(l_3,t) \tag{7.6}$$

The dynamics of the system of Fig. 7.1 is described by the following set of PDE.

$$mu_{i,tt}(x,t) - EAu_{i,xx}(x,t) = 0, \ \forall i = 1,...,4 \tag{7.7}$$

The corresponding boundary conditions for the set of Eqns. 7.7 are

$$u_1(0,t) = 0 \tag{7.8}$$
$$u_4(0,t) = 0 \tag{7.9}$$
$$m_1\ddot{u}_{c,1}(t) + EA\, u_{1,x}(l_1,t) + EA\, u_{2,x}(l_1,t) = 0 \tag{7.10}$$
$$I_1\ddot{\theta}_1(t) + EA\, u_{1,x}(l_1,t)r_1 - EA\, u_{2,x}(l_1,t)r_1 = 0 \tag{7.11}$$
$$m_2\ddot{u}_{c,2}(t) + EA\, u_{3,x}(l_2,t) + EA\, u_{4,x}(l_2,t) = 0 \tag{7.12}$$
$$I_2\ddot{\theta}_2(t) + EA\, u_{3,x}(l_2,t)r_2 - EA\, u_{4,x}(l_2,t)r_2 = 0 \tag{7.13}$$
$$u_2(l_3,t) = -u_3(l_3,t) \tag{7.14}$$
$$u_{2,x}(l_3,t)r_3 - u_{3,x}(l_3,t)r_3 + I_3\ddot{\theta}_3(t) = 0 \tag{7.15}$$

where $()_x$ means the derivative with respect to x.
We search for solutions to the set of Eqns. 7.7 with boundary conditions 7.8-7.15 of the form

$$u_i(x,t) = q(t)\Phi_i(x),\ \forall i = 1,...,4 \tag{7.16}$$

The following ODEs are obtained by substituting the derivatives of the Eqn. 7.16 into the set of PDEs 7.7.

$$\ddot{q}(t) + \omega^2 q(t) = 0 \tag{7.17}$$
$$\Phi''(x) + \gamma^2\Phi(x) = 0 \tag{7.18}$$
$$\gamma^2 = \frac{\mu}{EA}\omega^2 \tag{7.19}$$

Thus, the Eqn. 7.16 will have the following form in order to satisfy the ODEs 7.17 and 7.18.

$$u_i(x,t) = (A_i\sin(\gamma x) + B_i\cos(\gamma x))\sin(\omega t),\ \forall i = 1,...,4 \tag{7.20}$$

From condition 7.8, it results

$$u_1(x,t) = A_1 q(t)\sin(\gamma x) \tag{7.21}$$

In a similar manner, from condition 7.9,

$$u_4(x,t) = A_4 q(t) \sin(\gamma x) \tag{7.22}$$

Exp. 7.1 is differentiated twice with respect to time (it involves the second derivatives with respect to time of $u_1(l_1,t)$ and $u_2(l_2,t)$ given by Eqn. 7.20), and $u_1(x,t)$ and $u_2(x,t)$ are differentiated with respect to x and evaluated at l_1. The resulting expressions are introduced into Eqn. 7.10. Then, by means of Eqns. 7.18 and 7.19, we obtain

$$(A_1 + A_2)\, f_1(\gamma) + B_2 f_2(\gamma) = 0 \tag{7.23}$$

$$f_1(\gamma) = \frac{1}{2}\frac{m_1}{\mu}\gamma \sin(\gamma l_1) - \cos(\gamma l_1) \tag{7.24}$$

$$f_2(\gamma) = \frac{1}{2}\frac{m_1}{\mu}\gamma \cos(\gamma l_1) + \sin(\gamma l_1) \tag{7.25}$$

In a similar manner, Eqn. 7.4 is differentiated twice with respect to time, and the resulting one together with $u_{1,x}(l_1,t)$ and $u_{2,x}(l_1,t)$ obtained before is introduced into Eqn. 7.11 to obtain

$$(A_1 - A_2)\, g_1(\gamma) - B_2 g_2(\gamma) = 0 \tag{7.26}$$

$$g_1(\gamma) = \frac{I_1}{2\mu r_1^2}\gamma \sin(\gamma l_1) - \cos(\gamma l_1) \tag{7.27}$$

$$g_2(\gamma) = \frac{I_1}{2\mu r_1^2}\gamma \cos(\gamma l_1) + \sin(\gamma l_1) \tag{7.28}$$

The same procedure is applied with Eqns. 7.2 and 7.5 and Eqns. 7.12 and 7.13 to obtain

$$(A_3 + A_4)\, f_3(\gamma) + B_3 f_4(\gamma) = 0 \tag{7.29}$$

$$f_3(\gamma) = \frac{1}{2}\frac{m_2}{\mu}\gamma \sin(\gamma l_2) - \cos(\gamma l_2) \tag{7.30}$$

$$f_4(\gamma) = \frac{1}{2}\frac{m_2}{\mu}\gamma \cos(\gamma l_2) + \sin(\gamma l_2) \tag{7.31}$$

$$(A_3 - A_4)\, g_3(\gamma) + B_3 g_4(\gamma) = 0 \tag{7.32}$$

$$g_3(\gamma) = \frac{I_2}{2\mu r_2^2}\gamma \sin(\gamma l_2) - \cos(\gamma l_2) \tag{7.33}$$

$$g_4(\gamma) = \frac{I_2}{2\mu r_2^2}\gamma \cos(\gamma l_2) + \sin(\gamma l_2) \tag{7.34}$$

In a like manner, from Eqn. 7.6 and Eqn. 7.15, it results

$$A_3 g_5(\gamma) + B_3 g_6(\gamma) - A_2 f_5(\gamma) + B_2 f_6(\gamma) = 0 \tag{7.35}$$

$$g_5(\gamma) = \frac{I_3}{\mu r_3^2}\gamma \sin(\gamma l_3) + \cos(\gamma l_3) \tag{7.36}$$

$$g_6(\gamma) = \frac{I_3}{\mu r_3^2}\gamma \cos(\gamma l_3) - \sin(\gamma l_3) \tag{7.37}$$

$$f_5(\gamma) = \cos(\gamma l_3) \tag{7.38}$$

$$f_6(\gamma) = \sin(\gamma l_3) \tag{7.39}$$

Finally, from Eqn. 7.14

$$(A_2 + A_3)\, f_6(\gamma) + (B_2 + B_3)\, f_5(\gamma) = 0 \tag{7.40}$$

As a result, it is obtained a set of linear algebraic equations formed by Eqns. 7.23, 7.26, 7.29, 7.32, 7.35 and 7.40 that can be expressed as

$$\mathbf{A}\mathbf{b} = \mathbf{0} \tag{7.41}$$

where

$$\mathbf{A} = \begin{bmatrix} f_1 & f_1 & f_2 & 0 & 0 & 0 \\ g_1 & -g_1 & -g_2 & 0 & 0 & 0 \\ 0 & 0 & 0 & f_4 & f_3 & f_3 \\ 0 & 0 & 0 & g_4 & g_3 & -g_3 \\ 0 & -f_5 & f_6 & g_6 & g_5 & 0 \\ 0 & f_6 & f_5 & f_5 & f_6 & 0 \end{bmatrix} \tag{7.42}$$

(7.43)

$$\mathbf{b} = [A_1\ A_2\ B_2\ B_3\ A_3\ A_4]^{\mathrm{T}} \tag{7.44}$$

In order the set of equations 7.41 to have other solution but the null, we have got that

$$\det \mathbf{A} = 0 \tag{7.45}$$

Eqn. 7.45 is the characteristic equation, the roots of which will provide us the natural frequencies of the system. It results,

$$\det \mathbf{A} = F_3(\gamma)F_1(\gamma) - F_2(\gamma)F_4(\gamma) = 0 \tag{7.46}$$

$$F_1(\gamma) = g_5(\gamma)f_4(\gamma)g_3(\gamma) + g_5(\gamma)f_3(\gamma)g_4(\gamma) - 2f_3(\gamma)g_3(\gamma)g_6(\gamma) \tag{7.47}$$

$$F_2(\gamma) = f_5(\gamma)f_2(\gamma)g_1(\gamma) + f_5(\gamma)f_1(\gamma)g_2(\gamma) + 2f_1(\gamma)g_1(\gamma)f_6(\gamma) \tag{7.48}$$

$$F_3(\gamma) = -f_2(\gamma)g_1(\gamma)f_6(\gamma) - f_1(\gamma)g_2(\gamma)f_6(\gamma) + 2f_1(\gamma)g_1(\gamma)f_5(\gamma) \tag{7.49}$$

$$F_4(\gamma) = f_4(\gamma)g_3(\gamma)f_6(\gamma) + f_3(\gamma)g_4(\gamma)f_6(\gamma) - 2f_3(\gamma)g_3(\gamma)f_5(\gamma) \tag{7.50}$$

In this case, the solution of the set of equations is

$$A_1 = \frac{1}{2}CF_4(\gamma)F_5(\gamma) \tag{7.51}$$

$$A_2 = -\frac{1}{2}CF_4(\gamma)F_6(\gamma) \tag{7.52}$$

$$A_3 = -\frac{1}{2}CF_3(\gamma)F_7(\gamma) \tag{7.53}$$

$$A_4 = \frac{1}{2}CF_3(\gamma)F_8(\gamma) \tag{7.54}$$

$$B_2 = Cf_1(\gamma)g_1(\gamma)F_4(\gamma) \tag{7.55}$$

$$B_3 = Cf_3(\gamma)g_3(\gamma)F_3(\gamma) \tag{7.56}$$

where C is an arbitrary constant and

$$F_5(\gamma) = f_1(\gamma)g_2(\gamma) - f_2(\gamma)g_1(\gamma) \tag{7.57}$$

$$F_6(\gamma) = f_2(\gamma)g_1(\gamma) + f_1(\gamma)g_2(\gamma) \tag{7.58}$$

$$F_7(\gamma) = f_4(\gamma)g_3(\gamma) + f_3(\gamma)g_4(\gamma) \tag{7.59}$$

$$F_8(\gamma) = f_3(\gamma)g_4(\gamma) - f_4(\gamma)g_3(\gamma) \tag{7.60}$$

Finally, the mode shapes are given by the following expressions

$$u_1(x,t) = \frac{1}{2}Cq(t)F_4(\gamma)F_5(\gamma)\sin(\gamma x) \tag{7.61}$$

$$u_2(x,t) = Cq(t)\left(-\frac{1}{2}F_4(\gamma)F_6(\gamma)\sin(\gamma x) + f_1(\gamma)g_1(\gamma)F_4(\gamma)\cos(\gamma x)\right) \tag{7.62}$$

$$u_3(x,t) = Cq(t)\left(-\frac{1}{2}F_3(\gamma)F_7(\gamma)\sin(\gamma x) + f_3(\gamma)g_3(\gamma)F_3(\gamma)\cos(\gamma x)\right) \tag{7.63}$$

$$u_4(x,t) = \frac{1}{2}Cq(t)f_3(\gamma)g_3(\gamma)F_3(\gamma)F_8(\gamma)\sin(\gamma x) \tag{7.64}$$

7.2 The laboratory setup

Fig. 7.2 shows the laboratory model with a 2:1 roping configuration where the experimental tests have been carried out. There is one only rope, 23 m long. The machine is half a meter over the ceiling. Fig. 7.3 shows the machine and the traction sheave. The approximate values of the parameters are as follows: the radius and moment of inertia of the traction sheave, $r = 0.08$ m and $I = 0.3385$ kg·m^2 respectively; the radius and moment of inertia of the car- and counterweight-pulleys, 0.08 m and 0.0029 kg·m^2 respectively; the mass of the suspended frames, 94 kg (see Fig. 7.4); the mass density of the rope, 0.095 kg/m, and the product of the elasticity modulus and the cross-section area, $EA = 10^6$ Pa.

Solving Eqn. 7.45 according to the values of the parameters given in Section 7.2, the natural frequencies of the setup (see Fig. 7.5) as a function of the length l_1 (see Fig. 7.1) are obtained. As the suspended masses are equal, Fig. 7.5 shows a symmetric graph with respect to the vertical axis $l_1 = 5.5$ m, that corresponds to the situation at which the distances from the car and the counterweight to the ceiling are equal.

Some natural frequencies decrease as l_1 increases; it suggests that those natural frequencies are associated to the car-rope subsystem, that lengthens; some others increase as l_1 increases (as l_2 decreases) and it suggests that they are related to the counterweight-rope subsystem, that shortens.

7.2.1 Finite element analysis of the motor

The diagram of the laboratory model drive system is the same as that one corresponding to the 1:1 roping cfg. (see Fig. 5.1).

The machine is a 16 pole permanent magnet synchronous motor comprising a stator

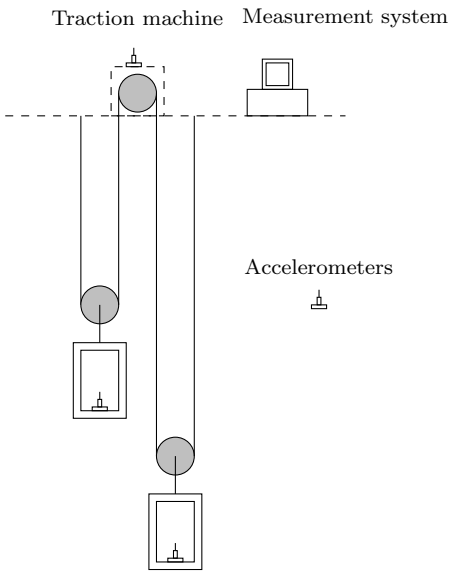

Figure 7.2: 2:1 roping configuration laboratory setup

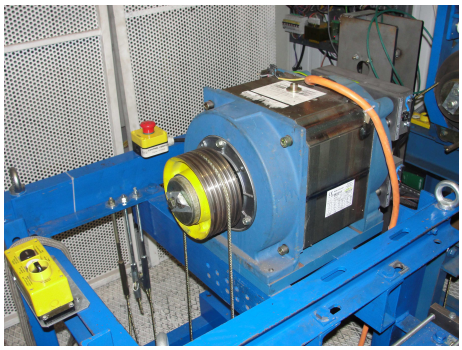

Figure 7.3: Machine and traction sheave

with 48 slots. The characteristics of this machine are summarised in Table 7.1. Its model is the same as in Fig. 5.2 and described in section 5.1.1.

The electric motor model uses some characteristic parameters such as inductances, resistance, magnet flux linkage and torque constants. All those parameters of the motor have been computed by Finite Element Analysis (FEA).

As the motor consist of p=8 pole pairs, the simulation geometry can be simplified to one pole pair domain. In Fig. 7.6 the magnetic field induced by the magnets around the geometry of the motor is shown.

Table 7.2 summarises the main motor parameters computed by FEA simulations.

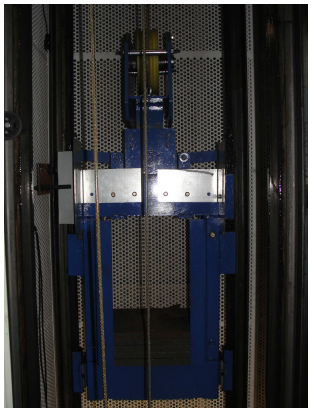

Figure 7.4: Hanging mass

Rated speed	382.5 rpm
Rated current	22.28 A
Rated torque	293 Nm
Maximum current	38.65 A
Maximum torque	513 Nm

Table 7.1: Machine characteristics

Apart from those components of the torque ripple considered, additional harmonics appear due to the radial magnetic forces between the stator and the rotor generated at the air-gap. The radial magnetic force per unit area or magnetic pressure waveform at any point of the air gap is obtained bay means of the Maxwell's stress tensor theorem (17) given by Eqn. 7.65.

$$p_{\mathrm{r}}(\theta,t) = \frac{1}{2\mu_0}\left(B_{\mathrm{n}}^2(\theta,t) - B_{\mathrm{t}}^2(\theta,t)\right) \tag{7.65}$$

where θ is the rotation angle with respect to the axis of symmetry of the machine, μ_0 is the magnetic permeability, t is the time, and B_{n} and B_{t} the normal and the tangential components of magnetic field around the air-gap. Fig. 7.7 shows the waveform of the magnetic radial pressure at a certain point of the stator core as a function of the rotor position. The spatial period of this signal is $\pi/4$ for symmetry reasons. Fig. 7.8 shows the components (spatial orders) in the corresponding Fourier series. The highest component corresponds to the spatial order 0 and it is a constant pressure; the spatial order 2 is a sinusoidal pressure distribution of spatial period $\pi/8$ and corresponding

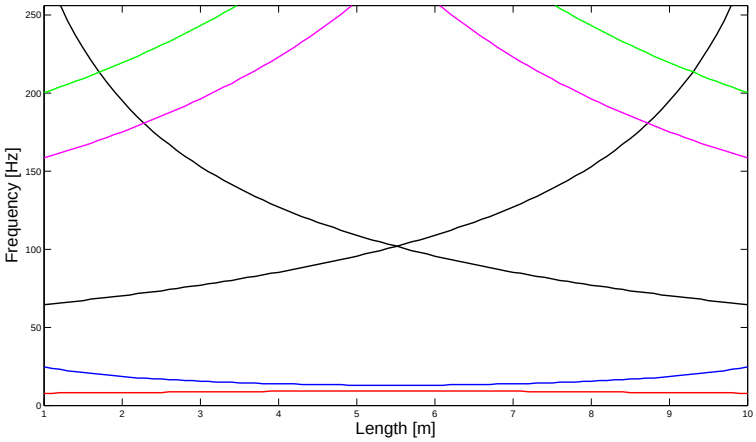

Figure 7.5: System natural frequencies versus length l_1 (first one in red; second one in blue; third one in black; fourth one in magenta and fifth one in green)

Coil Resistance	R_s	0.7 Ω
d-axis Inductance	L_d	7.16 mH
q-axis Inductance	L_q	9.86 mH
Magnet Flux Linkage	Ψ_pm(rms)	0.560 Wb
Average Torque Constant	K_τ	13.44 Nm/A
Torque Ripple Constant	$K_{\tau 12}$	0.0781 Nm/A
Cogging Torque Magnitude	$\Delta\tau_\mathrm{c}$	$<$ 0.1 Nm

Table 7.2: Parameters computed by FEA simulations

excitation frequency twice the fundamental one, $2\omega_\mathrm{s}$, and it is the main harmonic of the radial force.

7.3 Measurements

Fig. 7.2 shows a scheme of the setup with the acquisition system. Three accelerometers, each with its corresponding charge amplifier (look at Table 7.3) have been placed on both frames and on the machine.

The velocity profile (see Fig. 7.9) is composed of acceleration and deceleration

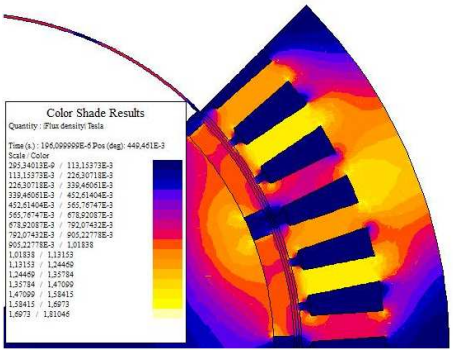

Figure 7.6: Spatial distribution of the magnetic field induced by the magnets

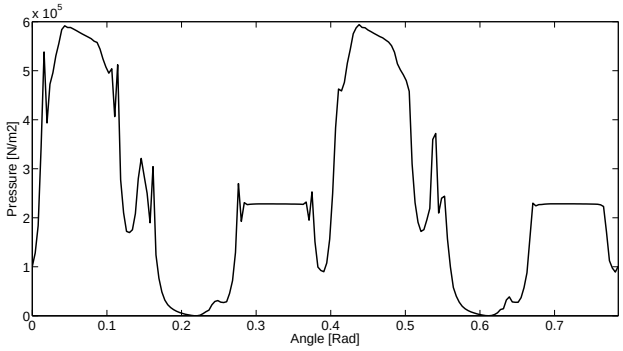

Figure 7.7: Magnetic radial force per unit area at rated load condition

periods and a constant velocity stage where the car velocity is around 1.4 m/s (ω_m = 35 rad/s). During the travel, the car (the left rig at Fig. 7.1) moves from the initial position l_1 = 8.5 m to the final l_1 = 2.3 m. The rigs are at the same height when l_1 = 5.5 m, which occurs around t =10 s.

The acceleration signals measured have been sampled at 512 Hz. Fig. 7.10 shows the accelerations of a) the machine, b) the counterweight and c) the car obtained. Low frequencies up to 2 Hz have been filtered.

Acquisition system	B&K Pulse
Accelerometers	B & K 4371, s.n. 1573419
Charge amplifiers	B & K 2635, s.n. 1602883

Table 7.3: Measurement system

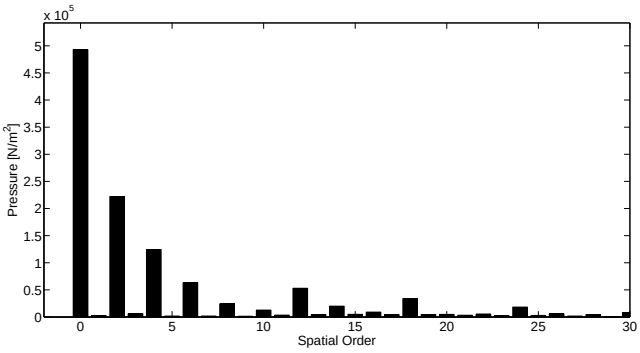

Figure 7.8: Fourier series components

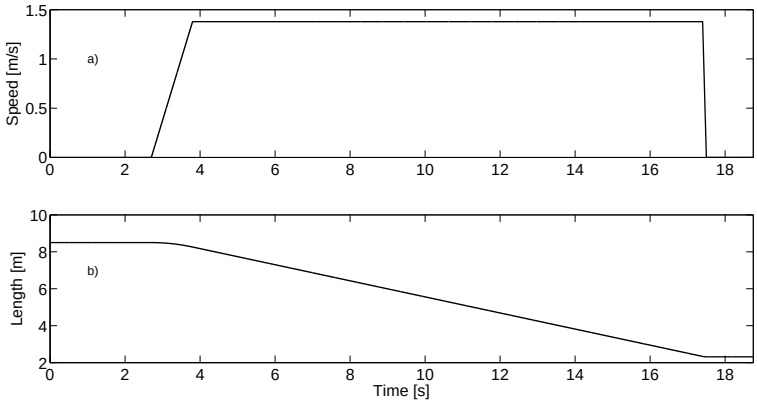

Figure 7.9: a) Velocity and b) displacement profiles

The evolution of the power spectral density (PSD) of the accelerations during the travel of the machine and the car have been represented in Figs. 7.11 and 7.12 respectively. The Burg algorithm (50) has been applied to obtain them, by means of the corresponding Matlab function. The Burg algorithm estimates the spectral content by fitting an autoregressive (AR) linear prediction filter model of a given order to the signal. Blocks of 200 samples with an overlapping of a 90% have been taken to estimate the frequency content. The order of the filter has been 150.

According to the conclusions obtained in Section 7.2.1, during the constant velocity stage of the system travel, the fundamental frequency ω_s is around 15 Hz, the main electromagnetic torque ripple around 90 Hz, the cogging torque frequency around 180 Hz and the main harmonic of the radial force around 30 Hz.

The acceleration measured on the machine (look at Fig. 7.11) shows clearly the pres-

ence of the fundamental frequency and all its multiples. Fig. 7.12 shows that some excitation frequencies are particularly amplified: the fundamental frequency at 15 Hz, as it close to the first two natural frequencies of the system (look at Fig. 7.5), the main harmonic of the radial force at 30 Hz, an important component of the torque ripple whenever there is any eccentricity in the machine shaft, and the electromagnetic torque ripple component at 90 Hz, close to the third natural frequency (look at Fig. 7.5). It is manifest as well a component at 60 Hz, at which there is an important component of the radial force (look at Fig. 7.8).

Besides, the vibration amplitude around the instant $t = 10$ s, for low frequencies, is particularly high, what can be due to the fact that the excitation frequency at 15 Hz and the first two natural frequencies (at 9 Hz and 13 Hz) are all the three very close to each other.

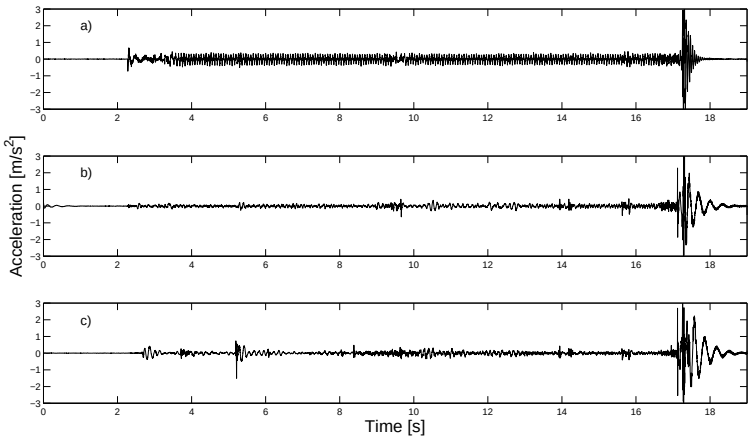

Figure 7.10: Accelerations of a) the machine , b) the car and c) the counterweight

7.4 Conclusions

The vertical vibration caused by torque ripple generated at the drive system is transmitted through the suspension ropes to the car.

Hoist ropes, due to their flexibility, loading conditions, and relatively low internal damping characteristics, largely determine the resonances within the system and the amount of vibration.

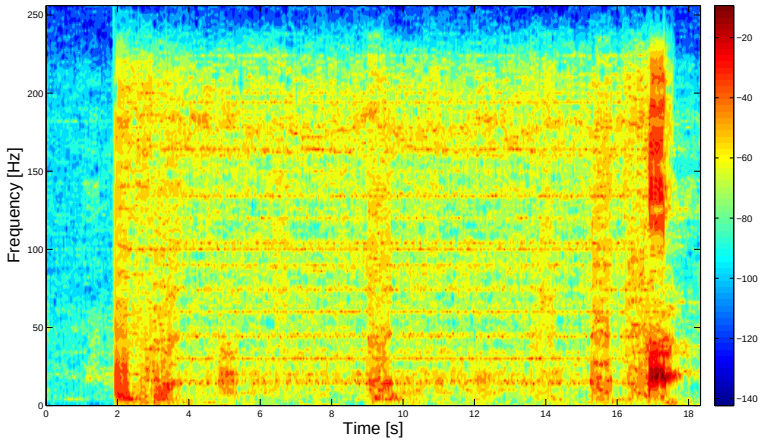

Figure 7.11: Machine acceleration PSD

A 2:1 roping configuration laboratory model has been represented as an assemblage of one-dimensional distributed subsystems, the rope segments, with lumped inertia elements (car, counterweight, traction sheave, pulleys) at their ends, and acting together as a single system due to constraints imposed between adjacent subsystems. The eigenvalue problem has been solved analytically and the natural frequencies and corresponding mode shapes obtained.

The machine torque ripple and the radial forces generated at the machine air-gap between the stator and the rotor have been computed using FEM simulation.

The acceleration response at the suspended masses and at the drive machine end in a laboratory model have been measured during a number of travels.

The experimental results corroborate the FEM simulation results obtained concerning the excitation frequencies.

It is confirmed as well that the excitation frequencies close to the natural frequencies of the system are particularly magnified at the setup rig.

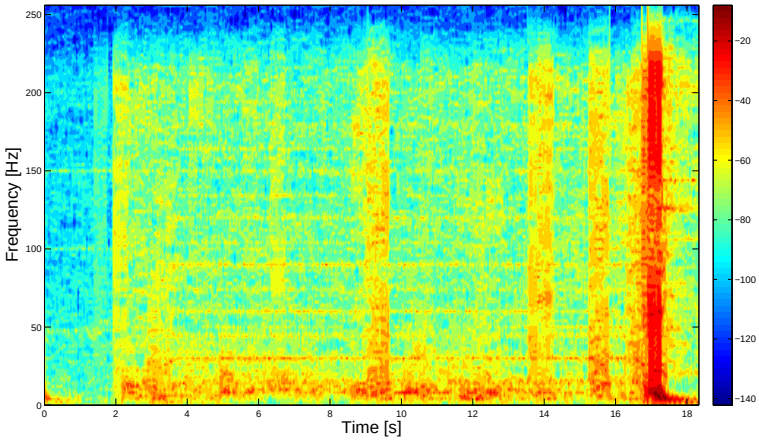

Figure 7.12: Car acceleration PSD

8

Summary and conclusions

8.1 Introduction

The primary objective of the thesis was stated as

"**The analysis of machine generated elevator car vertical vibrations**"

Thus, this research work has focused on one of the aspects of elevator ride quality: vertical vibration, particularly that one associated with the suspension ropes, and caused by the torque ripple generated at the drive system.
According to the main objective of the research and the conclusions drawn from the review of the literature, the following decisions were taken:

- Concerning the **elevator model** to be developed:
  - It has been developed a mathematical model of an elevator to study **only vertical vibrations**, because the coupling between the vertical and the lateral vibration has been neglected, and because the aim of the research is elevator vertical vibrations caused by vertical excitation forces.
  - The **inertia elements** (the car assembly, the counterweight and the traction sheave) have been **lumped** at its corresponding points, and the elevator system is represented as a translating assembly of these inertia elements coupled and constrained by one-dimensional slender continua, which involves not considering dynamic issues such as those described in Section 1.4.4.

  - A **model of the whole assembly**, including the car, the counterweight, the ropes and the drive system has been developed, because the research to be done deals with excitation forces generated at the machine, that couples the car- and counterweight-side ropes through the traction sheave.
    A common drive system model, reported in the related literature, has been developed as well. The input to it is a desired reference velocity profile to be followed by the car.
  - Regarding the **ropes**, that are distributed-parameter media, **either lumped- or distributed-parameter models** have been developed.

- With respect to **experimental tests**, as a real elevator installation is complex enough to make difficult obtaining conclusions on the features of its dynamics, tests have been carried out in **laboratory models**.

- The influence of the machine generated **torque ripple** in elevator car vertical vibration has been specifically studied in this research.

8.2 Main contributions

Next, the main contributions of the research work are enumerated.
Regarding the **stationary model of the 1:1 roping configuration** elevator system:

- A closed-form solution of the distributed-parameter model equations describing the dynamics of the system has been obtained.
  The orthogonality properties of the mode shapes satisfying the equations have been obtained as well.

- A lumped-parameter model has been developed too and the following conclusions have been drawn with respect to the distributed parameter model:

  - The first three natural frequencies calculated using the DPM model and the LPM model compare very well (the first natural frequency is 0 Hz and corresponds to an overall transport motion of the system).

  - At higher frequencies there are some differences between the results that are obtained from these models.
    It has been demonstrated that if the rope is represented by a larger number of lumped masses so that the number of degrees of freedom in the LPM is increased, this model yields more accurate results with the differences between the frequencies calculated from the DPM and LPM being decreased.
  - The car, the counterweight and the sheave are located at the nodes for all higher mode shapes from the 4th onwards.

Regarding the **non-stationary model of the 1:1 roping configuration** elevator system:

- It **includes the drive system**, with the machine and its controllers, whose characteristics have been calculated by the electromagnetic FEM software FLUX. The torque ripple amplitude has also been computed.
- A **novel distributed-parameter model** has been developed, as well as a lumped-parameter model. The DPM is described by a set of PDE that is solved by the Galerkin method.
- It is shown that only two modes contribute to the car and counterweight vibration responses and, as far as the prediction of the response of the car and the counterweight, it is concluded that **a five degree-of-freedom lumped-parameter model is as accurate as the distributed-parameter model**.

Concerning the experimental tests carried out in a 1:1 roping configuration elevator model, the most noteworthy is:

- **Simultaneous** car and counterweight **accelerations**, the **velocity** signal provided by the encoder, and the three phase motor currents from which to estimate the machine **torque** have been recorded during a number of travels for a range of suspended masses.
- Estimates of values of the rope **elasticity modulus** and the **friction coefficients** have been obtained from experimental tests and used in the simulations.

- The **accelerations** obtained in the **simulations** are **similar** in amplitude and frequency content to the corresponding **measured** dynamic signals.
- It is shown that the drive-system borne **excitation frequencies close to** the elevator system **natural frequencies appear in** the car- and counterweight-frame **acceleration** signals.

With respect to the 2:1 roping configuration elevator, the main conclusions are:

- A **closed-form solution of the distributed-parameter model equations** describing the dynamics of the system has been obtained.
- Similar experimental tests to those carried out in the case of the 1:1 roping cfg. show the **presence of machine generated excitation frequencies in the accelerations** measured.
- It is confirmed as well that the **excitation frequencies close to the natural frequencies** of the system are **particularly manifest** in the acceleration spectra of the suspended masses.

The proposed simulation models can be used as design and analysis tools in the development of high-performance elevator systems.

8.3 Publications

Related to the work developed, the following paper was accepted on June 1st 2013:

- X. Arrasate, S. Karczmarczyk, G. Almandoz, J.M. Abete, I. Isasa. The modelling, simulation and experimental testing of the dynamic responses of an elevator system. Mechanical Systems and Signal Processing.

The following papers have been presented in a number of Conferences:

- X. Arrasate, J. M. Abete and S. Kaczmarczyk. Distributed longitudinal vibration model of a lift system including the machine dynamics. 2nd International Conference on Experiments/Process/System Modelling/Simulation and Optimization. 2nd IC-EpsMsO, Athens (Greece). July 2007.

- X. Arrasate, J.M. Abete , S. Kaczmarczyk. The Simulation Model of the Vertical Dynamics and Control of an Elevator System. 2nd edition of the symposium of the Mechanics of Slender Structures. Baltimore, USA. July 2008.
- X. Arrasate, J.M. Abete , S. Kaczmarczyk. A Simulation Model of the Vertical Dynamics of an Elevator System. 3rd edition of the Symposium of the Mechanics of Slender Structures. Donostia-San Sebastin (Spain). July 2010.
- X. Arrasate, S. Kaczmarczyk, G. Almandoz, J.M. Abete, I. Isasa. The modelling and experimental testing of the vertical dynamic response of an elevator system with a 2:1 roping configuration. 25th International Conference on Noise and Vibration engineering (ISMA2012). Leuven (Belgium) 17-19 September 2012.
- X. Arrasate, S. Kaczmarczyk, G. Almandoz, J. M. Abete, I. Isasa. The Modelling, Simulation and Experimental Testing of Vertical Vibrations in an Elevator System with 1:1 Roping Configuration. 2nd Symposium on Lift and Escalator Technology. Northampton (UK), 26-27 September 2012.
- X. Arrasate, S. Kaczmarczyk, G. Almandoz, J.M. Abete, I. Isasa. Measurement and Simulation of Machine-Borne Vertical Vibration in Elevator Systems. International Conference on Vibration Problems. Lisbon (Portugal), 9-12 September 2013.

8.4 Future work

It has been demonstrated that the elevator car vibrates at frequencies generated at the drive system. The values of these excitation frequencies depend on the machine characteristics, such as the number of stator pole pairs or slots.
It has been shown as well that the proximity of an excitation frequency to any natural frequency of the system could make more manifest that tone in the car acceleration spectrum.
Currently the author is working on the design of new electrical machines for transportation systems that should minimise the torque ripple and whose main excitation frequencies should be far from the natural frequencies of the system.

Appendix A

Non-stationary model equations

In this appendix, it is derived the set of PDEs 5.14-5.18 in section 5.2.1.1 that describes the dynamics of the non-stationary model of the 1:1 roping configuration elevator. The extended Hamilton's principle (38) is applied, which means that

$$\int_{t_1}^{t_2} (\delta\mathcal{L} + \delta W)\,\mathrm{d}t = 0,\ \mathcal{L} = \mathcal{E} - \Pi_\mathrm{e} - \Pi_\mathrm{g} \tag{A.1}$$

where $\mathcal{L}$ is the system Lagrangian, $\mathcal{E}$ the kinetic energy, Π_e the rope elastic strain energy, and Π_g the system gravitational potential energy. δW is the virtual work done by the non-conservative forces. The kinetic energy of the system is expressed as

$$\begin{aligned}\mathcal{E} = &\int_0^{l_\mathrm{w}} \hat{\mathcal{E}}_\mathrm{w}(u_{\mathrm{w},t}, \dot{l}_\mathrm{w})\,\mathrm{d}s + \int_{l_\mathrm{w}}^{l_\mathrm{t}} \hat{\mathcal{E}}_\mathrm{c}(u_{\mathrm{c},t}, \dot{l}_\mathrm{w})\,\mathrm{d}s + \mathcal{E}_{m_\mathrm{w}}(u_{\mathrm{w},t}(0,t), \dot{l}_\mathrm{w}) + \\ &+\mathcal{E}_{m_\mathrm{sh}}(u_{\mathrm{w},t}(l_\mathrm{w},t), \dot{l}_\mathrm{w}) + \mathcal{E}_{m_\mathrm{c}}(u_{\mathrm{c},t}(l_\mathrm{t},t), \dot{l}_\mathrm{w})\end{aligned} \tag{A.2}$$

where $\hat{\mathcal{E}}_\mathrm{w}(u_{\mathrm{w},t}, \dot{l}_\mathrm{w})$ and $\hat{\mathcal{E}}_\mathrm{c}(u_{\mathrm{c},t}, \dot{l}_\mathrm{w})$ are the kinetic energy densities of the counterweight- and car-side ropes, and $\mathcal{E}_{m_\mathrm{w}}(u_{\mathrm{w},t}(0,t), \dot{l}_\mathrm{w})$, $\mathcal{E}_{m_\mathrm{sh}}(u_{\mathrm{w},t}(l_\mathrm{w},t), \dot{l}_\mathrm{w})$ and $\mathcal{E}_{m_\mathrm{c}}(u_{\mathrm{c},t}(l_\mathrm{t},t), \dot{l}_\mathrm{w})$ the kinetic energies of the counterweight, traction sheave and car, respectively. Those energy components are described by the following expressions

$$\hat{\mathcal{E}}_\mathrm{w}(u_{\mathrm{w},t}, \dot{l}_\mathrm{w}) = \frac{1}{2}\mu\left(u_{\mathrm{w},t} - \dot{l}_\mathrm{w}\right)^2 \tag{A.3}$$

$$\hat{\mathcal{E}}_c(u_{\mathrm{c},t}, \dot{l}_\mathrm{w}) = \frac{1}{2}\mu\left(u_{\mathrm{c},t} - \dot{l}_\mathrm{w}\right)^2 \tag{A.4}$$

$$\mathcal{E}_{m_\mathrm{w}}(u_{\mathrm{w},t}(0,t), \dot{l}_\mathrm{w}) = \frac{1}{2}m_\mathrm{w}\left(u_{\mathrm{w},t}(0,t) - \dot{l}_\mathrm{w}\right)^2 \tag{A.5}$$

$$\mathcal{E}_{m_{\mathrm{sh}}}(u_{\mathrm{w},t}(l_{\mathrm{w}},t),\dot{l}_{\mathrm{w}}) = \frac{1}{2}m_{\mathrm{sh}}\left(u_{\mathrm{w},t}(l_{\mathrm{w}},t)-\dot{l}_{\mathrm{w}}\right)^2,\ m_{\mathrm{sh}} = \frac{I}{r^2} \tag{A.6}$$

$$\mathcal{E}_{m_{\mathrm{c}}}(u_{\mathrm{c},t}\left(l_{\mathrm{t}},t\right),\dot{l}_{\mathrm{w}}) = \frac{1}{2}m_{\mathrm{c}}\left(u_{\mathrm{c},t}\left(l_{\mathrm{t}},t\right)-\dot{l}_{\mathrm{w}}\right)^2 \tag{A.7}$$

and $\dot{()}$ and $()_t$ express respectively differentiation and partial differentiation with respect to t.

The elastic strain energy of the ropes is

$$\Pi_e = \int_0^{l_{\mathrm{w}}} \hat{\Pi}_{\mathrm{w}}(u_{\mathrm{w},s})\ \mathrm{d}s + \int_{l_{\mathrm{w}}}^{l_{\mathrm{t}}} \hat{\Pi}_c(u_{\mathrm{c},s})\ \mathrm{d}s \tag{A.8}$$

where $()_{,s}$ denotes partial differentiation with respect to s, and $\hat{\Pi}_{\mathrm{w}}(u_{\mathrm{w},s})$ and $\hat{\Pi}_{\mathrm{c}}(u_{\mathrm{w},s})$ are the counterweight- and the car-side rope elastic strain energy densities respectively. Those are given by

$$\hat{\Pi}_{\mathrm{w}}(u_{\mathrm{w},s}) = \frac{1}{2}EAu_{\mathrm{w},s}^2$$
$$\hat{\Pi}_{\mathrm{c}}(u_{\mathrm{c},s}) = \frac{1}{2}EAu_{\mathrm{c},s}^2$$

The gravitational potential energy calculated at the sheave level is

$$\Pi_{\mathrm{g}} = g\left[\mu\int_0^{l_{\mathrm{w}}} u_{\mathrm{w}}\ \mathrm{d}s - \mu\int_{l_{\mathrm{w}}}^{l_{\mathrm{t}}} u_{\mathrm{c}}\ \mathrm{d}s + m_{\mathrm{w}}u_{\mathrm{w}}(0,t) - m_{\mathrm{c}}u_{\mathrm{c}}(l_{\mathrm{t}},t) + \right.$$
$$\left. -m_{\mathrm{c}}l_{\mathrm{c}} - m_{\mathrm{w}}l_{\mathrm{w}} - \frac{1}{2}\mu l_{\mathrm{w}}^2 - \frac{1}{2}\mu {l_{\mathrm{c}}}^2\right] \tag{A.9}$$

where g is the acceleration of gravity.

The virtual work done by the machine torque is given by

$$\delta W = \frac{\tau}{r}\left(\delta u_{\mathrm{w}}(l_{\mathrm{w}}) - \delta l_{\mathrm{w}}\right) \tag{A.10}$$

Hamilton's principle requires that any virtual displacement, arbitrary between two instants t_1 and t_2, vanishes at the ends of the time interval, so that at $t = t_1$ and $t = t_2$

$$\delta u_{\mathrm{w}} = 0, \delta u_{\mathrm{c}} = 0, \delta u_{\mathrm{w}}(0,t) = 0, \delta u_{\mathrm{w}}(l_{\mathrm{w}},t) = 0, \delta u_{\mathrm{c}}(l_{\mathrm{t}},t) = 0, \delta l_{\mathrm{w}} = 0 \tag{A.11}$$

Regarding the kinetic energy,

$$\int_{t_1}^{t_2} \delta\mathcal{E}\mathrm{d}t = \int_{t_1}^{t_2} \delta\left(\int_0^{l_\mathrm{w}} \hat{\mathcal{E}}_\mathrm{w}(u_{\mathrm{w},t}, \dot{l}_\mathrm{w})\mathrm{d}s\right)\mathrm{d}t + \\ + \int_{t_1}^{t_2} \delta\left(\int_{l_\mathrm{w}}^{l_\mathrm{t}} \hat{\mathcal{E}}_\mathrm{c}(u_{\mathrm{c},t}, \dot{l}_\mathrm{w})\mathrm{d}s\right)\mathrm{d}t + \int_{t_1}^{t_2} \delta\mathcal{E}_{m_\mathrm{w}}(u_{\mathrm{w},t}(0,t), \dot{l}_\mathrm{w})\mathrm{d}t + \\ + \int_{t_1}^{t_2} \delta\mathcal{E}_{m_\mathrm{sh}}(u_{\mathrm{w},t}(l_\mathrm{w},t), \dot{l}_\mathrm{w})\mathrm{d}t + \int_{t_1}^{t_2} \delta\mathcal{E}_{m_\mathrm{c}}(u_{\mathrm{c},t}(l_\mathrm{t},t), \dot{l}_\mathrm{w})\mathrm{d}t \tag{A.12}$$

The first term in the sum to the right of the equal sign in Eqn. A.12 is developed as

$$\int_{t_1}^{t_2} \delta\left(\int_0^{l_\mathrm{w}} \hat{\mathcal{E}}_\mathrm{w}(u_{\mathrm{w},t}, \dot{l}_\mathrm{w})\mathrm{d}s\right)\mathrm{d}t = \int_0^{l_\mathrm{w}} \mathrm{d}s \int_{t_1}^{t_2} \delta\left(\hat{E}_\mathrm{w}(u_{\mathrm{w},t}, \dot{l}_\mathrm{w})\right)\mathrm{d}t \tag{A.13}$$

$$\delta\left(\hat{\mathcal{E}}_\mathrm{w}(u_{\mathrm{w},t}, \dot{l}_\mathrm{w})\right) = \mu\left(u_{\mathrm{w},t} - \dot{l}_\mathrm{w}\right)\left(\frac{\partial}{\partial t}\delta u_\mathrm{w} - \frac{d}{\mathrm{d}t}\delta l_\mathrm{w}\right) \tag{A.14}$$

Introducing A.14 into A.13, it is obtained

$$\int_{t_1}^{t_2} \delta\left(\hat{\mathcal{E}}_\mathrm{w}(u_{\mathrm{w},t}, \dot{l}_\mathrm{w})\right)\mathrm{d}t = \\ - \int_{t_1}^{t_2} \mu\left(u_{\mathrm{w},tt} - \ddot{l}_\mathrm{w}\right)\delta u_\mathrm{w}\mathrm{d}t + \int_{t_1}^{t_2} \mu\left(u_{\mathrm{w},tt} - \ddot{l}_\mathrm{w}\right)\delta l_\mathrm{w}\mathrm{d}t \tag{A.15}$$

where the conditions A.11 have been applied. Consequently,

$$\int_{t_1}^{t_2} \delta\left(\int_0^{l_\mathrm{w}} \hat{\mathcal{E}}_\mathrm{w}(u_{\mathrm{w},t}, \dot{l}_\mathrm{w})ds\right)\mathrm{d}t = \\ \int_{t_1}^{t_2} \mathrm{d}t\left[-\int_0^{l_\mathrm{w}} \mu\left(u_{\mathrm{w},tt} - \ddot{l}_\mathrm{w}\right)\delta u_\mathrm{w}\mathrm{d}s + \int_0^{l_\mathrm{w}} \mu\left(u_{\mathrm{w},tt} - \ddot{l}_\mathrm{w}\right)\delta l_\mathrm{w}\mathrm{d}s\right] \tag{A.16}$$

In a similar manner, the rest of terms in the sum to the right of the equal sign in Eqn. A.12 can be developed, to obtain

$$\int_{t_1}^{t_2} \delta\left(\int_{l_\mathrm{w}}^{l_\mathrm{t}} \hat{\mathcal{E}}_\mathrm{c}(u_{\mathrm{c},t}, \dot{l}_\mathrm{w})\mathrm{d}s\right)\mathrm{d}t = \\ \int_{t_1}^{t_2} \mathrm{d}t\left[-\int_{l_\mathrm{w}}^{l_\mathrm{t}} \mu\left(u_{\mathrm{c},tt} - \ddot{l}_\mathrm{w}\right)\delta u_\mathrm{c}\mathrm{d}s + \int_{l_\mathrm{w}}^{l_\mathrm{t}} \mu\left(u_{\mathrm{c},tt} - \ddot{l}_\mathrm{w}\right)\delta l_\mathrm{w}\mathrm{d}s\right] \tag{A.17}$$

$$\int_{t_1}^{t_2} \delta\mathcal{E}_{m_\mathrm{w}} \mathrm{d}t = \int_{t_1}^{t_2} \mathrm{d}t \left[-m_\mathrm{w} \left(u_{\mathrm{w},tt}(0,t) - \ddot{l}_\mathrm{w} \right) \delta u_\mathrm{w}(0) + m_\mathrm{w} \left(u_{\mathrm{w},tt}(0,t) - \ddot{l}_\mathrm{w} \right) \delta l_\mathrm{w} \right] \quad \text{(A.18)}$$

$$\int_{t_1}^{t_2} \delta\mathcal{E}_\mathrm{s} \mathrm{d}t = \int_{t_1}^{t_2} \mathrm{d}t \left[-m_\mathrm{sh} \left(u_{\mathrm{w},tt}(l_\mathrm{w},t) - \ddot{l}_\mathrm{w} \right) \delta u_\mathrm{w}(l_\mathrm{w}) + m_\mathrm{sh} \left(u_{\mathrm{w},tt}(l_\mathrm{w},t) - \ddot{l}_\mathrm{w} \right) \delta l_\mathrm{w} \right] \quad \text{(A.19)}$$

$$\int_{t_1}^{t_2} \delta\mathcal{E}_{m_\mathrm{c}} \mathrm{d}t = \int_{t_1}^{t_2} \mathrm{d}t \left[-m_\mathrm{c} \left(u_{\mathrm{c},tt}(l_\mathrm{t},t) - \ddot{l}_\mathrm{w} \right) \delta u_\mathrm{c}(l_\mathrm{t}) + m_\mathrm{c} \left(u_{\mathrm{c},tt}(l_\mathrm{t},t) - \ddot{l}_\mathrm{w} \right) \delta l_\mathrm{w} \right] \quad \text{(A.20)}$$

The elastic strain energy of the system, expressed by A.8, can be developed as

$$\delta\hat{\Pi}_\mathrm{w} = EA\, u_{\mathrm{w},s} \frac{\partial}{\partial s}(\delta u_\mathrm{w}) \quad \text{(A.21)}$$

$$\int_{t_1}^{t_2} \delta \left(\int_0^{l_\mathrm{w}} \hat{\Pi}_\mathrm{w}\, ds \right) \mathrm{d}t = \int_{t_1}^{t_2} \mathrm{d}t\, EA \left[u_{\mathrm{w},s}(l_\mathrm{w}) \delta u_\mathrm{w}(l_\mathrm{w}) - u_{\mathrm{w},s}(0) \delta u_\mathrm{w}(0) - \int_0^{l_\mathrm{w}} u_{\mathrm{w},ss}\, \mathrm{d}s\, \delta u_\mathrm{w} \right] \quad \text{(A.22)}$$

$$\int_{t_1}^{t_2} \delta \left(\int_{l_\mathrm{w}}^{l_\mathrm{t}} \hat{\Pi}_\mathrm{c}\, \mathrm{d}s \right) \mathrm{d}t = \int_{t_1}^{t_2} \mathrm{d}t\, EA \left[u_{\mathrm{c},s}(l_\mathrm{t}) \delta u_\mathrm{c}(l_\mathrm{t}) - u_{\mathrm{c},s}(l_\mathrm{w}) \delta u_\mathrm{c}(l_\mathrm{w}) - \int_{l_\mathrm{w}}^{l_\mathrm{t}} u_{\mathrm{c},ss}\, \mathrm{d}s\, \delta u_\mathrm{c} \right] \quad \text{(A.23)}$$

With respect to the gravitational component of Eqn. A.1, it results

$$\begin{aligned} &\int_{t_1}^{t_2} \delta\Pi_\mathrm{g} = \\ &= \int_{t_1}^{t_2} \left[\int_0^{l_\mathrm{w}} \mu g\, \delta u_\mathrm{w}\, \mathrm{d}s - \int_{l_\mathrm{w}}^{l_\mathrm{t}} \mu g\, \delta u_\mathrm{c}\, \mathrm{d}s + m_\mathrm{w} g\, \delta u_\mathrm{w}(0) + \right. \\ &\left. - m_\mathrm{c} g\, \delta u_\mathrm{c}(l_\mathrm{t}) + m_\mathrm{c} g\, \delta l_\mathrm{w} - m_\mathrm{w} g\, \delta l_\mathrm{w} - \mu l_\mathrm{w} g\, \delta l_\mathrm{w} + \mu l_\mathrm{c} g\, \delta l_\mathrm{w} \right] \end{aligned} \quad \text{(A.24)}$$

Finally, regarding the virtual work done by the non-conservative forces, given by the expression A.10, it is obtained

$$\int_{t_1}^{t_2} \delta W \, \mathrm{d}t = \int_{t_1}^{t_2} \mathrm{d}t \left[\frac{\tau}{r} \delta u_{\mathrm{w}}(l_{\mathrm{w}}) - \frac{\tau}{r} \delta l_{\mathrm{w}} \right] \tag{A.25}$$

Eqns. A.16, A.17, A.18, A.19 and A.20 are introduced into expression A.12. The resulting A.12 and Eqns. A.22, A.23, A.24 and A.25 are introduced into Eqn. A.1. In the resulting Eqn. A.1, grouping the terms that multiply δu_{w}, δu_{c}, $\delta u_{\mathrm{w}}(0)$, $\delta u_{\mathrm{c}}(l_{\mathrm{t}})$ and $u_{\mathrm{w}}(l)$, the equations 5.14, 5.15, 5.16, 5.17 and 5.18 are obtained respectively. An identity is obtained from those terms that multiply δl_{w}.

A. NON-STATIONARY MODEL EQUATIONS

References

[1] **ISO/DIS 18738. Lifts (elevators) - Measurement of lift ride quality**, 2003.

[2] J. M. Aldaia, I. Aranburu, and J. M. Pagalday. **Single parameter elevator comfort evaluation**. In *Elevcon*, 1996.

[3] J.M. Aldaia, I. Aranburu, and J.M. Pagalday. **Mechatronic approach**. *Elevator World*, **45**(9):88 – 92, 1997.

[4] G. Almandoz, J. Poza, M. A. Rodriguez, and A. Gonzalez. **Analytic Model of a PMSM Considering Spatial Harmonics**. In *International Symposium on Power Electronics, Electrical Drives, Automation and Motion SPEEDAM*, 2008.

[5] A. Arakawa and K. Miyata. **A variable-structure control method for the suppression of elevator-cage vibration**. *28th Annual Conference of the IEEE Industrial Electronics Society*, **3**:1830 – 5, 2002.

[6] G. Benczek. **Using accelerometers to identify mechanical weak points (VE2, AFD and IWK curves)**. *Lift-Report*, 2003.

[7] R. E. Blodgett and A. K. Majumdar. **Analysis of elevator rope vibration in tall buildings**. *Journal of Vibration, Acoustics, Stress, and Reliability in Design*, **105**(1):5 – 10, 1983.

[8] Y. Chen and W.D. Zhu. **Forced Lateral Response of Cable-Car Systems in High-Speed Elevators**. *Elevcon*, 2005.

[9] L Chengxuan, W. Xiaolin, L. Jianguo, and M. Xing. **Main vibration sources and spectrum analysis on elevator**. *Elevator World*, October 2008.

[10] R.M. Chi and H.T. Shu. **Longitudinal vibration of a hoist rope coupled with the vertical vibration of an elevator car**. *Journal of Sound and Vibration*, **148**(1):154 – 159, 1991.

[11] B.H. Emory, W.D. Zhu, and S. Kaczmarczyk. **Modal Testing and Modeling of a Simplified Elevator System**. In *Proceedings of the IMAC-XXVII*, Orlando, Florida, USA, 2009.

REFERENCES

[12] Frank Fahy and John Walker. *Fundamentals of noise and vibration*. Spon Press, Taylor & Francis Group, 1998.

[13] D. Fukui, K. Okamoto, H. Kodera, and T. Niikawa. **Analysis of elevator dynamics with building block model method**. Symposium on the mechanics of Slender Structures (MoSS), 2006.

[14] K. Funai, H. Katayama, J.-I. Higaki, K. Utsunomiya, and S. Nakashima. **The Development of Active Vibration Dampers for Super High-Speed Elevators**. *Lift Report*, (5), Sept. 2004.

[15] R.-F. Fung, J.-H. Lin, and C.-M. Yao. **Vibration analysis and suppression control of an elevator string actuated by a PM synchronous servo motor**. *Journal of Sound and Vibration*, **206**(3):399 – 423, 1997.

[16] X.Y. Gang, D.Q. Mei, and Chen Z.C. **A horizontal vibration lift model for high speed elevators**. *Key Engineering Materials*, **297-300**:1585–1591, 2005.

[17] Jacek F. Gieras, Chong Wang, and Joseph C. Lai. *Noise of polyphase Electric Motors*. Taylor & Francis Group, LLC, 2006.

[18] T Hagiwara, T. Hamada, and S. Yamamoto. **Automatic guide-rail measuring system for elevator installation and renewal**. In *Elevcon*, 2004.

[19] I. Herrera. **Mechanical Modelling and Simulation Lift Systems: the Influence of the Dynamic Behaviour of Slender Structural Components**. In *Symposium on the Mechanics of Slender Structures (MoSS 2010), San Sebastian, Euskadi, Spain*, 2010.

[20] M Hirose, A. Oomiya, and K. Miyoshi. **New speed control techniques for high speed elevators**. In *Elevcon*, 1993.

[21] Roger E. Howkins. **Elevator Ride Quality. The Human Ride Experience**. *Lift Report*, **Issue 1/2007**, 2007.

[22] I. Isasa. *Model validation applied to locally nonlinear lift structures*. PhD thesis, Mondragon Unibertsitatea, 2009.

[23] S. Kaczmarczyk. **The passage through resonance in a catenary-vertical cable hoisting system with slowly varying length**. *Journal of Sound and Vibration*, **208**(2):243 – 265, 1997.

[24] S. Kaczmarczyk. **The Prediction and Analysis of Lift Car- Hoist Rope Vibration Interactions**. In *Elevcon*, 2005.

[25] S. Kaczmarczyk. **Prediction on the influence of vibration on structural integrity of elevator suspension ropes**. *Key Engineering Materials*, **293-294**:761–768, 2005.

[26] S. Kaczmarczyk. **The dynamic response of elevator compensating ropes in high-rise buildings**. *Lift-Report*, 2009.

[27] S. Kaczmarczyk, J.P. Andrew, and J.P. Adams. **The modelling and prediction of the influence of building vibration on the dynamic response of elevator ropes**. *Materials Science Forum*, **440-441**:489 – 496, 2003.

[28] S. Kaczmarczyk and P. Andrew. **Vibration analysis of elevator ropes**. *Elevator World*, **53**(6):126 – 129, 2005.

[29] S. Kaczmarczyk and R. Iwankiewicz. **Dynamic response of an elevator car due to stochastic rail excitation**. *Proc. Estonian Acad. Sci. Phys. Math.*, **55**:58–67, 2006.

[30] S. Kaczmarczyk and W. Ostachowicz. **Non stationary responses of cables with slowly varying length**. *International Journal of Acoustics and Vibration*, (5):117–126, 2000.

[31] S. Kaczmarczyk and W. Ostachowicz. **Transient vibration phenomena in deep mine hoisting cables. Part 1: Mathematical model**. *Journal of Sound and Vibration*, **262**(2):219 – 244, 2003.

[32] H. Kimura, H. Ito, Y. Fujita, and T. Nakagawa. **Forced vibration analysis of an elevator rope with both ends moving**. *Journal of Vibration and Acoustics*, **129(4)**:471–477, Feb 21 2007.

[33] T. Kotera. **Vibrations of a string with time-varying length**. *Bulletin of the JSME*, **21**(160):1469 – 1474, 1978.

[34] H. Liu, Z. Q. Zhu, E. Mohamed, Y. Fu, and X. Qi. **Flux-Weakening Control of Nonsalient Pole PMSM Having Large Winding Inductance, Accounting for Resistive Voltage Drop and Inverter Nonlinearities**. *IEEE Transactions on Power Electronics*, **27**(2), Feb. 2012.

[35] G. P. Lorsbach. **Measurement of lift ride quality**. *Lift-Report*, 2000.

[36] G. P. Lorsbach. **Analysis of elevator ride quality, vibration**. *Elevator World*, **51**(6):108 – 110, 2003.

[37] D. Mei, X. Du, and Z. Chen. **Optimization of dynamic parameters for a traction-type passanger elevator using a dynamic byte coding genetic algorithm**. *Journal of Mechanical Engineering Science*, **223 Part C**, 2009.

[38] L. Meirovitch. *Fundamentals of vibrations*. Mc Graw Hill, 2001.

[39] N. Mutoh, K. Kagomiya, T. Kurosawa, M. Konya, and T. Andoh. **Horizontal vibration suppression method suitable for super-high-speed elevators**. *Electrical Engineering in Japan*, **129**(1):59 – 73, 1999.

[40] K. Nai, W. Forsythe, and R. M. Goodall. **Modelling and simulation of a lift system**. In *IMA International Conference on Control*, pages 6–11, 1992.

[41] K. Nai, W. Forsythe, and R.M. Goodall. **Improving ride quality in high-speed elevators**. *Elevator World*, **45**(6):88 – 93, 1997.

[42] S. Nakagiri. **Eigenvalue analysis of a long cable modeled as assembled links**. *Theoretical and Applied Mechanics*, **50**:159 – 163, 2001.

[43] S. Nakagiri and S. Takahashi. **Effect of horizontal constraints on flexural vibration of a long elevator rope**. *Theoretical and Applied Mechanics Japan*, **52**:145 – 151, 2003.

[44] M. Otsuki, R. Nakada, K. Yoshida, K. Nagata, S. Fujimoto, and T. Munakata. **Vibration control of rope-sway of elevator for high-rise building**. *Proceedings of the ASME Design Engineering Technical Conference*, **6 B**:1861 – 1868, 2001.

[45] M. Otsuki, K. Yoshida, K. Nagata, S. Fujimoto, and T. Nakagawa. **Experimental study on vibration control for rope-sway of elevator of high-rise building**. *Proceedings of the 2002 American Control Conference*, **1**:238 – 43, 2002.

[46] M. Otsuki, K. Yoshida, S. Nakagaki, T. Nakagawa, S. Fujimoto, and H. Kimura. **Experimental examination of non-stationary robust vibration control for an elevator rope**. *Proceedings of the Institution of Mechanical Engineers. Part I: Journal of Systems and Control Engineering*, **218**(7):531 – 544, 2004.

[47] J.M. Pagalday, X. Sagartzazu, A. Mardaras, M. Calzada, and M.A. Madoz. **Implementation of a theoretical-experimental model for improving the comfort in lift installations**. *Proceedings of the 2004 International Conference on Noise and Vibration Engineering, ISMA*, pages 3611 – 3624, 2004.

[48] R. H. Park. **Two Reaction Theory of Synchronous Machines**. *AIEE Transactions*, **48**:716–730, 1929.

[49] Z. J. Piech. **Coated steel belts and elevator machinery**. *Elevatori*, 2005.

[50] J. G. Proakis and D. G. Manolakis. *Digital signal processing*. Prentice Hall, 1996.

[51] H. Ren and W. D. Zhu. **An accurate spatial discretization and substructural method with application to moving elevator cable-car systems. Part I: methodology**. In *Proceedings of the ASME 2011 International Design Engineering Technical Conferences & Computers and Information in Engineering Conference*, 2011.

[52] H. Ren and W. D. Zhu. **An accurate spatial discretization and substructural method with application to moving elevator cable-car systems. Part II: application**. In *Proceedings of the ASME 2011 International Design Engineering Technical Conferences & Computers and Information in Engineering Conference*, 2011.

[53] R. Roberts. **Control of hig-rise/high-speed elevators**. In *Proceedings of the American Control Conference*, pages 3440– 3444, 1998.

[54] R. Salamaliki-Simpson, S. Kaczmarczyk, P. Picton, and S. Turner. **The dynamics and vibration of an elevator car-suspension rope system**. In *Twelfth International Congress on Sound and Vibration*, 2005.

[55] R. Salamaliki-Simpson, S. Kaczmarczyk, P. Picton, and S. Turner. **The vibration study of non-linear interactions in a moving elevator car-suspension rope system**. In *Proceedings of the Symposium on the Mechanics of Slender Structure (MoSS)*, Northampton (UK), 28 - 29 September 2006.

[56] M. Sissala, T. Heimola, and M. Otala. **Optimization of a lift car vibrational behaviour by modal analysis**. *Elevator World*, **33**(6):39 – 43, 1985.

[57] Y. Takeichi, S. Komada, M. Ishida, and T. Hori. **Speed control of symmetrical type three-mass resonant system by PID-controller**. *4th International Workshop on Advanced Motion Control Proceedings*, **2**:594 – 9, 1996.

[58] Y. Terumichi, S. Kaczmarczyk, S. Turner, M. Yoshizawa, and W. Ostachowicz. **Modelling, simulation and analysis techniques in the prediction of non-stationary vibration response of hoist ropes in lift systems**. *Materials Science Forum*, **440-441**:497 – 504, 2003.

[59] Y. Terumichi, M. Ohtsuka, M. Yoshizawa, Y. Fukawa, and Y. Tsujioka. **Non-stationary vibrations of a string with time-varying length and a mass-spring system attached at the lower end**. *Nonlinear Dynamics*, **12**(1):39 – 55, 1997.

[60] P. Vas. *Sensorless Control and Direct torque Control*. Oxford Science publications, 1998.

[61] S.R. Venkatesh, Y. M. Cho, and J. Kim. **Robust control of vertical motions in ultra-high rise elevators**. *Control Engineering Practice*, **10**:121–132, 2002.

[62] S.R. Venkatesh and Y.M. Cho. **Identification and control of high-rise elevators**. In *Proceedings of the American Control Conference*, 1998.

[63] Jovan Vladic, Radomir Dokic, Milan Kljajin, and Mirko Karakasic. **Modelling and simulations of elevator dynamic behaviour**. *Modeliranje i simulacije dinamickog ponasanja dizala*, **18**:423–434, 2011.

[64] J.A. Wickert and C.D. Jr. Mote. **Classical vibration analysis of axially moving continua**. *Journal of Applied Mechanics, Transactions ASME*, **57**(3):738 – 744, 1990.

[65] T. Yamamoto, K. Yasuda, and M. Kato. **Vibration of a string with time-varying length**. *Bulletin of the JSME*, **21**(162):1677 – 1684, 1978.

[66] Y. Yamazaki, M. Tomisawa, K. Okada, and Y. Sugiyama. **Vibration control of super-high-speed elevators. (Car vibration control method based on computer simulation and experiment using a full-size car model)**. *JSME International Journal, Series C (Dynamics, Control, Robotics, Design and Manufacturing)*, **40**(1):74 – 81, 1997.

[67] C.Y. Zhang, G. Yang, and C. Zhu. **Parametric resonance of elevator rope and the suppression strategy**. *Elevator world*, 2007.

[68] C.Y. Zhang, C.M. Zhu, Z.Q. Lin, and T.X. Wu. **Theoretical and experimental study on the parametrically excited vibration of mass-loaded string**. *Nonlinear Dynamics*, **37**:1–18, 2004.

[69] Y. Zhang, S.K. Agrawal, and P. Hagedorn. **Longitudinal vibration modeling and control of a flexible transporter system with arbitrarily varying cable lengths**. *Journal of Vibration and Control*, **11**(3):431 – 456, 2005.

[70] Y.Q. Zhou. **Models for an elevator hoistway vertical dynamic system**. In *5th International Congress on Sound and Vibration*, 1997.

[71] W. D. Zhu and Y. Chen. **Forced response of translating media with variable length and tension: application to high speed elevators**. ASME International Mechanical Engineering Congress and exposition, 2004.

[72] W. D. Zhu and Y. Chen. **Theoretical and Experimental Investigation of Elevator Cable Dynamics and Control**. *Journal of Vibration and Acoustic*, **128 (1)**:66–78, 2006.

[73] W. D. Zhu, J. Ni, and J. Huang. **Active control of translating media with arbitrarily varying length.** *American Society of Mechanical engineers. Journal of Vibration and Acoustics*, **123**:347–358, 2001.

[74] W. D. Zhu, H. Ren, and C. Xiao. **A Nonlinear Model of a Slack Cable With Bending Stiffness and Moving Ends With Application to Elevator Traveling and Compensation Cables**. *Journal of Applied Mechanics*, **78**(4), 2011.

[75] W.D. Zhu and J. Ni. **Energetics and stability of translating media with an arbitrarily varying length**. *Transactions of the ASME. Journal of Vibration and Acoustics*, **122**:295 – 304, 2000.

[76] W.D. Zhu and L.J. Teppo. **Design and analysis of a scaled model of a high-rise, high-speed elevator**. *Journal of Sound and Vibration*, **264**:707 – 31, 2003.

[77] W.D. Zhu and G.Y. Xu. **Vibration of elevator cables with small bending stiffness**. *Journal of Sound and Vibration*, **263**(3):679 – 99, 2003.